ULTRAFAST OPTICAL PULSES: SYNTHESIS AND APPLICATIONS

A Dissertation

by

KAI WANG

Submitted to the Office of Graduate and Professional Studies of
Texas A&M University
in partial fulfillment of the requirements for the degree of

DOCTOR OF PHILOSOPHY

Chair of Committee,	Alexei V. Sokolov
Committee Members,	Olga Kocharovskaya
	M. Suhail Zubairy
	Hong Liang
Head of Department,	George R. Welch

December 2013

Major Subject: Physics

ABSTRACT

This dissertation is devoted to ultrafast waveform synthesis using coherent Raman sidebands with the assistance of pulse shapers based on acousto-optic programmable dispersive filter (AOPDF) or deformable mirror (DM). Ultrashort optical science has encompassed the realm of electronic and chemical processes taking place on the few femtosecond-to-attosecond timescale. Molecular modulation is a technique that has been developed to produce ultrafast pulses based on broadband coherent Raman scattering, which provides the required optical bandwidth. This technique is capable of producing a pulse whose duration can be shorter than one optical field cycle in the visible-UV range, providing a potential for non-sinusoidal field synthesis.

We produce the coherent Raman sidebands in a Raman-active crystal driven by two-color femtosecond laser pulses. With the assistance of a pulse shaper based on AOPDF, we report the phase control of the ultrabroad spectrum, aiming to synthesize non-sinusoidal waveforms. The setup allows for both coarse, manual phase adjustments and programmable fine-tuning of spectral phases. A flat spectral phase across these 5 frequency-separated sub-bands is achieved, which implies generation of isolated 2 to 3 optical-cycle pulses.

The energy of the ultrafast waveform produced in this setup is limited by the damage threshold of the pulse shaper. In order to obtain high energy ultrafast waveforms, we design a reflection scheme using spherical mirrors to combine the Raman sidebands. The sidebands and the driving pulses are refocused back to the Raman crystal and the relative spectral phases are retrieved from an interferogram based on nonlinear Raman interaction. Furthermore, using a DM to adjust the spectral phases, we demonstrate that our setup is capable of synthesizing ultrafast

waveforms using the coherent Raman sidebands.

We explore an additional ultrashort pulse generation technique, theoretically. We investigate formation of resonant dispersive waves (RDW) in photonic crystal fibers (PCF). Our simulation shows that with an input of two pulses, or a broadband chirped pulse in a PCF, RDW could form a sufficiently short pulse in the UV region, which could be a new method to obtain the ultrashort UV pulse.

In addition to studying methods for production of ultrashort pulses, we explore areas where such pulses can be utilized. The field of ultrafast optics is highly interdisciplinary, with a wide range of applications. We report two experiments with femtosecond laser pulses: 1) We demonstrate a scheme which achieves sub-diffraction imaging of remote objects by using femtosecond laser filaments. The use of laser filaments for imaging is destined to have applications in many environments. Achieving super-resolution has become a scientific imperative for remote imaging of objects and scenes needing increased detail and has motivated the development of various laser-based techniques. 2) All-optical control device where the "gate" photon could switch a "source" light beam has been a long-standing goal in optics, especially in optical communication. In a transversely excited atmospheric (TEA) nitrogen laser setup, we trigger the nitrogen laser radiation with a femtosecond laser pulse switching a transverse discharge in air. Moreover, with two TEA lasers as a model, we demonstrate the swept gain scheme for remote sensing.

DEDICATION

To My Parents, Xiangyu Wang and Xiaoxia Ding

ACKNOWLEDGEMENTS

First and foremost, I give my special thanks to my Ph. D advisor Dr. Alexei V. Sokolov for his guidance and continuous support through the years as my friend and mentor. His wealth of knowledge and enthusiasm for research are keys to my research. He introduces me to the world of laser physics and trains me to be an experimentalist in physics with great patience. I also would like to thank the support from Dr. M. Scully during my study, who is the leader of institute for quantum science and engineering. His hard work and ingenious thinking always inspire me. I want to particularly thank Dr. Miaochan Zhi, who was the leader of our experiments in the past years. Most of this work presented in this dissertation is done with her and Xia Hua, the other colleague who I give special thanks to. Without Miaochan's leadership and collaborations, our experiments would not be accomplished.

I appreciate my committee, Dr. Olga Kocharovskaya, Dr. Hong Liang, and Dr. M. Suhail Zubairy, for their helpful discussions and their time invested in the processes. I would like to thank Dr. Hemmer for sharing his idea about laser filamentation with us and inspire us to accomplish the experiment. I also thank my Texas A&M University colleagues who spend time to read my dissertation and help me improve the language. They are Dr. Amitabh Joshi, Dr. Dmitri Voronine, Dr. Alex Sinyukov, Dr. Benjiamin Strycker, Jonathan Thompson, and Charles Ballman. I am grateful for the former colleagues in our group, Dr. Andrea Burzo, Dr. Jiahui Peng, who I worked with through years. They taught me the experimental skills and tricks, and helped me to become an experimental researcher.

My special thanks are extended to Dr. Qingqing Sun and Dr. Xi Wang for the help during the early years in College Station. I would like to thank for the Institute

of Quantum Sciences and Engineerings (IQSE) colleagues, Dr. George R. Welch, Dr. James Strohaber, Dr. Anatoly V Svidzinsky, Dr. Ariunbold Gombojav, Dr. Hebin Li, Dr. Pankj. K. Jha, Dr. Matthew M. Springer, Dr. Dawei Wang, Dr. Ziyun Di, Dr. Feng Zhu, Kim Chapin, Han Cai, Yujie Shen, Andrew Travero, Luqi Yuan, Zhenhuan Yi, and many other fellow graduate students and friends for their help in life and research. I would like to thank the people outside A&M, Dr. R.E. Meyers, Dr. V.A. Polovinkin, and Dr. Y.V. Radeonychev for their collaborations. I appreciate that Dr. J. Dudley and Dr. F. Biancalana from University of Bath to share their program for the simulation.

I also would like to offer my special thanks to master thesis advisor Dr. Ying Gu from Peking University in China. She helped me to establish a good background in quantum optics and trained me to overcome my weakness.

I am very thankful for my parents to support and encourage me all the time.

NOMENCLATURE

AOPDF	acousto-optic programmable dispersive filter
AS	anti-Stokes
BBO	barium borate
CARS	coherent anti-Stokes Raman scattering
CFWM	cascaded four wave mixing
CRS	coherent Raman scattering
CSRS	coherent Stokes Raman scattering
DM	deformable mirror
FROG	frequency-resolved optical gating
FTL	fourier transform limited
FWHM	full width half maximum
FWM	four wave mixing
FWRM	four-wave mixing Raman
fs	femtosecond
HC	hollow core
HHG	high harmonic generation
LCM	liquid crystal modulators
MEMS	micro-electro-mechanical systems
NPR	nonlinear polarization rotation
NSE	nonlinear Schrodinger equation
OAM	orbital angular momentum
OPA	optical parametric amplifier
$PbWO_4$	lead tungstate
PCF	photonic crystal fiber

PCF	photonic crystal fiber
PMT	photomultiplier tube
ps	picosecond
RDW	resonant dispersive waves
SFG	sum frequency generation
SHG	second harmonic generation
SPIDER	spectral phase interferometry for direct electrical field reconstruction
SVEA	slowly varying envelope approximation
TC	topology charge
TEA	transversely excited atmospheric
XFROG	cross frequency-resolved optical gating
TxDOT	Texas Department of Transportation

TABLE OF CONTENTS

LIST OF FIGURES

FIGURE Page

1. INTRODUCTION

In the scientific literature, the term "ultrashort" refers to the femtosecond (fs) to picosecond (ps) time scale. An ultrashort optical pulse can provide high time resolution, high spatial resolution, high bandwidth and high intensity [1]. The studies of ultrafast optics are highly interdisciplinary areas, which include the generation of ultrashort optical pulse [2, 3], ultrafast spectroscopy [4, 5], laser controlled chemistry [6], frequency metrology [7], high speed electrical testing [3], laser-plasma interaction [8, 9], biomedical applications [10, 11], and so on.

There are many sources that produce ultrafast optical pulses. Dye lasers, which are easily tuned in wavelength, were the "work horse" throughout the 1980's in laser spectroscopy practiced in physics and chemistry [12]. Solid state lasers, such as Ti:sapphire laser, are very versatile in the field of ultrafast optics due to their high power level [13]. However, due to the bulk optics, they are not optimal for industrial applications. Optical fiber lasers, on the other hand, are compact and easy to integrate making them an ideal choice for industry [14]. Finding a new source of ultrafast optical pulses is still an active research area. Nowadays, high harmonic generation (HHG) is capable of producing the pulse as short as 80 attoseconds in the ultra-violet (UV) region [15]. However, because of the low efficiency of the HHG, the pulse energy generated using this technique is low, which limits the application in scientific studies. Moreover, in order to study electronic and chemical process under femtosecond time scale, optical pulses of a few femtoseconds or sub-femtosecond are needed. However, there are currently not many sources available for this purpose.

Meanwhile, another technique, called molecular modulation has been under development since the 1990s' [16]. This technique is potentially a complementary method

for HHG and will benefit the field of attoscience. Molecular modulation is based on coherent Raman scattering. Raman scattering is an inelastic scattering process where the scattered photon is different in energy from the incident photon by an amount equal to the molecular vibrational transition [17]. When the energy levels are driven coherently, the Raman process can cascade and generate a broadband spectrum with its components equally separated by the molecular transition. The coherently driven energy level states will evolve coherently and the quantum states of all of the molecular will possess the same phase [18]. This results in a time-dependent modulation of the refractive index of the ensemble with a frequency of approximately hundreds of THz [19]. A medium with a high Raman cross section can greatly affect the amplitude and phase of the spectrum [20]. The resultant strongly-modulated spectrum is capable of supporting a subfemtosecond optical pulse [21].

Experiments of molecular modulation have achieved a lot of progress in many directions. Through adiabatic excitation of the D_2 molecular transitions with nanosecond pulses, the synthesis of a pulse train with nearly single-cycle waveforms was demonstrated by Sokolov *et al.* [22]. Yavuz *et al.* observed the generation of 200 rovibrational sidebands by simultaneously exciting a rotational and a vibrational transition [23]. With the adiabatic Raman excitation technique, Shverdin *et al.* successfully synthesized the first single-cycle optical pulse [24]. Utilizing an impulsive excitation technique, Zhavoronkov and Korn have generated pulses with a period of 3.8 fs in a hollow fiber filled with SF_6 [25]. Some other works worth mentioning include: 1) Yavuz's group proposed a Terahertz radiation source using molecular modulation [26]; 2) Hakuta's group accomplished the sideband generation in solid hydrogen (H2) [27, 28]; 3)In order to utilized molecular modulation technique in precision spectroscopy applications, Yavuz *et al.* extended it using continuous-wave (CW) lasers in a gas filled cavity [29].

Besides exciting Raman transitions in a gaseous medium, researchers found that multiple coherent anti-Stokes Raman scattering (CARS) signals with broad spectral widths can be generated in crystals, such as TiO_2 [30], $PbWO_4$ [31], $KGd(WO_4)_2$ [32], etc.. It can be driven by ultrafast femtosecond laser pulses at room temperature. The spectrum of adjacent CARS peaks are usually overlapped with each other so that the entire spectrum, which has a nearly two-octaves bandwidth, is continuous. This gives us some advantages over the case in gas. The spectrum has a potential to generate isolated femtosecond optical pulses with high energy. Meanwhile, this spectrum can be characterized using ultrashort pulse characterization techniques. Besides driving the coherent Raman scattering using two-color femtosecond laser pulses, Zhi *et al.* demonstrated cascaded generation of sidebands using chirped femtosecond laser pulses in solids [33]. In addition, coherent Raman scattering in solids can also be used to generate high order femtosecond optical vortices[34]. In principle, this is capable to produce subcycle optical vortices combined with pulse synthesis techniques[35]. Worthy of mention, there is another similar technique based on cascaded four wave mixing (CFWM) processes in a solid medium, which showed the potential for the generation of ultrafast optical pulses, especially in the UV range [36]. CFWM has been extensively studied in the last two decades in parallel with the molecular modulation technique [36, 37]. Notably, a sub-10-fs deep-ultraviolet pulse has been generated using CFWM in gaseous media [38].

The Raman sidebands generated in a gaseous media propagate co-linearly. By adjusting the spectral phase of the sidebands, it is possible to synthesize an ultrashort waveform using the coherent Raman sidebands [39]. Recently, researchers demonstrated that ultrafast waveform synthesis can be accomplished with the assistance of a pulse shaper. For example, Pandiri *et al.* showed that by employing a combination of a spatial phase controller and a spectral interferometer, the spectral phase

of Raman sidebands can be finely controlled at the target [40]. Another remarkable result is from Kung's group. Using the Raman sidebands generated from hydrogen gas, they demonstrated an optical function generator [41]. They produced Raman sidebands by beginning with a driving laser frequency that is nearly equal to the molecular Raman resonance. As a result, the frequencies of generated sidebands are commensurate ($\omega_n = n\omega_m$). The carrier envelope phase was stable and can be controlled precisely. This satisfies the aforementioned conditions for arbitrary optical waveform synthesis with any desired shape [42, 43]. Also, since the spectrum covers more than one octave, the synthesis of a subcycle optical pulse is possible. This provides opportunities for shaping not only the pulse envelope but also the shape of the electric field itself [44]. In Kung's work, they demonstrated the synthesis of waveform trains of square shape (sawtooth, triangle, etc.) for electric fields.

For a cascaded Raman process in solid medium, due to the pulse dispersion of the solid state, the pump beam and the Stokes beam need to be incident on the crystal with a phase matching angle. The sidebands of coherent Raman scattering are also generated with different angles as a result of phase matching. This makes it a challenge to combine these sidebands into a single beam. One needs to correct both the angle dispersion and temporal dispersion. Matsubara et al proposed and demonstrated that the angular dispersion can be compensated using a grating [45] and a prism [46].

Characterization of the generated ultrafast wave is as important as the waveform synthesis itself. Many techniques have been developed for the ultrafast pulse characterization [47]. People have already applied these technique to characterize ultrafast waveforms synthesized using Raman sidebands. Both Matsubara et al [45] and Pandiri *et al.* [40] have used the spectral phase interferometry for direct electrical field reconstruction (SPIDER) technique for pulse characterization in their work.

Kung's group, in their optical function generator experiment, used the linear cross-correlation technique to measure their optical waveform [41]. In addition to these methods, the relative spectral phase could be characterized by the sum frequency generation among different frequencies, which was pointed out by Hansh 20 years ago [48]. Hsieh *et al.* used this technique to show the interpulse phase locking of an optical frequency comb based on Raman [49].

In our own research, we proposed some schemes utilizing the pulse shapers to assist the synthesis of ultrafast waveforms using coherent Raman sidebands produced from Raman active crystals. The first scheme is utilization of a pulse shaper based on an acousto-opitc programmable dispersive filter (AOPDF), also known as Dazzler. This device is capable of correcting the dispersion up to the fourth order. Differing from pulse shapers based on liquid crystal modulators (LCM), Dazzler does not require the dispersive device to separate the frequency component. Moreover, Dazzler works when different frequency components are collinearly incident. Our experiment is similar to the work of Matsubara et. al. [46] where we use a prism to combine the Raman sidebands generated in crystal into a collinear beam. Because the linear dispersion is too great to be corrected by the Dazzler, we first manually pre-compensate linear chirp by inserting glass slides into the beam paths. Dazzler is used to correct the higher order dispersion, and adjust the relative spectral phase and amplitude for the waveform synthesis. The ultrashort waveform is characterized using the method proposed by Hansh [48], which is to generate the inteferogram using the second harmonic by scanning the phase of parts of the spectrum. Through theoretical simulation of the spectrogram, we can retrieve the relative spectral phases and amplitude of the sidebands, which is sufficient to retrieve the ultrafast waveform.

The second scheme we proposed is to use a reflection scheme to characterize and synthesize the ultrafast waveform. Spherical mirrors are used to reflect and refocus

the generated beams back to the crystal. When they overlap again on the crystal, the multi sidebands interact with each other. By scanning the phase of the sidebands, we get an interferogram, which is essentially a cross-FROG (XFROG) trace. A theoretical simulation is used to retrieve the spectral phase from the spectrogram. In order to synthesize the ultrafast waveform, we will use a micro-electro-mechanical systems (MEMS) deformable mirror (DM) (BOSTON Micromachines. Co.). The DM is inserted into the optical path to adjust the spectral phases of the sidebands. This phase sensitive device is demonstrated to be capable of assisting the synthesis of the ultrafast waveform using coherent Raman sidebands.

This dissertation is mainly devoted to ultrafast waveform synthesis using coherent Raman sidebands. The rest of the dissertation is organized as follows. In Section II, concepts of the nonlinearity of ultrafast pulses and the theory of the coherent Raman generation are introduced. In Section III, the experiments of the generation of coherent Raman scattering in solids (diamond and $PbWO_4$) are described. We show how to enhance the coherent Raman scattering in a double-path reflection scheme. As a result of the enhancement, the spectrum of coherent Raman scattering is broadened with the generation of five new AS sidebands. Using the same setup, the CFWM generated in a piece of glass is extended to UV in the experiment. In Section IV, the synthesis and measurement of ultrafast waveform with the assistance of pulse shapers based on AOPDF or DM using coherent Raman sidebands are presented. With the pulse shaper based on AOPDF, we retrieve the ultrafast waveform based on second harmonic generation (SHG) and sum frequency generation (SFG) from a BBO crystal. Using five Raman sidebands generated from diamond, we produce a pulse as short as two optical cycle. However, the energy of the pulse is mainly limited by the damage threshold of the pulse shaper. Therefore, we employ spherical mirrors to assist the ultrafast waveform synthesis in a reflection scheme. We retrieve spectral

phases from an interferogram based on nonlinear Raman interaction. Furthermore, a DM is used to assist the phase control of Raman sidebands. The experiment demonstrates that our setup is capable of synthesizing the ultrafast waveform using coherent Raman sidebands.

In the Section V, some studies of the ultrafast laser's application are given. Ultrafast laser pulses with their unique properties could be utilized in many interdisciplinary fields. This section is divided into three subsections as follows.

The first subsection is about sub-diffraction imaging using femtosecond laser filamentation in remote sensing. The femtosecond laser filamentation occurs when an intense femtosecond laser pulse self-focuses to a sufficient intensity capable of ionizing the propagation medium. Once this threshold is reached, the laser beam is self-guided and its size is determined by the interplay between Kerr self-focusing and defocusing from low density plasma [50]. The diameter of the filaments (around one hundred micrometers in air) is not be affected by the aperture of optical systems. Therefore, we propose that the laser filament can be used to increase the resolution of an imaging system whose resolution limit is bigger than the diameter of laser filamentation. For example, since laser filamentation can be formed of a long distance from the source [51–53], the resolution of the detecting device in remote sensing could be improved by several orders in an atmospheric environment [54]. We demonstrate sub-diffraction imaging using laser filamentation in the lab. The filament was formed in a glass tank. Since the density of water is thousands of times bigger than that of atmosphere, this setup is used to scale the propagation of the laser in air for several kilometers [55]. With laser filamentation, we can improve the resolution by two orders of magnitudes in this remote sensing scenario.

The second subsection is about optical switching of a transversely excited atmospheric (TEA) nitrogen laser. The TEA nitrogen laser is a gas laser that can work

in the atmospheric pressure [56]. The TEA nitrogen laser pulse is about 1 nanosecond and the wavelength is 337 nm. Our TEA laser is home-made, and the lasing medium is the molecular nitrogen in air. In general, the TEA laser is triggered by an air breakdown process between two electrodes. We use femtosecond laser pulses to produce a conventional plasma to trigger the air breakdown process inside the spark gap. Our experiments demonstrate that the TEA laser can be synchronized with the femtosecond laser pulse. However, the microsecond jitter between the air breakdown and the nitrogen laser pulse limits the applications of our scheme. In addition, using the TEA nitrogen laser to set up a model, we demonstrate a swept gain scheme in remote sensing [57].

The last subsection is a theoretical simulation of generating UV femtosecond pulses in photonic crystal fibers (PCF). The high order dispersion in PCF could lead to the generation of the resonant dispersive waves (RDW) in normalous dispersion region [58, 59]. In photonic crystal fiber such as Kagome-lattice hollow core (HC) photonic crystal fiber, the fourth oder dispersion leads to a RDW produced in UV range, which can be a source for UV femtosecond optical pulses. We use the theoretical simulation to study if the UV RDW could be sufficient shorter in Kagome-lattice HC-PCF by inputting two near infrared optical pulses. The theoretical simulation shows that by inputting two pulses with different wavelength, we could produce a pulse as short as 30 fs in the UV region. Furthermore, with inputting a broadband chirped near-infrared femtosecond pulse, it could produce a UV RDW as short as 50fs. This work is cooperated with J. Dudley and F. Biancalana from University of Bath.

2. BASIC CONCEPTS OF ULTRAFAST NONLINEAR OPTICS

In this section, I will introduce some concepts of the nonlinearity of ultrafast pulses and Raman scattering, which are related to the contents of the following section.

Due to the high intensity of femtosecond laser pulses, there exist versatile nonlinear optical phenomena when the pulse propagates through the medium. Nonlinear optical effect plays an important role in ultrafast optics. As an example, both the generation and characterization of the ultrafast pulse are based on the optical nonlinearity [1]. Moreover, the interplays between nonlinear optical effects could result in some interesting unique phenomena. When the pulses propagate in air or liquid, the Kerr-effect and the plasma defocusing will lead to laser filamentation. In the medium with anormalous dispersion such as photonic crystal fiber, optical solitons occur because of the balanced dispersion and Kerr-effect.

In the first subsection, the basic equations of propagations of the electromagnetic waves in medium are described. Then, two nonlinear optical effects namely laser filamentation and optical soliton, are introduced. The next subsection discusses the basic concepts for Raman scattering, coherent Raman scattering and stimulated Raman scattering. Theory of coherent Raman scattering for the generation of ultrafast optics pulses is reviewed in the last subsection.

2.1 Propagation of Electromagnetic Waves in Medium

Light is electromagnetic wave with certain frequency. The propagation of light is described using Maxwell's equations:

$$\begin{aligned} \nabla \times \mathbf{H} &= \mathbf{j} + \tfrac{\partial \mathbf{D}}{\partial t}, \\ \nabla \cdot \mathbf{B} &= 0, \\ \nabla \times \mathbf{E} &= -\tfrac{\partial \mathbf{B}}{\partial t}, \\ \nabla \cdot \mathbf{D} &= \rho, \end{aligned} \tag{2.1}$$

where $\mathbf{E}$ represents the electrical field, $\mathbf{B}$ represent the magnetic field (magnetic induction), $\mathbf{D}$ is the electric displacement field and $\mathbf{H}$, sometimes is also called magnetic field ($\mathbf{B}$ is then called magnetic induction). $\mathbf{j}$ is the current density and ρ is the charge density. Usually, we describe the electric field using $\mathbf{E}$, for in the non-relativistic situation, the interaction between electric field $\mathbf{E}$ and charge is much stronger than that of the magnetic field $\mathbf{B}$. When light propagates in the vacuum, we have $\mathbf{D} = \varepsilon_0 \mathbf{E}$, $\mathbf{B} = \mu_0 \mathbf{H}$. ε_0 is the electric permittivity of the free space and μ_0 is the magnetic permeability of the free space. In the medium, we have $\mathbf{D} = \varepsilon \mathbf{E}$, and $\mathbf{B} = \mu \mathbf{H}$. Moreover, the electric displacement is given by

$$\mathbf{D} = \varepsilon_0 \mathbf{E} + \mathbf{P} \tag{2.2}$$

Here, $\mathbf{P}$ is the macroscopic density of the permanent and induced electric dipole moments in the material, called the polarization density. Hence the fundamental equation of optics propagation in either linear or nonlinear regime is,

$$\frac{\partial^2 \mathbf{E}}{\partial z^2} - \frac{1}{c_0^2} \frac{\partial^2 \mathbf{E}}{\partial t^2} = \mu_0 \frac{1}{c_0^2} \frac{\partial^2 \mathbf{P}}{\partial t^2} \tag{2.3}$$

where c_0 is the speed of light in free space. The induced polarization contains both linear and nonlinear optical effects. At low intensity, the induced polarization $\mathbf{P}$ is proportional to the electric field and it is present as:

$$\mathbf{P} = \varepsilon_0[\chi^1\mathbf{E} + \chi^2\mathbf{E}^2 + \chi^3\mathbf{E}^3 + \ldots + \chi^n\mathbf{E}^n + \ldots]. \tag{2.4}$$

Here χ^1 is the linear susceptibility, χ^2 and χ^3 are the second- and third- order susceptibilities. χ^n is the nth-order susceptibility. Written in the form of Eq.(2.4), it is usually assumed that the polarization at time t depends on the instantaneous value of the electric field strength and the medium is lossless. In the general procedure, the nonlinear optical phenomena are described based on the expressing $\mathbf{P}$ in terms of the applied electric field strength $\mathbf{E}$. In theory, $\mathbf{P}$ plays a key role in the description of nonlinear optical phenomena, because the polarization $\mathbf{P}$ can act as the source of the new component of electromagnetic fields.

The macroscopic polarization can be obtained by adding up the electric dipoles of particles per unit volume, *i.e.*

$$\mathbf{P}(t) = N < \mathbf{p} >= N < \mu(t) >, \tag{2.5}$$

where N is the number of the electrical dipoles and μ is the electric dipole moment, $\mu(t) = -e \cdot r(t)$. $r(t)$ is the displacement and it depends on how strong the electron is bound to the nuclei. The nonlinear susceptibility could be described using the quantum mechanical theory [60]. The theoretical calculations of the susceptibility are particular reliable for atomic vapors, because the atomic parameters are known with very high precision.

Eq. (2.3) with higher order differentials can be solved using numerical simulation.

People usually make some reasonable approximation to simplify this propagation equation. **E** is given by:

$$\mathbf{E(r,t)} = \{\frac{1}{2}A(r,t)exp(i(\mathbf{k}r - \omega t))\widehat{e} + c.c\} \tag{2.6}$$

where A is the amplitude and ω is the frequency, $\widehat{e}$ is the unit polarization vector. Therefore, the polarization **P** can be written as $\mathbf{P} = \frac{1}{2}Pexp(i(\mathbf{k}\cdot\mathbf{r} - \omega t)) + c.c.$ In a slowly varying envelope approximation (SVEA), in which the envelope of a forward-travelling wave pulse varies slowly in time and space compared to a period or wavelength, i.e. $|\frac{\partial^2 E}{\partial z^2}| \ll |2i\omega_0\frac{\partial E}{\partial t}| \ll |\omega_0^2 E|$, assuming that beam propagates along z direction, the propagation equation becomes

$$\frac{\partial A}{\partial z} + (\frac{\partial^2 A}{\partial x^2} + \frac{\partial^2 A}{\partial y^2}) + \frac{1}{c}\frac{\partial A}{\partial t} = -i\frac{\mu_0\omega_0^2 P}{2k_0}. \tag{2.7}$$

Using this equation, we can study many interesting nonlinear light-matter interaction phenomena [50, 60, 61]. In the following subsection, femtosecond laser filamentation and optical soliton are introduced.

2.2 Femtosecond Laser Filamentation

Laser filamentation was firstly observed as the filamentary damage tracks in glassin 1964 [62]. Filament propagation of laser pulses in the atmosphere was observed in 1994 by Gerard Mourou, *et al.* [63]. The filamentation in atmosphere is created because the balance between the self-focusing refraction and self-attneuating diffraction by ionization and rarefaction of a laser beam of terawatt intensities. The "filament" acts like a wave guided thus preventing the divergence. There have been sophististicated models developed to describe the filamentation process [50].

We give an example using the propagation equations to study the femtosecond

laser filamentation propagation in medium. We consider that the laser field is linearly polarized. In the atmosphere, the filamentation will happens when the intensity is higher than $5 \times 10^{13} W/cm^2$. In this case, the third-order nonlinearity such as the optical Kerr effect, is the important phenomenon in the centro-symmetric medium for the light propagation. The Kerr effect leads to a self-focusing of the beam. On the other hand, the high intensity of the beam ionizes the medium and produces the plasma in the path of the beam. The plasma defocus the self-focusing beam because of the refractive index gradient from the uneven plasma density. Therefore, the balance between the self-focusing and defocusing forms a "self-guided" beam along the propagation.

The optical Kerr effect could be described with the nonlinear polarization $P_{nl} = \varepsilon_0 \chi^3 |\mathbf{E}|^2 \mathbf{E}$, where $\chi^3 = \epsilon_0 c n_2 n_0^2/3$ (n_2 is the coefficient of the nonlinear Kerr index). Using the reference frame of the pulse ($z, t = t_{lab} - z/v_g(\omega - 0)$), where $v - g(\omega_0) = \frac{\partial \omega}{k}|_{\omega_0}$ denote the group velocity, we obtain the nonlinear Schordinger equation (NSE),

$$\frac{\partial E}{\partial z} = \frac{i}{2k}\Delta_\perp E + i k_0 n_2 |E^2| E - i \frac{k_0}{2n_0}\frac{\rho}{\rho_c} E. \tag{2.8}$$

Here, we assume the constant linear refraction index n_0 constant. The last term accounts for the defocusing of the plasma. The plasma current is introduced by

$$\frac{\partial J_P}{\partial t} = -\frac{e^2}{m_e}\rho E, \tag{2.9}$$

where ρ is the electron density and $\rho_c = \epsilon_0 m_e \omega_0^2/e^2$ is the critical plasma density above which the plasma becomes opaque ($\rho_c = 2 \times 10^{21} cm^{-3}$ at 800 nm). Hence, this model takes into account the main physical effects proposed to be responsible for the self-channeling of ultrashort laser pulse in air by Braun *et al.* [63].This model

was proposed before the discovery of the femtosecond filamentation. For instance, it was used to study the laser induced breakdown in water [64]. The model was used in the early numerical works on femtosecond filamentation Considering the multiphoton ionizaiton process accounts for the generation of the plasma [63, 65, 66]. Researchers have modified the model by including more conditions and other nonlinear phenomena [50], such as group velocity dispersion, Raman effect, tunneling ionization, cross phase modulation, third harmonic generation, and so on. These equations are difficult to solve analytically but they have been studied extensively using numerical simulation.

2.3 Optical Soliton

For Eq. (2.8), if we do not consider the plasma term regarding the plasma, We obtain the general nonlinear Schordinger equation

$$\frac{\partial E}{\partial z} = -\frac{iK_2}{2}\frac{\partial^2 E}{\partial t^2} + i\gamma|E^2|E, \tag{2.10}$$

where K_2 describes the dispersion and γ denotes the Kerr effect. Inside the anormalous dispersive medium, when the wavelength of the light is close to the resonance, $K_2 < 0$. In this case, when $\gamma > 0$, the equation could be solved with inverse scattering transform method [67]. There is an analytical solution for Eq. (5.1), it is

$$E(z,t) = E_0 sech(t/\tau_0)e^{i\kappa z}. \tag{2.11}$$

The wave described by Eq. (2.11) is called the optical soliton. Optical soliton maintains its shape during the propagation. τ_0 is a parameter that characterizes the pulse width of the soliton. The energy per soliton is related to the dispersion of the medium and the third-order nonlinearity coefficient γ. In the normal dispersion

region, with negative γ, there exists a "dark soliton". Optical soliton has been observed in the photonic crystal fiber, which implies the application potential in optical communications [67].

In the case of the higher order dispersion, due to the high dispersive medium or high dispersive device like prism, we add the higher order dispersion term $D = i\sum_{m=3}^{\infty}\frac{\beta_m}{m!}(i\frac{\partial}{\partial t})^m$ into the NSE. In this case, some new frequency waves are generated owing to the perturbation of high-order dispersion. The induced new wave E_d is called the resonant dispersive waves (RDW) [58, 59]. The NSE could be rewritten as

$$\frac{\partial E+E_d}{\partial z} = -\frac{iK_2}{2}\frac{\partial^2(E+E_d)}{\partial t^2} + i\gamma|(E+E_d)^2|(E+E_d) + i\sum_{m=3}^{\infty}\frac{\beta_m}{m!}(i\frac{\partial}{\partial t})^m(E+E_d). \tag{2.12}$$

Compared with the soliton, the energy of the resonant dispersive wave is relatively small, which might be 10% [59] of the incident pulse in some situations. The dynamics of RDW has been carefully studied [68]. If only considering the third order dispersion, there is only one dispersive induced, and if considering the fourth order dispersion, there is a pair of RDWs generated. They are red-shifted and blue-shifted respectively. This make the RDW a possible source to generate femtosecond pulses.

2.4 Spontaneous Raman Scattering and Coherent Raman Scattering

Raman scattering was named after the famous Indian physicist C.V. Raman, who discovered the inelastic scattering of a photon in liquid with K. S. Krishnan [69]. The Raman effect was also discovered independently by G. Landsberg and L.I. Mandelstam [70]. Moreover, it was predicted theoretically by A. Smekal in 1923 [71]. C.V. Raman received the Nobel Prize in 1930 for his work on the scattering of light [72].Raman scattering has been fully described [60, 73].

In general, when a material sample is illuminated by a beam (liquid, solid or gas), part of the light is transmitted, part is reflected, and part is scattered. If the scattered light is observed spectroscopically, most of light has the same frequency as the incident beam, which come from Mie scattering and Rayleigh scattering. A small portion of light has frequencies different from the incident light, which are from inelastic scattering. They are Brillouin scattering, which is an interaction between an electromagnetic wave and a density wave, magnetic spin wave, or other low frequency quasi-particle, and Raman scattering, which results from molecular vibrations, rotations and etc. The scattered light with frequency lower than the incident photon is called Stokes scattering and the scattering with higher frequency is called anti-Stokes scattering. The frequency shifts depend on the materials. For the spontaneous Raman scattering, the Stokes scattering is orders of magnitude more intense than the anti-Stokes scattering.

The energy diagram of Raman scattering is shown in Fig.2.1. Raman scattering happens even when the incident photon is far off-resonant.It entails transition from the state level a (b) to the final level b (a)with n' serving as the intermediate level for Stokes (anti-Stokes) scattering. In thermal equilibrium, there is more population in ground state a than that of excited state b, so that the anti-Stokes is much weaker than the Stokes scattering.

The spontaneous Raman scattering happens randomly in time interval, so that it is incoherent process. However, if some of the scattered Stokes photons are trapped inside the medium, or inputting some Stokes photons with the pump light, it results in stimulated Raman scattering. The total Raman scattering rate is increased sufficient largely compared with the spontaneous Raman scattering. The more Stokes photons are present, the more of Stokes photons are generated. This amplification of Stokes light with pump beam is exploited in Raman lasers [74, 75]. More generally,

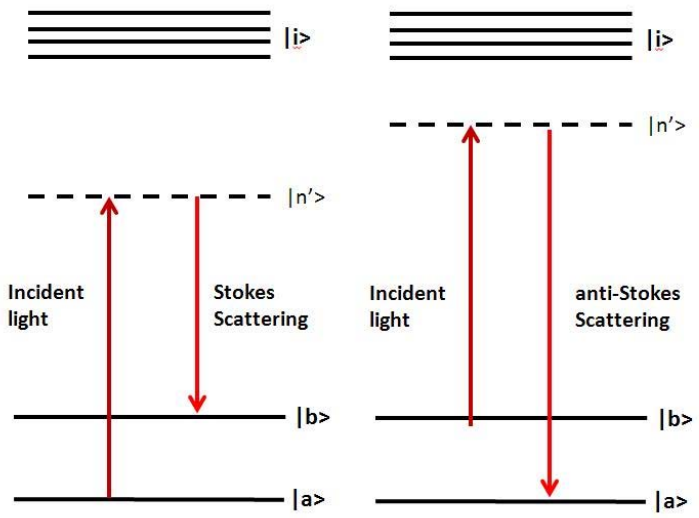

Figure 2.1: Energy diagram for Raman scattering. The left is for the Stokes Raman scattering. The right is for the anti-Stokes Raman scattering. Level n' serves as the intermediate level for Stokes (anti-Stokes) scattering. Levels i are the resonant electronic states.

if a Raman-active molecule is driven into resonance by two incident (off-resonance) fields, the Raman resonance is said to be stimulated. The initial phase of the Raman states is determined by the relative phase difference of the incident pulses. Generally, the spontaneous Raman scattering is very weak. For example, in solid-state medium, the cross-section of Raman scattering is around $10^{-6} cm^{-1} sec^{-1}$. Nevertheless, the stimulated Raman scattering process occurs with a high conversion efficiency of the incident laser, which would close to 10%. Moreover, in spontaneous Raman scattering, the scattering light is in the form of a dipole radiation pattern, whereas the stimulated Raman scattering leads to emission in a narrow cone in the forward and backward direction. Stimulated Raman scattering was discovered by Woodbury and Ng [76]and was described fully by Eckhardt *et al.* in 1962 [77].

Classically, Raman scattering is described using a simple harmonic oscillator of

resonance frequency ω_ν and damping constant γ [60]. In the following, we will briefly go through the theoretical equations, which are adapted from Ref. [60].

The equation of motion describing the molecule vibration is:

$$\frac{d^2\widetilde{q}}{dt^2} + 2\gamma\frac{d\widetilde{q}}{dt} + \omega_\nu^2 = \frac{\widetilde{F}(t)}{m}, \tag{2.13}$$

where $\widetilde{F}(t)$ is the the force that acts on the vibrational mode, and m denotes the reduced nuclear mass.

The key assumption of the theory is that the optical polarizability of the molecule (which is typically predominantly electronic in origin) is not constant, but depends on the internuclear separation $q(t)$ according to the equation

$$\widetilde{\alpha}(t) = \alpha_0 + (\frac{\partial\alpha}{\partial q})\widetilde{q}(t). \tag{2.14}$$

The Stokes polarization with a complex amplitude is given by

$$P(\omega_s) = N\epsilon_0(\frac{\partial\alpha}{\partial q})_0 q^*(\Omega)A_L e^{ik_s z}. \tag{2.15}$$

The Raman susceptibility $\chi^3(\omega_s) = \omega_s + \omega_L - \omega_L$ is defined by the expression

$$P(\omega_s) = 6\epsilon_0\chi_R(\omega_s)|A_L|^2 A_S e^{ik_s z}. \tag{2.16}$$

By comparison, the Raman susceptibility is given by

$$\chi_R(\omega_s) = \frac{\epsilon_0(N/6m)(\partial\alpha/\partial q)_0^2}{\omega_0^2 - (\omega_L - \omega_s)^2 + 2i(\omega_L - \omega_S)\gamma}, \tag{2.17}$$

where γ is the damping constant, N is the density of the molecules and m is the

reduced nuclear mass.

In the slowly-varying amplitude approximation, the evolution of the Stokes field A_S is given by

$$\frac{dA_S}{dz} = -\alpha_S A_S, \tag{2.18}$$

where $\alpha_S = -12\pi i \frac{\omega_S}{n_s c}\chi_R(\omega_S)|A_L|^2$ is the Stokes wave "absorption" coefficient which has a negative real part, implying that the Stokes wave has an exponential growth.

For anti-Stokes (AS) waves, there is a similar expression as Stokes waves. The total polarization at the AS frequency is

$$P(\omega_a) = 6\chi_R(\omega_a)|A_L|^2 A_a \exp(ik_a z) + 3\chi_F(\omega_a)A_L^2 A_S^\star \exp[i(2k_L - k_S)z], \tag{2.19}$$

where $\chi_F(\omega_a) = \chi^3(\omega_a = 2\omega_L - \omega_S)$ is the four wave mixing (FWM) susceptibility. Similarly there is a FWM contribution to the Stokes polarization. Therefore, assuming optically isotropic medium, slowly varying amplitudes and constant pump approximations, the field amplitudes of AS and S fields obey the coupled equations:

$$\frac{dA_S}{dz} = -\alpha_S A_S + \kappa_S A_{AS}^* e^{i\triangle kz}, \tag{2.20}$$

$$\frac{dA_{AS}}{dz} = -\alpha_{AS} A_{AS} + \kappa_{AS} A_S^* e^{i\triangle kz}. \tag{2.21}$$

When the phase mismatching $\triangle k = (2\mathbf{k}_L - \mathbf{k}_S - \mathbf{k}_{AS})$ is small, the FWM term is an effective driving term. Perfect phase matching can always be achieved if the Stokes wave propagates at some nonzero angle with respect to the incident beam.

We have mentioned four wave mixing susceptibility in the above description. FWM is a general term for a process in which a frequency is created from the three other frequencies $\omega_4 = \pm\omega_1 + \pm\omega_2 + \pm\omega_3$. For example, third harmonic generation is a special case of FWM in which $\omega_1 = \omega_2 = \omega_3$, and $\omega_4 = 3\omega_1$. In **coherent**

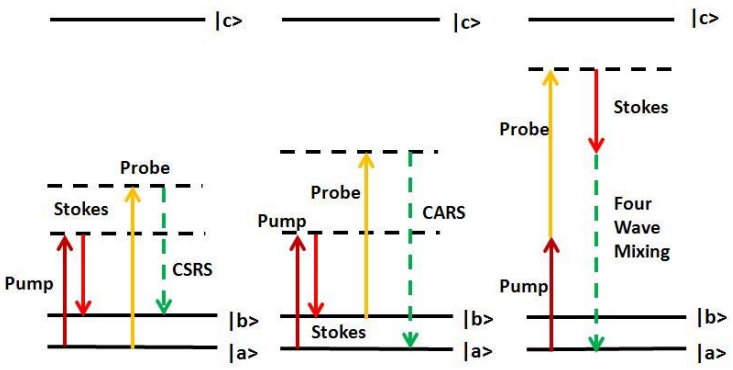

Figure 2.2: Energy diagram for CARS, CSRS and non-resonant FWM. The left panel is for the CARS. The middle panel is for the CSRS. The right panel is for the non-resonant FWM.

anti-Stokes Raman scattering (CARS), a special case of FWM, the two laser field are chosen such that $\omega_1 - \omega_2 = \omega_R$. These two beams generate a coherence for the vibrational molecular states. These molecules act as a nonlinear medium for the generation of AS radiation at $\omega_{CARS} = 2\omega_P - \omega_S$. The intensity I of the CARS signal is [78]

$$I \propto |\chi^{(3)}|^2 N^2 I_1(\omega_1)^2 I_2(\omega_2) \tag{2.22}$$

Here N is the molecular density and $I_1(\omega_1)$ and $I_2(\omega_2)$ are the pump laser intensities. Another similar process is **coherent Stokes Raman scattering (CSRS)** in which a frequency $\omega_{CSRS} = 2\omega_1 - \omega_2$ is generated. The different processes are shown schematically in Fig.2.2. Generally, together with CARS, there is a non-resonant FWM, which is usually taken as a background.

From the detection mode, SRS is different from spanetous Raman, CARS and CSRS. In SRS, the signal is initially present. But in CARS or CSRS, the signal is initially vacant. In SRS, the generation of Stokes field and anti-Stokes field can have higher efficiency, which has been developed in Raman laser[79, 80]. The phe-

nomenon of high-order stimulated Raman scattering simultaneously generated over a wide spectral region is called four-wave mixing Raman (FWRM) [81]. For example, FWRM in crystal $PbWO_4$ has been observed up to 9th order [82].

CARS and CSRS can increase the signal sufficiently compared with the spontaneous Raman. Coherent Raman scattering (CRS) techniques in optical microscopy are becoming popular intimately related to these sufficiently improved signal levels, which have enabled the fast scanning capabilities of CRS microscopes. Moreover, beyond stronger vibrational signals, the coherent Raman interaction offers a rich palette of probing mechanisms for examining a wide variety of molecular properties. When ultrafast pulses are used, CRS methods can resolve the ultrafast evolution of such Raman coherences on the appropriate timescale. CRS techniques also offer more detailed information about molecular orientation than spontaneous Raman techniques. In addition, advanced resonant Raman (coherent or spontaneous) techniques can selectively probe both the electronic and vibrational response of the material, which opens a window to a wealth of molecular information [73]. With adiabatically driving the vibrational molecular states, higher order CARS and CSRS has been observed in gases and solids, which could be a new source for the ultrashort optical pulse [33, 44]. Section III and IV will discuss this subject in detail.

2.5 Theory of Molecular Modulation

As described in the introduction, our technique to generate broadband sidebands in crystals uses two driving fields (pump and Stokes), which are tuned close to the Raman frequency. These two fields prepare the molecular coherence. The theoretical work has been carefully developed by [19, 83]. The theoretical model is briefly described.

The energy diagram is shown in Fig. 2.3. Our formalism is valid in atomic or

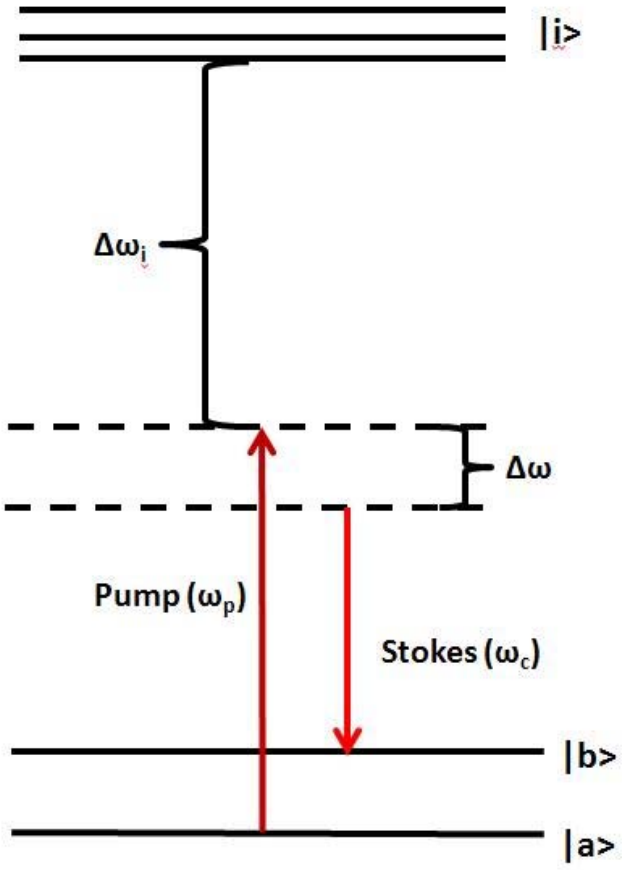

Figure 2.3: Energy diagram for coherent Raman scattering. Laser fields are applied at the frequency ω_p (pump) and ω_s (Stokes) to establish the coherence between the molecular vibrational states.

molecular systems when the detunings of laser fields from the electronic states $|i>$ are larger compared with the Rabi frequencies. The probability amplitudes of these states are small.

In a simple assumption, we consider the one-dimensional propagation fields: $E_p(z,t) = Re(A_p(z,t)exp(j(\omega_p t - k_p z)))$, and $E_s(z,t) = Re(A_s(z,t)exp(j(\omega_s t - k_s z)))$. The quantities A_p, A_s are the complex envelopes of the pump and Stokes laser, which vary with space and time. k_p and k_s are the free space vector.

We assume that each of the states $|i>$ of Fig. 2.3 has nonzero matrix elements to both states $|a>$ and $|b>$. For convenience, we take these matrix elements as real and define (real) Rabi frequencies as $\Omega_{ai} = \mu_{ai}E_p/\hbar$ and $\Omega_{bi} = \mu_{bi}E_s/\hbar$. We do not include the additional background refractive index caused by the fields. In the rotational wave approximation, the equations of the probability amplitudes are

$$\frac{\partial C_a}{\partial t} = j(\sum_i \frac{\Omega_{ai}}{2} C_i)A_p, \tag{2.23}$$

$$\frac{\partial C_b}{\partial t} + j\Delta\tilde{\omega}_b C_2 = j(\sum_i \frac{\Omega_{bi}}{2} C_i)A_c, \tag{2.24}$$

$$\frac{\partial C_i}{\partial t} + j\Delta\omega_i C_i = \frac{j}{2}\Omega_{ai}C_1 A_p^* + \frac{j}{2}\Omega_{bi}C_2 A_c^*. \tag{2.25}$$

Assuming that the derivatives of the probability amplitudes of the upper states $|i>$ are small compared with the detuning from these states and can be neglected. Eq (2.25) could be solved in terms of C_a and C_b and substituting the result into Eqs. (2.23) and (2.24).

In a more general case, we include all possible sidebands, spaced by the modulation frequency ω_m, regardless of whether the fields are applied at the input or are generated during the propagation. The fields could be written as $\omega_q = \omega_0 + q(\omega_b - \omega_a - \Delta\omega) = \omega_a + q\omega_m$, here ω_m is the modulation frequency, which is equal to the difference of the two applied fields. $\Delta\omega$ is the difference between ω_m and the Raman transition frequency, set by the applied field. Therefore, the pump field will be $q = 0$ and the Stokes field will be $q = -1$. Moreover, considering all the rotating terms and non-rotating terms, the equations are written as

$$\frac{\partial C_a}{\partial t} = j\frac{A\hbar}{2}C_a + j\frac{B\hbar}{2}C_b, \tag{2.26}$$

$$\frac{\partial C_b}{\partial t} + j\Delta\bar{\omega}_2 C_b = j\frac{C\hbar}{2}C_a + j\frac{D\hbar}{2}C_b, \tag{2.27}$$

where

$$A = \sum_q a_q |E_q|^2, \tag{2.28}$$

$$B = \sum_q b_q E_q E_{q-1}^*, \tag{2.29}$$

$$C = \sum_q b_{q+1}^* E_q E_{q+1}^*, \tag{2.30}$$

$$D = \sum_q d_q |E_q|^2. \tag{2.31}$$

The terms a_q, b_q, and d_q are

$$a_q = -\frac{1}{2\hbar^2}\sum_i [\frac{|\mu_{ai}|^2}{\omega_{ia} - \omega_q} + \frac{|\mu_{ia}|^2}{\omega_{ia} + \omega_q}], \tag{2.32}$$

$$d_q = -\frac{1}{2\hbar^2}\sum_i [\frac{|\mu_{bi}|^2}{\omega_{bi} - \omega_q} + \frac{|\mu_{ib}|^2}{\omega_{ib} + \omega_q}], \tag{2.33}$$

$$b_q = -\frac{1}{2\hbar^2}\sum_i [\frac{\mu_{ai}\mu_{bi}^*}{\omega_{ia} - \omega_q} + \frac{\mu_{ai}\mu_{bi}^*}{\omega_{ib} + \omega_q}]. \tag{2.34}$$

Hence, we obtain the effective Hamiltonian [84]:

$$H_{eff} = -\frac{\hbar}{2}\begin{bmatrix} \sum_q a_q |E_q|^2 & \sum_q b_q E_q E_{q-1}^* \\ \sum_q b_{q+1}^* E_q E_{q+1}^* & \sum_q d_q |E_q|^2 - 2\Delta\omega \end{bmatrix} = -\frac{\hbar}{2}\begin{bmatrix} A & B \\ B^* & D - 2\Delta\omega \end{bmatrix}. \tag{2.35}$$

This Hamiltonian has included all rotating and non-rotating, cross-transition terms. The constant a_q, b_q, and d_q determine dispersion and coupling [83]. From the general slowly-varying-envelope approximation Eq.(2.7), in this Raman system, the propagation equation for the qth Raman sidebands, in local time, is:

$$\frac{\partial E_q}{\partial z} = -j\eta\hbar\omega_q N(a_q\rho_{aa}E_q + d_q\rho_{bb}E_q + b^*\rho_{ab}E_{q-1} + b_{q+1}\rho^*_{ab}E_{q+1}). \tag{2.36}$$

This equation together with Eq.(4.1) give the conservation of energy and numbers of photon.

We take all sidebands far from the resonance as that in Eq.(2.36), $a_q = b_q = a_0$ and $b_0 = b_q$ and define propagation constant $\beta_q = \eta\hbar\omega_q N a_0$ and change variables by $E_q = \widetilde{E}exp(-j\beta_q z)$, $\rho_{ab} = \widetilde{\rho_{ab}}exp(-j\beta_m z)$. With these approximations and definitions, the Eq. (2.36) becomes

$$\frac{\partial E_q(\omega, z)}{\partial z} = -j\frac{b_0}{a_0}\beta_q(\tilde{\rho_{ab}}\tilde{E_{q-1}} + \tilde{\rho^*_{ab}}\tilde{E_{q+1}}), \tag{2.37}$$

where $\tilde{\rho_{ab}} = \frac{1}{2}sin\tilde{\theta}exp(j\tilde{\varphi})$. φ is given by $B = |B|exp(j\varphi)$, and θ is given by $tan\theta = \frac{2|B|}{2\Delta\omega - D + A}$. Defining $\gamma = \frac{b_0}{a_0}\beta_0 sin[\theta(0)]$, by using Bessel function identities, the analytical solution for Eqs.(4.4) with input fields E_0 and E_{-1} are

$$\tilde{\varphi}(z) = \varphi(0) = arg[E_0(0)E^*_{-1}(0)], \tag{2.38}$$

$$\tilde{\rho_{ab}}(z) = \rho_{ab} = \frac{1}{2}sin\tilde{\theta(0)}exp(j\tilde{\varphi(0)}), \tag{2.39}$$

$$\tilde{E_q}(z) = E_0 exp[j(\varphi(0) - \frac{\pi}{2})q]J_q(\gamma z) + E_{-1}exp[j(\varphi(0) - \frac{\pi}{2})(q+1)]J_{q+1}(\gamma z). \tag{2.40}$$

These solutions are in frequency domain. In time domain, we consider a model that the optical pulses modulated with the molecular frequency ω_m in the medium.

This has been solved analytically. Using the reduced local time $\eta = \tau - z/v + \phi/\omega_m$, the solution is obtained as [85]

$$E(z, \eta) = E_{in}(s)G(\eta). \tag{2.41}$$

The amplitude enhancement factor G is

$$G = \frac{sin(\omega_m s) + \phi}{sin\omega_m \eta} = \frac{1}{e^{\alpha z} cos^2 \frac{\omega_j \eta + \varphi}{2} + e^{-\alpha z} sin^2 \frac{\omega \eta + \varphi}{2}}, \tag{2.42}$$

where E_m is the input field at z=0, $\alpha = 2N\hbar\omega_m d_f \rho_0/\epsilon_0$, and the effective group velocity $v \equiv \omega_m/k$. The input time s is determined from the equation

$$tan[(\omega_m s + \phi/2)] = e^{-\alpha z} tan(\omega_m \eta/2). \tag{2.43}$$

The theoretical work describes the molecular modulation and predicts femtosecond pulses generated using molecular modulation technique, which has been demonstrated in experiments [21, 86].

3. GENERATION OF COHERENT RAMAN SCATTERING IN SOLID MEDIA

In this section, I will describe experiments on the coherent Raman sidebands generation in solid-state medium using femtosecond laser. The molecular modulation was firstly developed in gaseous medium [21]. In the past years, our group has extended it by using femtosecond laser pulse to excite the Raman mode in solid [87]. Generating broadband Raman sidebands in solid-state medium has many advantages. Gaseous medium could have a large Raman frequency shift and negligible dispersion, but the experimental setup are complex and gaseous medium possess lower density compared with solids and thus it needs very long interaction length. On the other hand, solids have a much higher density and can work at room temperature. Also the solid state systems are compact and need less maintenance compared to gaseous systems [88]. The coherent Raman sidebands are generated in different kinds of Raman active crystals, such as diamond, $PbWO_4$, $KGd[WO_4]_2$ (KGW), etc. The coherent Raman scattering in solid-state has some properties as follows [31, 33]. 1) The scattered beams come out at different angles following the phase matching condition. 2) The spectra of the adjacent sidebands overlap. 3) The sidebands are not equally spaced in frequency domain. The frequency spacing between the sidebands decreases gradually.

We select diamond and lead tungstate ($PbWO_4$) for the Raman scattering studies because these crystals have a high Raman gain and they exhibit a broadband transparency ranging from the UV to IR. $PbWO_4$ attracted a lot attention due to its potential use to make the scintillation detector for Large Hadron Collider in 1995 [89]. $PbWO$ has a wide optical transparency from 0.33 to 5.5 μm and a relative large damage threshold. The Raman spectrum of $PbWO_4$ has been studied extensively

[82, 90]. Diamond has an extremely broad optical transparency from 220 nm up to longer than 50 μm. Also, diamond is characterized by its high thermal conductivity. Recently, both $PbWO_4$ and diamond are studied for the Raman laser due to their high Raman gain coefficient [79, 80].

In the experiment of generations of the coherent Raman sidebands, we use a Ti:Sapphire amplifier (Mira+Legend, Coherent) which produces 40 femtosecond pulses with central wavelength at 806 nm and repetition rate of 1 kHz . The pulse from the amplifier is taken as the fundamental beam to pump optical parametric amplifier (OPA). We use two optical parametric amplifiers, which could tune the wavelength from 300 nm to 3000 nm. The Raman transitions are driven off-resonance (adiabatically) with driving lasers of sufficient intensity (The product of Rabi frequencies exceeds the product of the detuning from the resonance of the electronic states and the detuning of the Raman transitions). In order to excite the high gain Raman mode of the different media, we use different configurations to satisfy the requirement for the coherent Raman scattering.

3.1 Coherent Raman Scattering in $PbWO_4$

The coherent Raman scattering by $PbWO_4$ crystal is studied recently [31]. There are several strong Raman transitions for $PbWO_4$ among which the Raman mode at 901 cm^{-1} is the strongest. The linewidth of this mode is $\Delta\nu_R = 4.3\ cm^{-1}$, corresponding to a phonon relaxation time of $T_2 \approx 2.5ps$. The other Raman transitions are at 320 cm^{-1} and 750 cm^{-1}. We excite the Raman mode at 901 cm^{-1}. The fundamental beam is separated into two by a beam splitter. In our previous work [31], about 40% of the beam was used as a pump beam for an optical parametric amplifier (OPA) and the remaining is used to pump another OPA. In the current work, a part of fundamental beam is used to pump an OPA and remaining beam

is used as the pump for the Raman scattering. The second harmonic of the idler beam generated from the OPA has a central wavelength of 870 nm and is used as the Stokes beam. The experimental setup is shown in Fig. 3.1 [Following the coherent anti-Stokes Raman Spectroscopy (CARS) convention, we denote the shorter 806 nm wavelength beam as the pump and the longer wavelength (870 nm) one as the Stokes beam.]

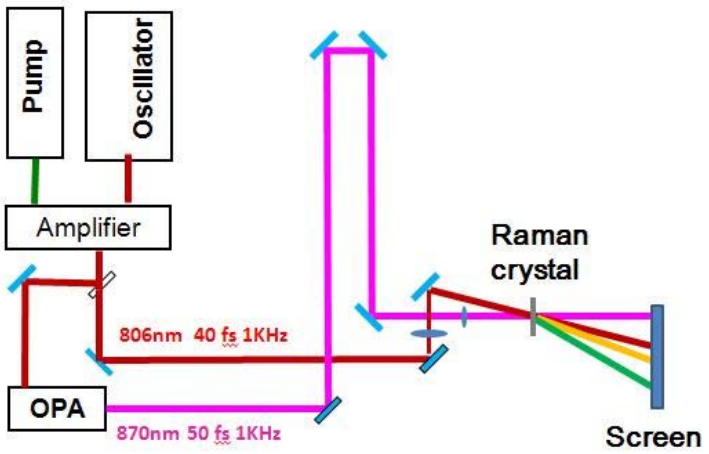

Figure 3.1: Experimental setup to study the coherent Raman scattering from $PbWO_4$ crystal. The 800 nm beam generated from the amplifier is divided into two parts. 40% energy is used as the pump for Raman process. The other is used to pump an OPA. The second harmonic of the idler beam generated from the OPA with a center wavelength of 870 nm is used as the Stokes beam. A white paper screen is used to record the distribution angle of scattered light and to photograph the beam profile.

The pump and Stokes beams with the same polarization cross in the medium at an angle around 3.5^o optimized in accordance with the phase matching and higher order sidebands generation. In the experiment, we use a piece of glass (microscope slide) and $PbWO_4$ for generating sidebands. The first sideband emerging from the

pump beam is labeled as anti-Stokes one (AS1) and the 2nd one is labeled as anti-Stokes two (AS2), etc...

Figure 3.2: The photo of sidebands generated by $PbWO_4$ crystal recorded by a camera. These sidebands have been generated up to 23rd order in anti-Stokes side and at least 2nd order in Stokes side.

In the experiment, we first use 0.5 mm thick $PbWO_4$ Raman crystal. The broadband Raman sidebands are generated at different output angles, determined by the phase matching conditions [31]. The generated spectrum is shown in Fig.3.2 where we can see the anti-Stokes scattering, up to 23rd order. In the Stokes side, the second order Stokes scattering can be seen with the help of infrared card. Between the pump and Stokes beams, there are several small blue spots, which correspond to the four wave mixing among the pump and the Stokes beams. The lower sidebands have more rich structure in spectrum as observed previously [31, 91]. For each individual sidebands, we can clearly see that the beam has a "local" dispersion, which means that the blue-shifted frequency is close to the pump and Stokes, and the red-shifted one is towards the anti-Stokes side. Fig.3.3 shows the relationship between the frequencies and the output angles (the angle is measured with the pump beam as 0 degree). Besides the sidebands which generated through the Raman transition at 901 cm^{-1}, there is yet another set of sidebands produced through the other Raman transition in experiments.

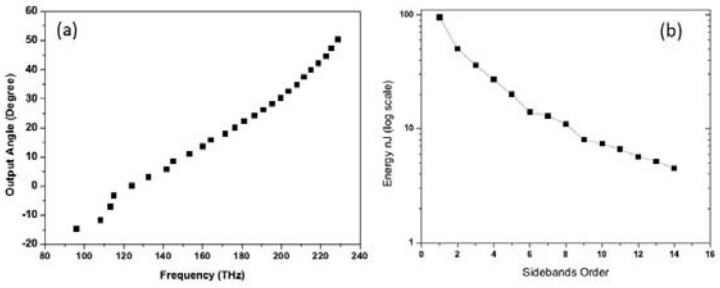

Figure 3.3: (a) The relationship between the output angles and sidebands frequencies. Here the 800nm beam is taken as the reference (0^o). (b) The relationship between the energy of sidebands and the order number, which follows the Bessel function type dependence.

In principle, the frequencies ω_n of the sidebands could be calculated following the relationship $\omega_n = \omega_p + n\omega_R$, where ω_p is the frequency of the pump beam and ω_R is the frequency of Raman transition. In experiments, the frequency difference decreases gradually for the higher order sidebands due to many reasons such as dispersion [31]. Fig. 3.3 is the relationship between the sidebands power and the order, which is in agreement with a bessel function as predicted by theory [22]. The conversion efficiency is nearly 20% with respect to the power of pump pulse.

The angle between the pump beam and Stokes beam is also critical [31]. If the angle between the pump beam and the Stokes beam is decreased, the lower order sidebands will have more power than the higher order sidebands. On the contrary, when the angle is increased, more higher order AS sidebands are generated. Furthermore, there are always more anti-Stokes sidebands than Stokes sidebands. In the phase matching diagram, the vector increases for the higher sidebands (Fig. 3.4(a)). However, on the Stokes side, the k-vectors of the sidebands become shorter for higher order sidebands due to the energy conversation (Fig. 3.4 (b)). As a result, it disrupts the phase matching. Therefore, the high order Stokes sidebands will not

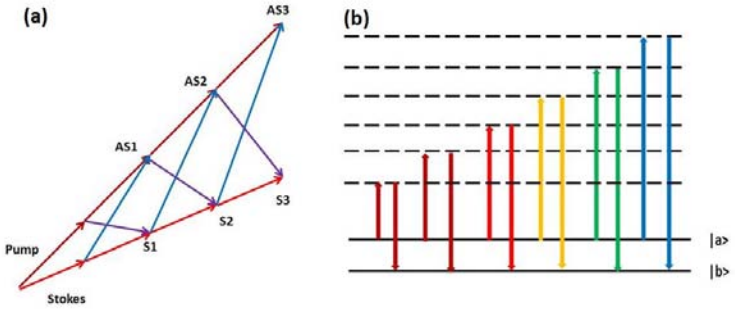

Figure 3.4: (a)The phase matching diagram for the cascade sidebands generation. The vectors of Stokes and anti-Stokes sidebands increase for the higher order scattering. (b) The energy level scheme for the cascade Raman process. For the higher order Stokes scattering, the energy of the photon decrease. For the higher order anti-Stokes scattering, the energy increases.

be generated.

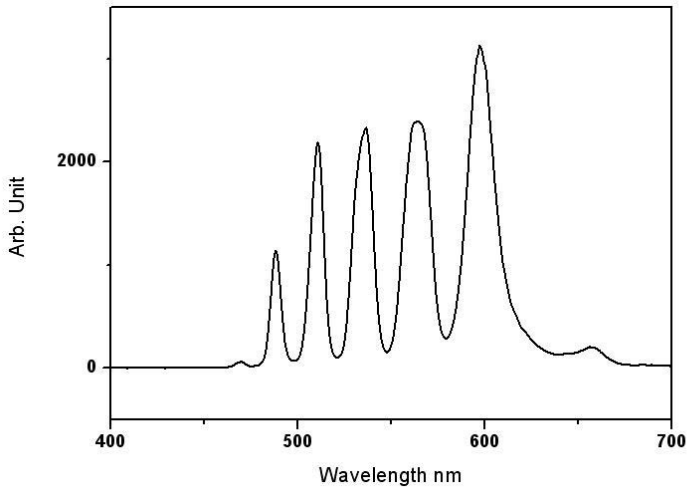

Figure 3.5: The spectrum of coherent Raman sidebands generated from a CVD diamond. Here the pump is 800 nm and Stokes is 902 nm, and AS 3-AS7 are recorded.

For diamond, there is a strong Raman mode at $1332cm^{-1}$. The large Raman

frequency makes the coherent Raman scattering easily to cover a broad spectral range but with a few sidebands. Diamond is also characterized with its high thermal conductivity, good toughness, chemical inertness, and a very good transparency. Figure 3.5 shows a typical spectrum of the sidebands generated from a synthetic single-crystal diamond produced by chemical vapor deposition (CVD).

The sidebands generated in the coherent Raman process are in femtosecond time region. Figure 3.6 is the result of FROG measurement of one sideband generated in diamond, which is accomplished by Phazzler (Phazzler (Fastlite, Fr.) is a device based on Dazzler for the pulse characterization). The broadband spectrum relying on Raman process has a potential to synthesize a few-femtosecond or sub cycle femtosecond laser pulses. So far, molecular modulation is the most successful technique that could provide coherent superposition and manipulation of frequencies over more than an octave in the visible and flanking spectral ranges [92].

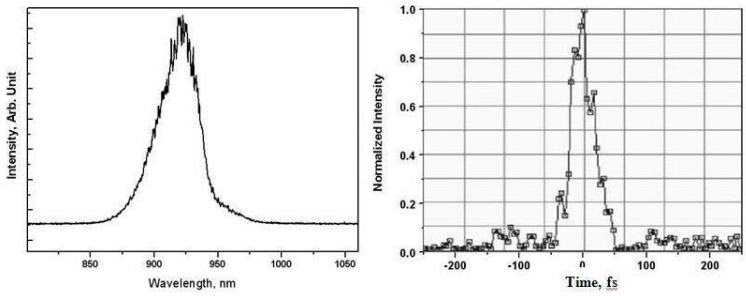

Figure 3.6: The typical spectrum and FROG measurement of AS1 generated from Raman crystal (diamond) using Phazzler (FastLite). The left is the spectrum and the right is the FROG measurement. The center wavelength of AS1 is at 940 nm. The dispersion of the pulse has been corrected by Phazzler. The full-width-half-maximum (FWHM) is measured to be 32.8 fs.

3.2 Spectral Broadening of Coherent Raman Scattering in Solid Medium

In this subsection, we discuss a scheme that allows broadening of the spectrum of coherent Raman scattering sidebands which are generated from a crystal in a double-path interaction scheme. This scheme allows efficient multi-beam interaction as the phase matching conditions among multi-beams are automatically fulfilled. When the relative phases among the sidebands are properly adjusted, the spectrum can be broadened through the second interaction path with relatively low input pulse energy.

Broadband spectrum is one of the essential requirements for generating ultrashort optical pulses, which are used in a diverse range of fields, such as optical coherence tomography [93], frequency metrology [94, 95], fluorescence lifetime imaging [96], optical communications [97], and gas sensing [98, 99]. The spectral broadening is usually accomplished by propagating an initial short optical pulse through the medium with strong nonlinearity. Many techniques are used to broaden the spectrum of a laser pulse. For example, self-phase modulation (SPM) in a photonic crystal fiber is a common technique to achieve a broad spectrum and such fibers have been used to generate supercontinuum [100]. Recently an octave wide spectrum is produced on a chip-scale integrated device by using micro-resonator [101]. High harmonic generation has extended the spectrum to the soft X-ray regime. Nowadays it is the main technique for attosecond optical pulse generation [15].

Molecular modulation is another ultrashort pulse generation technique which has attracted great interest in the last two decades [16]. This technique relies on adiabatic preparation of near-maximal molecular coherence. The resultant coherent molecular motion leads to the generation of a broad spectrum of coherent sidebands [86]. It was first accomplished in gas with nanosecond lasers [19] and has been extended

to femtosecond domain using Raman active crystals [31] and to continuous wave domain using an optical cavity filled with gas [102]. With assistance of a pulse shaper, the arbitrary ultrashort wave form synthesis using Raman sidebands has been demonstrated [35, 41].

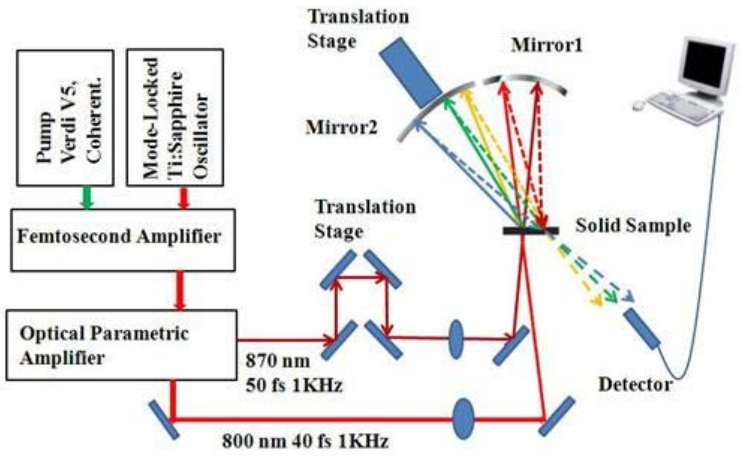

Figure 3.7: Schematics of the experimental setup. Broadband sidebands are first generated by focusing two femtosecond pulses in a solid. The Raman sidebands are reflected back by two spherical mirrors with a focus length of f=10 cm, which leads to further broadening of the spectrum.

In the experiment we use 0.5 mm thick Raman crystal PbWO4. The experimental setup is shown in Fig. 3.7. It is a similar experimental setup to that of last subsection. After the coherent Raman sidebands are generated, we will use spherical mirrors to refocus these beams back to the crystal to a spot which is hundreds micrometers away from the incident spots. The broadband Raman sidebands are generated at different output angles, determined by the phase matching conditions [31]. In our experiment, the pump power is around 16 mW and the Stokes is around 1 mW. The intensity of pump on the crystal is around 1011$\sim$1012 W/cm^2. After the crystal,

the pump and stokes together is around 14 mW. To further broaden the spectrum, one may intuitively want to increase the input pulse energy. However, the maximum allowable pulse energy is limited by damage threshold of the crystal. In addition, other parasitic nonlinear processes such as self-phase modulation will occur as the laser power is increased. Here we use the generated sideband to assist the cascade Raman process to broaden the spectrum thus avoiding the high input pulse energy. Specifically, we use concave spherical mirrors to reflect the beams back to the same crystal. In this configuration, only when the distance between the crystal and the spherical mirror is two times of the focus length of the spherical mirror, the beams are re-focused back to same spot of the crystal. Moreover, the angles between the sideband beams in the second path, which is the reflection path, are the same as the first path, therefore phase matching is automatically fulfilled. Consequently the interaction between the beams is maximized.

In our experiment, we use a spherical mirror with a focal length of 10 cm and keep it about 20 cm away from the crystal. The beams are re-focused back to the crystal with a offset from their incident spots such that two spots are just distinguishable from each other. The relative spectral phases between the beams are important since it determines whether there is generation or elimination of new Raman sidebands [39]. A translation stage is used to finely adjust the distance between the spherical mirror and the crystal. This enables us to adjust the relative spectral phases between these sidebands. In principle, by adjusting the spectral phase of each individual sideband, we could optimize the cascade Raman process to broaden the spectrum and produce the sidebands with the high energy. In our experiments, with only one mirror to adjust the spectral phases of several sidebands altogether, we are still able to find a position where the generation of new sidebands is enhanced. In Fig. 3.8 we show photographs of the beams after the second path. With only one mirror reflecting

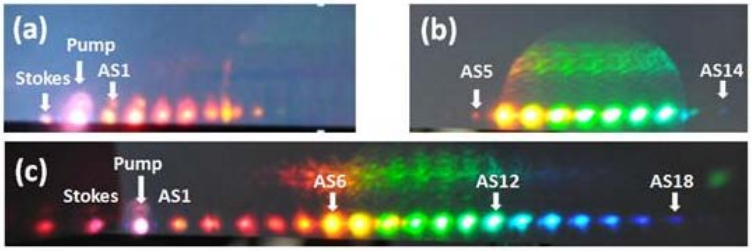

Figure 3.8: The photograph of the Raman generation from $PbWO_4$ reflection back to the crystal taken by a camera. (a) Only pump, Stokes, S1 and AS1 were reflected back with one mirror. S1 was not shown in the figure because it is out of the range of camera. AS2 CAS7 were generated when the other beams overlapped and in phase. (b) AS6-AS12 sidebands were reflected back to the crystal with the second mirror. The small spots outside the shadow of the mirror were the new sidebands generated when AS6-AS12 overlapped and in phase. (c) All the beam including pump, stokes, AS1, S1, and AS6-AS12 were reflected back to the same spot on the crystal with two mirrors and were temporally overlapped. An infrared card was used here to help display S1. AS13-AS18 sidebands were the sidebands generated when two sets of beams overlapped. (d) Energy level schematic of the cascade coherent anti-Stokes Raman process.

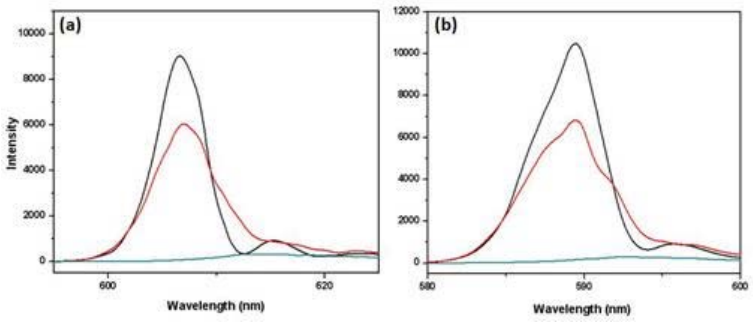

Figure 3.9: Spectrum of sideband AS6 (a) and AS7 (b) using one spherical mirror reflecting beams (pump, Stokes, AS1, AS2, and AS3) back to $PbWO_4$. Black line is the spectrum reflecting back pump, Stokes, AS1 AS2, and AS3. Red line is the spectrum reflecting back pump, Stokes and AS1. Green line is the spectrum reflecting back pump and Stokes.

back the pump, S1 and AS1, the new sidebands AS2-AS7 are generated through the second path. With only the second mirror reflecting back AS6-AS12, the new

sidebands AS4, AS5, AS13, and AS14 are generated when AS6-AS12 overlapped again on the crystal. By fine adjustment of the position of the mirror, the generation of the new sidebands get enhanced at certain point. Now we combine the sidebands by two mirrors and focus them back to the same spot. We keep the position of the second mirror fixed at the place where the generation of the new sidebands was enhanced. By adjusting the position of the first mirror to overlap two groups of beams both in time and space, we observe that the new sidebands AS15-AS18 are generated. At certain position, the intensities of the new sidebands are also enhanced as shown in Fig. 3.8. The detail related to the effect of the spectral phase for the cascade Raman process will be discussed in the next section.

In experiments, we use a spectrometer (Ocean Optics, USB 2000) to observe the change in spectra of the new sidebands when only one mirror is reflecting back the beams. The spectra of AS6, AS7 are shown in Fig. 3.9. Pump and Stokes beams are reflected back into the crystal and generate a few sidebands up to seven orders. When AS1 is reflected back and combined with the pump and Stokes beams, AS6, AS7 intensity are greatly enhanced. Focusing the pump, Stokes, AS1, AS2 and AS3 beams give almost two fold increase in AS6, AS7 intensities. In addition to Raman crystal, we also use a 150 μm glass (BK7) to see whether this scheme works with non-resonant cascaded four-wave-mixing (CFWM) process. The CFWM is similar to Raman process and generates the sidebands with different output angle as well. Between the pump and Stokes, there are several blue spots which also result from four wave mixing (Fig. 3.10). The third harmonic generation due to interaction of pump, Stokes and the four wave mixing between pump and Stokes also take place (Fig. 3.10).

Similar to Raman crystal, we find that when the generated beams and the residual of pump and Stokes are all reflected back and overlapped again at the glass both

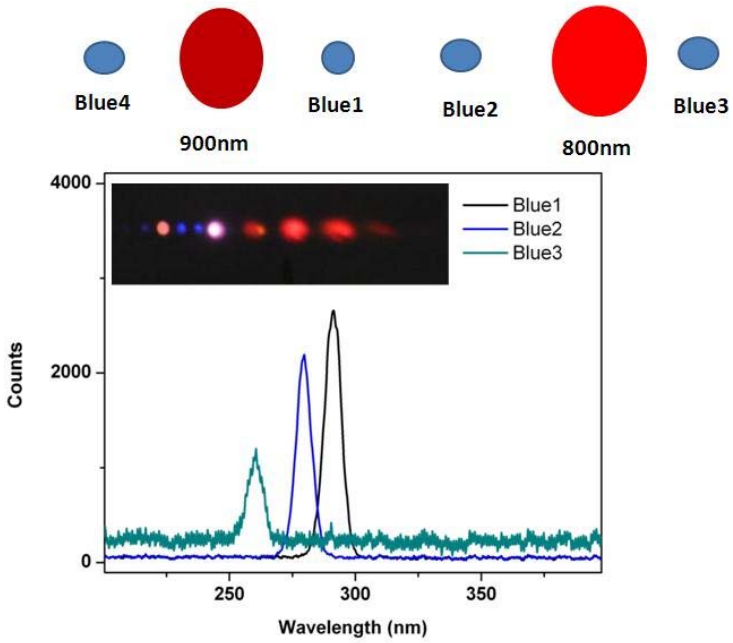

Figure 3.10: The photon of the blue spot generated from glass and their spectrum. The right blue spot between pump and Stokes is the third harmonic generation of pump. The left is the third harmonic of Stokes. The blue spot outside pump is the four wave mixing ($\omega = 2\omega_p + \omega_s$). The blue spot outside Stokes is the other four wave mixing ($\omega = 2\omega_s + \omega_p$)

temporally and spatially, the spectrum is obviously broadened, as shown in Fig. 3.11. The spectrum is extended to UV, which is close to the limit of transmission of the glass.

There are interferences appearing on the beams when they are reflected back to the glass. Fig. 3.12 is the fringe recorded at different position of the second mirror. The interference is the result between the reflected beam generated in the first path and the new generated sidebands on the second path produced by the same pump and Stokes beams. The width of the fringes is changing at different position because the angle between k-vectors of two set of beams is changing when we change the position of one spherical mirror. When the k-vectors of two sets of beams are nearly

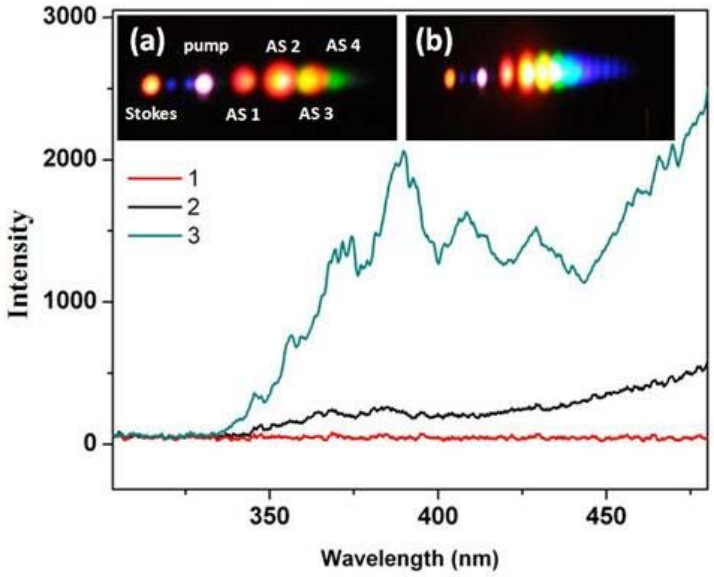

Figure 3.11: The photo and spectrum of sidebands generated in a 150 μm thick glass. (a) The photo of the Pump and Stokes beam and the generated CFWM sidebands in the first path. (b) The photon of the pump, Stokes and all the generated CFWM sidebands when the beams in figure (a) are reflected back to the glass with one spherical mirror. (c) The spectrum at 400 nm when pump, Stokes and other sidebands reflected back to the glass. Line 1 is the spectrum when pump and Stokes in figure (a) are reflected back to the glass. Line 2 is the spectrum when pump, Stokes, and AS1 are reflected back to the glass. Line 3 is the spectrum when all the beams in figure (a) are reflected back to the glass.

overlapped where the width of the fringes is much broader, the beams with new frequencies are generated due to the interaction between the pump, Stokes, AS1, AS2, etc.. Fig. 3.12(c) and (d) clearly show that the new beams are produced at the blue-shifted side.

Moreover, we could generate the optical vortex (OV) in the sidebands using the coherent Raman process [87]. By putting a spiral phase plate on the pump beam, an optical vortex with topology charge (TC) l equal to ± 1 could be produced. It is shaped by a spiral phase plate having an azimuthal structure divided into 16 segments with each step contributing $n\pi/8$ phase shift [103], contained an first order

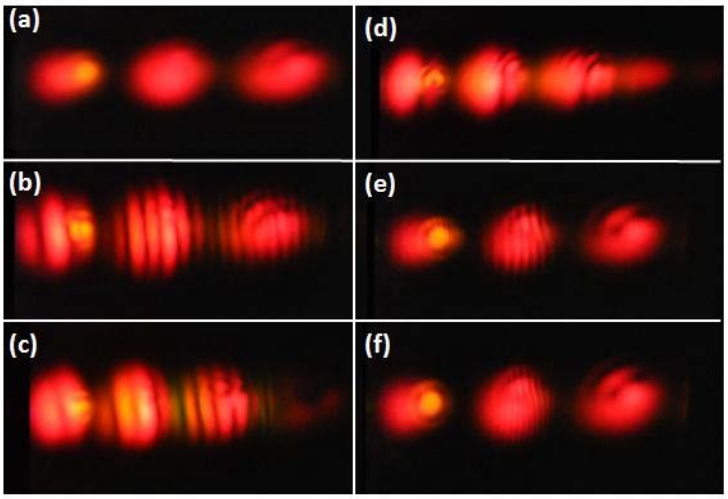

Figure 3.12: The photos of the spatial interference pattern due to the sidebands of the glass after the reflection. (a), (b), (c), (d), (e), and (f) are arranged as we move the spherical mirror close to the glass. The size of fringes is changing because the k-vector of two group beam are changing their overlap. The new sidebands are generated in (c) and (d).

OV ($l = \pm 1$). Optical vortices are the result of orbital angular momentum (OAM) and TC are equal to the OAM of the beam. When the pump beam with TC=1 and a gaussian Stokes beam ($TC = 0$) interact on the crystal, there are optical vortices yielded on the higher order Raman sidebands (Fig. 3.13). The topological charge number of OV follows the algebra $l_n = l_p + n(l_p - l_s)$ [104], where l_n is the TC of the nth AS sideband, l_p is the TC number for pump beam and l_s is the TC number for the Stokes beam. The increment of the beam diameter is an indication of the increment of TC. OV generated in this method can be characterized using the interference between the gaussian beam ($TC = 0$) and the beam with optical vortex ($TC \neq 0$) [34, 35]. Since this is a coherence process, in principle, it would be possible to synthesize the subcycle optical vortices using our setup [35].

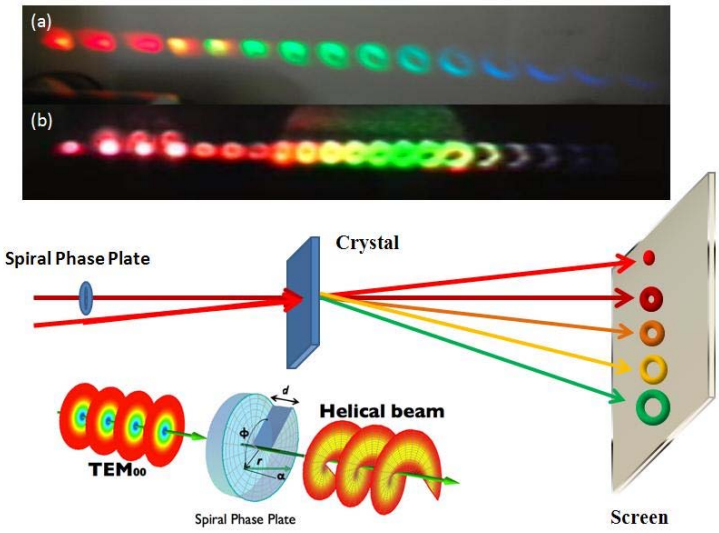

Figure 3.13: The setup to generate optical vortex on the coherent Raman sidebands. A spiral phase plate is inserted into the beam path. The pump beam, shaped by a spiral phase plate having an azimuthal structure divided into 16 segments with each step contributing $n\pi/8$ phase shift [103], contains an OV $l = \pm 1$. (a) The optical vortices generated on the coherent Raman sidebands. (b) The optical vortices generated in the reflection scheme, when the pump, Stokes and other sidebands combine together. In the reflection scheme, besides the generation of new sidebands, the vortices are also produced through the interaction.

4. ULTRAFAST WAVEFORM SYNTHESIS USING COHERENT RAMAN SIDEBANDS

The synthesis of the ultrafast waveform is significant for ultrafast science. Usually, the broadband pulses are generated through highly nonlinear light-matter interaction. The pulse obtained is not Fourier-transform limited so that researchers need to correct the phase distortion in order to get the ultrafast optical pulse. In some case, a special designed optical field would be required during the research; therefore, people need to manipulate both the amplitude and phase of the optical pulses in frequency and time domain.

The pulse shaping techniques are to synthesize the user-specified ultrashort pulse fields by means of parallel manipulation of optical Fourier components [105]. Now it has been widely adopted [106–111]. Pulse shaping has been used widely in Raman spectroscopy such as to suppress the background [112] and to optimize the CARS signal [113]. It could also help to accomplish the quantum control in the liquid phase [108]. Combined the pulse shaping and optimization algorithm to control and optimized the chemical reactions [109, 111]. Molecular motion could also be manipulated using femtosecond pulse sequences [106]. In high-harmonic generation, it has been demonstrated that the shaped pulse could be used to optimize the generation of the soft X-ray [110]. There are many schemes for ultrafast waveform shaping. Using the pulse shaper based on LCM is the most common techniques [105], which could manipulate the spectral comb line-by-line [114] or manipulate arbitrary ultrafast waveform using the coherent Raman sidebands[41]. However, using LCM will require a relative complex system. Recently people proposed several simple schemes to synthesize the ultrafast waveform by using multicolor pulse synthesis technique

[92] or inserting multiple transparency dispersive materials into the optical path to assist the ultrafast waveform synthesis [115].

Using the sidebands generated in solid as a source for the ultrafast optical pulse, we face the challenge to combine the sidebands into the ultrafast waveform. The coherent Raman sidebands generated in solid come out with different angles so that one challenge is to combine them into a single beam and the other is to adjust their spectral phases. People have proposed some schemes to accomplish this goal. For example, Matsubara *et al.* used a prism to combine the sidebands and obtain 14 fs pulses [45] due to the near linear relationship between the output angle and frequency. However, they compensated the phases mainly by adjusting the distance between the prism and the focusing spherical mirror. As a result, the phase could not be completely compensated or flexibly controlled.

We address this challenge by combining manual phase adjustment with programmable pulse shaping in experiments. In the first subsection, I report our experiment of coarse, manual phase adjustments and fine-tuning of spectral phases with the assistance of the pulse shaper based on AOPDF. In the second subsection, I present a new reflection scheme to characterize and synthesize ultrafast waveforms with the assistance of the pulse shaper based on DM. We demonstrate that our scheme is capable of synthesizing the ultrafast waveform using coherent Raman sidebands

4.1 Ultrafast Waveform Shaping Using AOPDF [1].

In Section III, we showed that the sidebands generated in crystals have broad spectrum but did not come out collinearly. Therefore, aiming to synthesis the ultra-

[1*] Part of this subsection is reprinted with permission from "Generation of femtosecond optical vortices by molecular modulation in a Raman-active crystal," by Miaochan Zhi,Kai Wang, Xia Hua, and Alexei V. Sokolov, OPTICS LETTERS 36(20), 4032-4034 (2011), and "Shaper-assisted phase optimization of a broad "holey" spectrum." by Miaochan Zhi,Kai Wang, Benjiamin D. Strycker, Xia Hua, and Alexei V. Sokolov, OPTICS EXPRESS 19(23), 23400-23407 (2011), Copyright 2011 by Optical Society of America

short waveform using the coherent Raman sidebands, we not only need to correct "local" phase distortions on each sideband, but also need to "globally" adjust the relative phases of the sidebands. The devices which could accomplish this goal is pulse shaper, which could manipulate the ultrashort waveform spectral line by spectral line. In this subsection, I report a demonstration of ultrafast waveform shaping using the pulse shaper Dazzler based on AOPDF.

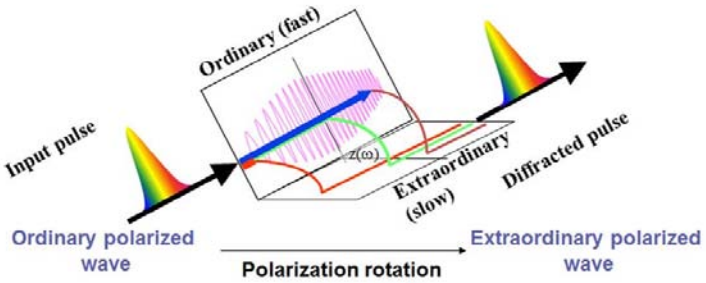

Figure 4.1: The sketch of how the dazzler works. The input beam is along the ordinary axis and the diffraction beam is along the extraordinary beam. The sound wave will behavior like a Bragg grating due to the change of the refractive index induced by compression and decompression. The output beam is slightly off from the incident direction.

Using Dazzler for pulse shaping, it does not require to separate the frequency component with dispersive device. Dazzler works with the collinear incident beam Fig. 4.1. The polarization of the input beam is along the ordinary axis of the crystal (TeO_2). The diffraction beam, the shaped beam, is along the extraordinary axis. It is similar to an acousto-optic modulator, in the sense that it uses sound waves as a diffraction grating. As the longitudinal sound wave propagates through the medium, the compression and decompression of the crystal lattice slightly change the index of refraction at those points, causing the incident intense beam to act as

hitting a Bragg grating if its wavelength is corresponded with the period of the sound wave. The intensity of the sound wave determines how much of that input spectrums wavelength will be diffracted. The diffracted beam is the one we are shaping.

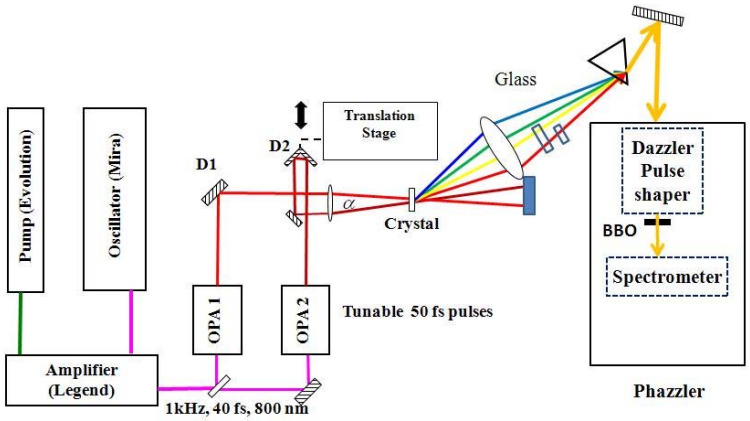

Figure 4.2: Schematics of the experimental setup. In our experiment, a spherical mirror (instead of a lens) is used to focus the Raman sidebands to the prism in order to minimize dispersion. The glass plates are inserted (and tilted as needed) so as to coarse-tune the spectral phases, thus producing a waveform pre-compensated for pulse shaping by Dazzler.

The schematics of the experimental setup is shown in Fig. 4.2. We obtain 50 fs pump pulses centered around 1200 nm (Stokes) and 1035 nm (pump) with 1 kHz repetition rate from two computer-controlled optical parametric amplifiers (OPA). The pump and Stokes beams are focused and crossed at an angle of 3.7^o into a 1-mm thick synthetic single-crystal diamond. The sidebands are combined to a single beam by a prism and then sent to a pulse shaper. We focus on the first five orders of anti-Stokes (AS) sidebands. The center wavelengths of these sidebands (from AS1 to AS5) are 930 nm, 840 nm, 780 nm, 720 nm, and 680 nm, respectively.

Combination of manual and computer controlled pulse shaping is an essential

ingredient in our work. The pulse shaper has limited pulse shaping bandwidth and limited temporal pulse shaping window. As the first step, we precompensate the delays among the sidebands by adding different amounts of glass in each sideband beam path Fig. 4.2. Then the resultant single beam is sent in to a programmable pulse shaper for fine-tuning. The pulse shaper (Phazzler, FastLite) is based on an acousto-optic programmable dispersive filter, which allows compact, in-line and high efficiency pulse shaping and pulse characterization [116]. Phazzler is a pulse characterization device, which is a combination of Dazzler and FROG. We use the experimental setup inside Phazzler but we will not use the FROG or other pulse characterization technique of Phazzler.

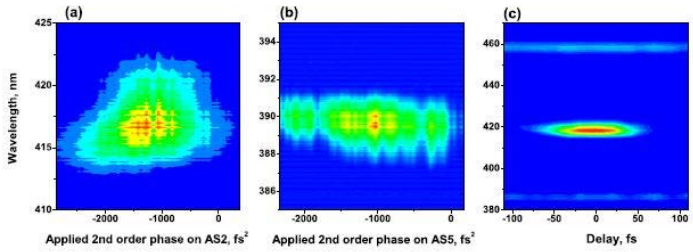

Figure 4.3: (a) SHG of AS2 spectrum as a function of applied second-order phase on AS2 sideband. (b) SFG of AS1 and AS5 as a function of applied second-order phase on AS5. (c) SFG of AS1 and AS3. Zero delay between the sidebands is defined to coincide with the strongest SFG position.

The shaped beam is incident on a BBO crystal and we use the nonlinear signal to assist ultrafast waveform synthesis using coherent Raman sidebands. The second harmonic generation (SHG) spectrum has a local maximum when the second order phase distortion equals zero [117]. In step 2 we measure the second order phase distortion by recording the SHG of each sideband as a function of applied second

order phase. Then we compensate the second order phase distortion by the pulse shaper.

We start by compensating linear chirp (second-order) phase for each sideband. Here as an example, in Fig. 4.3(a) we show the spectrum of SHG of AS2 as a function of the applied second-order phase. After we integrate the intensity over the spectral width, we find that it has a maximum at -1250 fs2. We then apply a 1250 fs2 chirp to AS2 to compensate this second-order phase distortion. The higher-order phase distortions are relatively small so no compensation is required. The compensation of AS5 second-order phase distortion is not so straightforward, as the pulse energy of AS5 is about 3 orders of magnitude smaller than that of AS1 [87]. It is too weak to measure the SHG of AS5 individually, with the sensitivity of our spectrometer. To circumvent this problem, we use the SFG between AS1 and AS5: we compensate the secondorder dispersion by maximizing the SFG signal, as shown in Fig. 4.3(b). This SFG between sidebands is also used to find the temporal overlap between the sidebands. One example is given in Fig. 4.3(c), where we show the SFG between AS1 and AS3. Zero delay is defined at the point where maximum SFG signal is generated.

Next in the step 3, we use the pulse shaper to overlap all 5 sidebands in time, by measuring the sum frequency generation (SFG) signal between the sidebands. In the last step, we adjust the relative phases of the sidebands by using the coherent beating between the SFG of the AS n-1 and AS n+1 and the SHG of AS n (with n being the sideband order). First, we vary the phase of the AS 3 and record the sinusoidal change of the intensity at the SHG of AS2 peak, which is a result of the beating between SHG of AS2 and SFG of $AS1\&AS3$. Theoretically, the peak intensity of the SHG of AS2 varies as $cos(2\phi_2 - \phi_1 - \phi_3)$, where ϕ_1, ϕ_2 and ϕ_3 are the spectral phases of each sideband, respectively. We set the AS2 phase such that we obtain

constructive interference at the SHG of AS2 peak. Then we add AS4 in and vary AS4 phase until we again achieve maximum peak intensity at the SHG of AS3 peak, when constructive interference between SHG of AS3 and SFG of $AS2\&AS4$ occurs. Finally we let AS5 in and adjust the AS5 phase similarly. A flat relative phases of the five sidebands is thus achieved, which is sufficient to produce Fourier-transform limited pulses [118]. This part of the method is similar to the one that was used by Chen *et al.* [118].

To verify that we have achieved the flat spectral phase and to show that we can fully control the sideband phases, we record the SHG spectrum after the BBO crystal as we vary AS2 phase for two cases: (a) all 5 sidebands are in phase and (b) AS3 is ϕ out of phase with the other 4 sidebands at the beginning of the scan when $\phi_{AS2} = 0$. The results are shown in Fig. 4.4. For case (a), all spectral components have maxima when all sidebands are in phase [dotted lines in Fig. 4.4 (a)]. The beating at the position of SHG of AS3 is a result of interference between the SHG of AS3, SFG of AS1 & AS5, and SFG of AS2 & AS4. Specifically, the field amplitude in this spectral region is proportional to $A1 * cos(2\phi_3 - \phi_2 - \phi_4) + A2 * cos(2\phi_3 - \phi_1 - \phi_5) + A3 * cos(2\phi_1 + 2\phi_5)$ (A1, A2 and A3 are determined by the amplitudes of the Raman sidebands). The tilt in the spectra of subband C (SHG of AS2) and subband D (SFG of AS1 & AS4 and AS2 & AS3) is due to the residue chirp on AS1, which results from selecting part of the AS1 spectrum that are centered at 910 nm by the pulse shaper. This way we can achieve the best contract ratio of the coherent beating on the center-band (subband E). In Fig. 4.4 (b) we show theoretical plots of the spectral dependence on the AS2 phase. We assume all the sidebands are in phase and have the same amplitude 1 except AS5, whose amplitudes is set to 0.1. We add negative chirp to AS1 sideband to match the experimental result. We can see the experimental result agrees well with the theory.

When AS3 is π radians out of phase with the rest of 4 sidebands, at multiple integers of 2π positions the π phase shift of AS3 leads to an interchange in the positions of the peaks and nulls in the intensities of the subband C D and F as we vary AS2 phase, as shown in Fig. 4.4 (c) (theory) and (d) (experiment). Again, the experimental result coincides well with the theoretical simulation, which demonstrates the degree of control and predictability we have in our experiment. In Fig. 4.4 (f) and (g) we show two electric fields for the two experimental runs [Fig. 4.4 (a) and (d)] with $\phi_{AS2} = 0$. The first one gives a Fourier-transform-limited (FTL) pulse with less than 3 optical cycles duration. The second pulse has a more complex envelope. The electric field is calculated by Fourier-transforming the spectrum which is taken from the experimental measurement. Furthermore, when varying ϕ_{AS2}, we in essence perform a cross-correlation measurement between two periodic waveforms synthesized by AS2 and AS4 (moving) and by AS1,3 and AS5 (stationary). Both waveforms have the same period [$T = 2\pi/(\omega_{AS4} - \omega_{AS2}) \doteq 17fs$, where ϕ_{AS2}, ϕ_{AS4} are the sideband frequencies], and the first waveform is delayed with respect to the second by $\phi_{AS_2/2\pi}T$. The total spectral intensity of the SHG of all sidebands can be used to measure the pulse duration, similar to how multi-photon ionization was used to characterize single cycle pulses [44]. It is plotted as a function of the AS2 phase, in Fig. 4.4 (e). The peak width is 0.4π, which corresponds to 3.4 fs. The shorter pulse duration than that of FTL pulse [Fig. 4.4 (f)] may be due to the nonlinearity of the measurement. The trace of the total spectral intensity of the sidebands for case (b) [Fig. 4.4 (h)] also resembles the envelope shape of the calculated electric field of [Fig. 4.4 (g)].

We also explore how the coherent beating of the subbands varies as we scan AS1, AS2 and AS3 phases. When all 5 sidebands are in phase, the coherent beating for each subband as a function of the AS2 phase (Fig. 4.4(a)) is similar to a situation

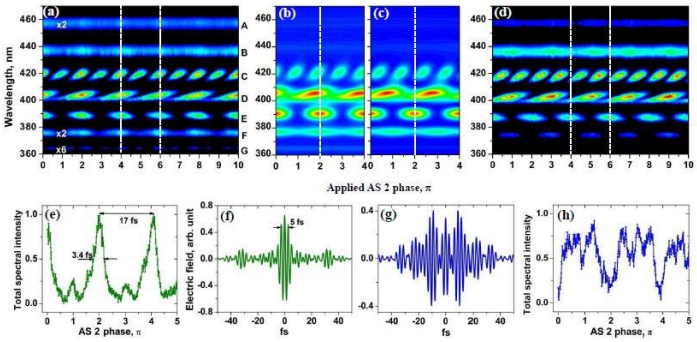

Figure 4.4: The SHG spectrum of the 5 sidebands after the BBO crystal as we vary the AS 2 phase from 0 to 10π, after we adjust the relative phase among all sidebands to be equal [(a) and (b)] or when AS3 is π out of phase with respect to the other 4 sidebands [(c) and (d)]. Subband A, C, G: SHG of AS1, 2 and 4, respectively; B: SFG of $AS1\&2$; D: SFG of $AS1\&4$, and SFG of $AS2\&3$; E: SHG of AS3, SFG of $AS1\&5$, and $AS2\&4$; F: SFG of $AS3\&4$. (b) and (c): Theoretical simulation of (a) and (d). (f) and (g): Electric field of pulses calculated for (f) when all sidebands are in phase, and (g) when AS3 is π out of phase with respect to the other 4 sidebands. (e) and (h): Phase dependence of the total spectral intensity after the BBO crystal for cases (a) and (d), which gives an indication of the pulse duration, as discussed in the text.

when AS3 phase is scanned, as shown in Fig. 4.5. The main difference is that, compared to the other subbands, the fringes have a doubled frequency for SHG of AS2 when AS2 phase is scanned, while the fringes have a doubled frequency for SHG of AS3 when AS3 phase is scanned. The SHG/SFG subband intensities vs AS1 phase are shown in Fig. 4.5(c). Due to shorter integration time of 500 ms (in all other scans, we do two scans with integration time of both 500 ms and 5000 ms) we can not distinguish the beating for SHG of AS1. However, we observe that the sidebands beat in unison and produce a perfect coincidence of the central 4 subband patterns (C, D, E, and F).

We note that a slight sideband phase shift (with respect to flat phase) can lead to a large shift of the center fringe pattern (subband E). Specifically, when the phase is

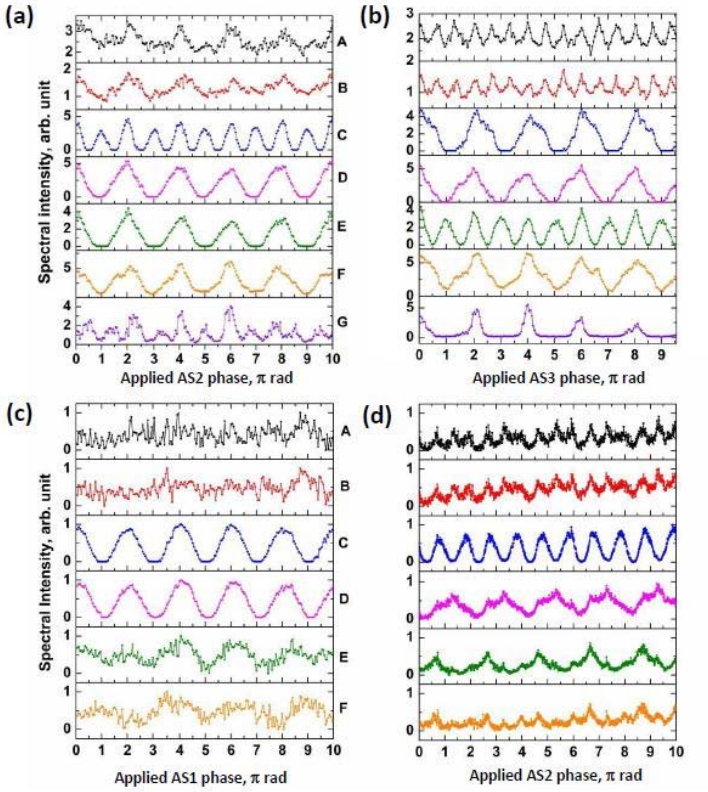

Figure 4.5: The peak intensity of the SHG/SFG subbands as we vary the AS2 phase (a), AS3 phase (b) and AS1 phase (c) from 0 to 10 π, after we adjust the relative phases among all sidebands to be equal. (d) The peak intensity of the subbands as we vary the AS2 phase from 0 to 10 π when the sideband phases are not perfectly flat. Step size is 0.01 π in (d) and 0.05 π in (a), (b) and (c).

not flat, patterns at SHG of AS3 are shifted by a phase which is not only determined by the phase difference among sidebands, but also the relative amplitudes of the sidebands. Therefore, it is crucial to scan up to 10 radians of phase change with a step of at most 0.05π when one obtains the relative phase between the sidebands, as shown in Fig. 4.5(c) and (d). Then, with the sinusoidal fitting, an accurate relative phase between the sidebands can be determined. One example of the shift of the peaks due to this non-flat spectral phase is shown in Fig. 4.5(d). Large phase error occurred when we determined the relative phase between the sidebands using only

2 cycles (phase scan up to π rad). The phase shift on subband E is close to in this example, where we estimate we have up to 0.2π phase error on each sideband.

In conclusion, we demonstrate the mutual coherence of the spectral sidebands generated through molecular modulation in diamond, and show our capability to control spectral phases in a precise and stable manner, in a setup which combines manual, course adjustment of individual sideband phases with programmable pulse shaping and fine phase (and amplitude) tuning across the full spectrum. The good agreement between theory and experiment allows us to synthesize well-controlled and predictable temporal waveforms.

Although the work is focused on 5 sidebands only, this method in principle can be extended to many more spectral lines. Moreover, it can also be applied to other frequency combs such as harmonics that are generated from OPAs [119]. Significant advances toward single-cycle pulse generation and non-sinusoidal field synthesis can be obtained when two (or more) pulse shapers covering adjacent spectral ranges are used. The non-traditional fields will find application in many areas of ultrafast science, such as coherent control [120].

4.2 Ultrafast Waveform Synthesis and Characterization in a Reflection Scheme

In Section III, we design a reflection scheme which takes advantage of spherical mirrors to preserve the phase matching angles between sidebands. We reflect the sidebands and the driving fields back to the Raman crystal and we find that interactions between these sidebands depend on the relative spectral phases. If we use two spherical mirrors to reflect the pump and Stokes beams and the other higher sidebands separately, the intensities of the sidebands would oscillate as we adjust the spectral phases by scanning the position of the spherical mirror with translation stage. We record the spectrum of the sidebands as a function of the mirror position

and it yields a 2D interferogram, which is essentially an XFROG based on Raman nonlinear interaction. We retrieve the relative spectral phases from this spectrogram with a theoretical simulation.

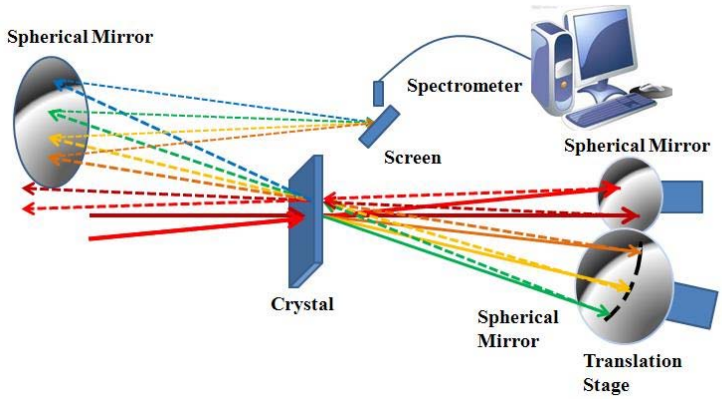

Figure 4.6: Experimental setup. Pump and Stokes beams are crossed on the Raman active crystal. Two concave spherical mirrors are used to reflect beams back to the crystal. One mirror reflects back pump and Stokes beams. And the other reflects back the higher order Raman sidebands. Two groups of beams are overlapped again on the crystal and interact with each other. Then the beams are collected with another spherical mirror and the spectrometer is used to record the spectrogram from a scattering at the focal point.

The experimental setup is nearly the same as that we have described in Section III (Fig. 4.6). It consists of a Ti:Sapphire amplifier which outputs 40 fs pulses with center wavelength at 806 nm and 1 kHz repetition rate. The beam is divided into two by a beam splitter. About 40% of the beam is used as pump beam and the rest is used to pump an optical parametric amplifier (OPA). Second harmonic of the idler beam generated from the OPA with a center wavelength of 902 nm is then used as the Stokes beam. The pump and Stokes beams are focused and crossed at an angle of 3.7^o into a 1 mm thick synthetic single-crystal diamond to excite the Raman mode

at 1332 cm^{-1}. The properties of the coherent Raman sidebands generated can be found in Ref. [121]. In our current experiment, we generate the sidebands up to AS9 with a lower input energy. We optimize the generation to suppress the unwanted nonlinearity and thus obtain a relatively clean spectra of the sidebands.

The concave spherical mirrors with the focal length of 10 cm are used. We call the reflection path as "the second path". The original path to generate the sidebands is the first path. When the pump and Stokes are reflected back together, they could generate the sidebands just as the first path. However, because the reflection spot is off from the incident spot in experiments, the focus condition is different from the first path and the power is also not the same. Therefore, the generation of sidebands is less efficient compared to the first path. By reflecting back sidebands together with the pump and Stokes beams using two concave spherical mirrors, the spectrum is broadened under certain condition as we discussed in the previous section.

The phases of sidebands are very important in the Raman interaction [22]. In principle, we could optimize the interaction by adjusting the phase of each individual sideband separately. This will require a micro-mirror array. In our experiment, we use only one spherical mirror to reflect back several sidebands together, which will change the phases together. In this case, in the experiment, we practically find a proper position, which is corresponding to proper spectral phases, to enhance the interaction. After finding the proper position for one mirror, we fix it. Then we adjust the second mirror to an appropriate position where the beams reflected back by two mirrors interact with each other. The spectrum is then recorded with a spectrometer as a function of the scanning. Scanning the position of one mirror for about tens of micrometers is corresponded to a time delay that is around hundreds of femtoseconds.

The crystal diamond is used in the experiment. The first mirror reflects back the

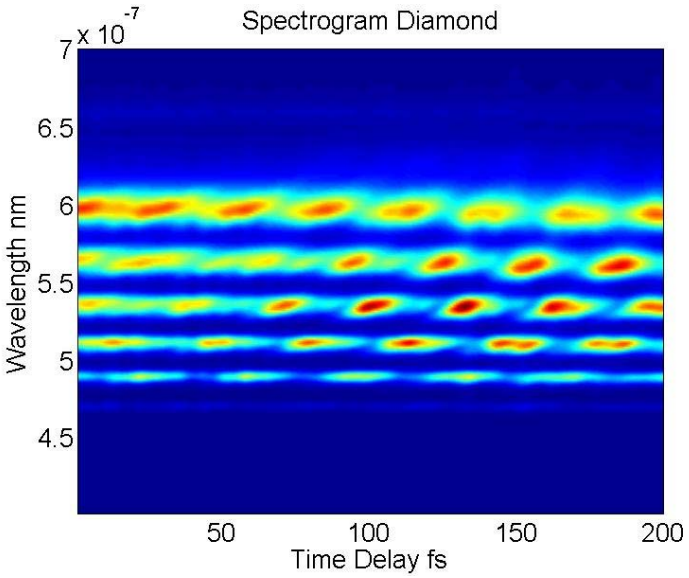

Figure 4.7: The 2D interferogram produced in the diamond. The x-axis is the scanning position of the spherical mirror. It is displayed as the time delay corresponding the the other spherical mirror, which reflects back the pump and Stokes beams. Zero time is arbitrary. The y-axis is the wavelength. We record the scattering using spectrometer (HR2000,Ocean Optics). Five sidebands AS3-AS7 are recorded. There is an intensity oscillation on the spectrum. This 2D interferogram is essentially an XFROG trace.

pump and Stokes beams and the second mirror reflects back the sidebands AS3-AS7. The resultant spectrum at 400 - 600 nm is shown in Fig. 4.7. When only one sideband is reflected back on the second mirror, the first order coherent Raman scattering occurs along with the cross phase modulation due to the interaction between the sideband and the intense pump and Stokes beams. If we reflect back two adjacent sidebands on the second mirror, the intensity of the coherent Raman sidebands will oscillate when we scan the position of one mirror. The frequency of the oscillation (or beating) on the spectrogram is nearly equal to the central frequency separation of two adjacent sidebands. This is clearly shown in Fig.4.8.

If we reflect back the sidebands which are not adjacent, the oscillation of inten-

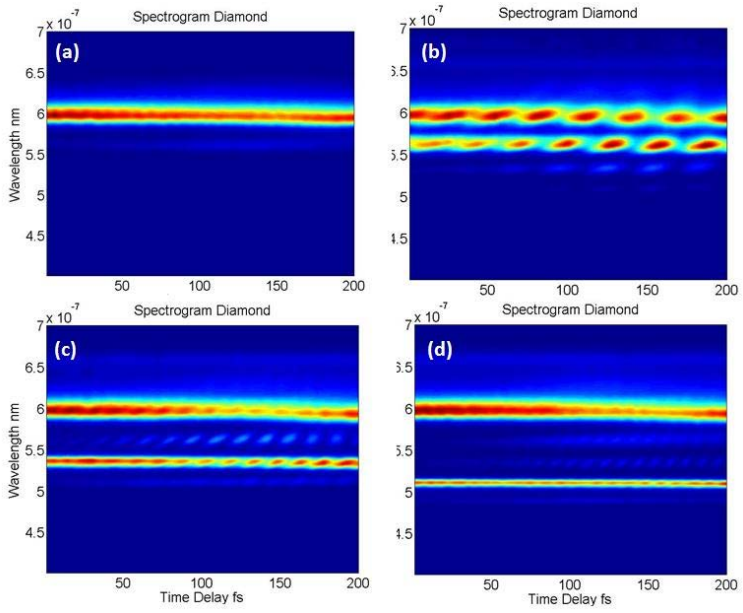

Figure 4.8: 2D interferogram obtained in diamond with different sidebands. (a) is the spectrogram generated with AS3, pump, and Stokes beams. (b) is the spectrogram generated from only AS3, AS4 and pump and Stokes. (c) is the spectrogram generated with AS3 and AS5. The bottom right is the spectrogram generated with AS3 and AS5. It is clear that there is an intensity oscillation on the new generated beam at the frequency of AS4 between AS3 and AS5. (d) is the spectrogram generated with AS3 and AS6. Two orders of Raman scattering occur for AS3 and AS6, which generate the new frequency beams at AS4 and AS5. There are oscillations of intensities on the generated Raman sidebands.

sities still occurs but with a different period. In Fig. 4.8(c), it is shown that when AS3 and AS5 are reflected back, the intensity oscillation can not be clearly seen on AS3 and AS5, but can be clearly seen at the frequency of AS4 even though AS4 is absent. This is because AS3 produces anti-Stokes Raman scattering to generate a sideband at the frequency of AS4 and AS5 produces Stokes scattering that generates a sideband at the frequency of AS4 as well. The generations from these two channels lead to the intensity oscillation at the frequency of AS4. The oscillation frequency is nearly equal to the frequency difference between AS3 and AS5. Even if we choose

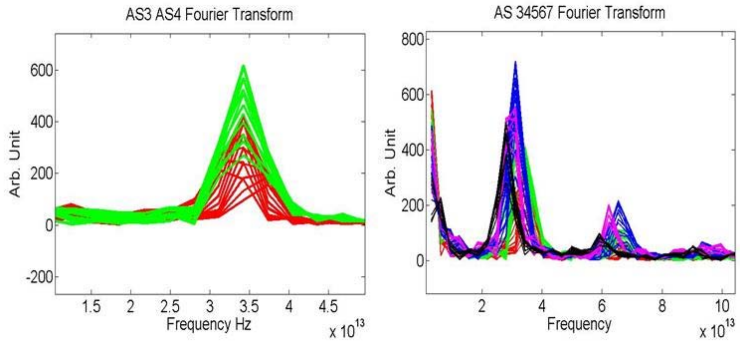

Figure 4.9: Fourier transform of the spectrogram at different wavelength. (a) is the Fourier transform of the spectrogram generated by AS3 and AS4. Red curve is from different wavelength of AS 3, while green curve is from different wavelength of AS4. The oscillation frequency is nearly the same, which is around $3.5 \times 10^{13} Hz$. (b) is the Fourier transform of the spectrogram generated by AS3, AS4, AS5, AS6, and AS7. Red curve is from different wavelength of AS3. Green curve is from different wavelength of AS4. Blue curve is from different wavelength of AS 5. Magenta curve is from different wavelength of AS6. Black curve is from different wavelength of AS7. The beating frequency is different for the higher order sidebands. Moreover, there are also higher frequencies at around $7 \times 10^{13} Hz$ and $19 \times 10^{13} Hz$, which come from the interaction of sidebands which are not adjacent.

AS3 and AS6 (Fig. 4.8(d)), there is still an intensity oscillation appearing at the wavelength AS4 and AS5, with a frequency close to the frequency difference between AS3 and AS5. We need to emphasize that this intensity oscillation will not occur if the pump and Stokes are not refocused back to interact with sidebands. Moreover, diamond has a high gain for Raman scattering. When the coherent Raman scattering occurs, it suppresses the other nonlinear effects. However, due to the abberation of the spherical mirror, the spectrogram is still distorted to some extent.

Fig. 4.10 is the spectrogram produced in $PbWO_4$, which has relatively low Raman gain compared to the diamond. We could see that the central frequency of the sidebands is shifted a lot as a result of the cross phase modulation induced by the

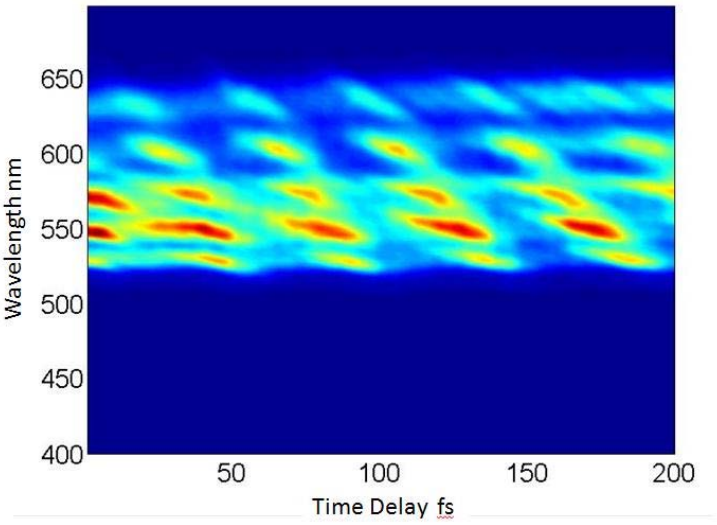

Figure 4.10: The spectrogram generated from $PbWO_4$ crystal. It is similar to the spectrogram generated in diamond. The x-axis is the time delay related to the other mirror which reflects the pump and Stokes beams.

intense pump beam. The oscillation period is changing during the scan, which can be measured by the distance between the adjacent intensity extrema. This results from several factors, such as the abberation of the concave spherical mirror, the chirp of the beam, the cross phase modulation, etc.

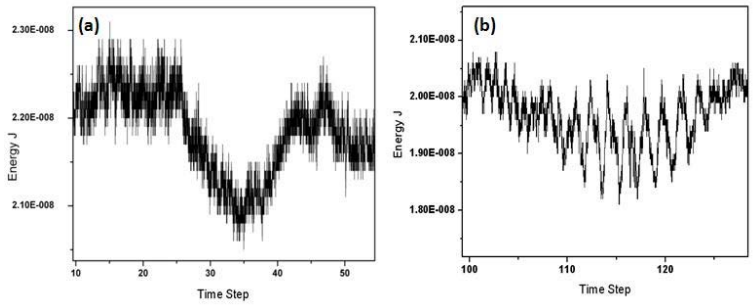

Figure 4.11: The power measurement of the sidebands generated from $PbWO_4$ crystal. (a) is the situation with only one sideband. (b) is the situation with two sidebands. The background is strong in these measurements.

This interferogram can be looked at as a result of the interaction between the pulse train and the coherent vibrational states driven by the pump and Stokes pulses. For a coherent Raman process, the generated multi-sidebands are coherent and they yield the pulse train when they are combined together. The duration of the pulse depends on the spectral bandwidth.

The Raman mode excited in this experiment is at 1332 cm^{-1}, which corresponds to the period of coherence of around 24 fs. But due to the dispersion and the other nonlinear effects, in the experiment, the frequency difference between the sidebands is decreased for the higher order anti-Stokes sidebands. Therefore, the period of the coherence in experiment is around 30 fs. The period of the intensity oscillation is nearly the same for the spectrogram generated from two sidebands (Fig. 4.9(a)). But for multi-sidebands, the beating period is different and it decreases for the higher order sidebands (Fig.4.9(b)). The pulse duration of a single pulse produced through the coherence Raman process is around 100 fs [87], which is much longer than the period of the coherence between the vibrational states. When the single pulse interacts with the coherent state, it only produces the Raman scattering (together with other nonlinearities). However, when two different sidebands are reflected back and combined on the crystal, the duration of a sub-pulse is smaller than the period of coherence. In this case, the nonlinear interaction would depend on the phases of the coherent states. If the pulse train interacts with the phased state ($\rho_{ab} > 0$), the lower frequency is advanced with regard to the higher frequency. When the pulse interacts with the antiphased state, the higher frquency is advanced over the lower frequency [19]. Therefore, if we move pulse train from the phased state to antiphased state (This is what happens when we scan one spherical mirror), an oscillation of intensity occurs in frequency domain [22]. In addition, we use power meter to measure the energy of the sidebands during the scan. Fig. 4.11 is the power measurement of

the single sideband when we scan the position of the mirror. Fig. 4.11(a) is the case when only one sideband is reflected back. Fig. 4.11(b) is the case when two adjacent sidebands are reflected back. With one sideband, we see a depletion of the energy of the sideband when the sideband overlaps with the pump and Stokes beams. With multi-sidebands reflecting, we see the oscillation on the energy when they are overlapped with pump and Stokes beams.

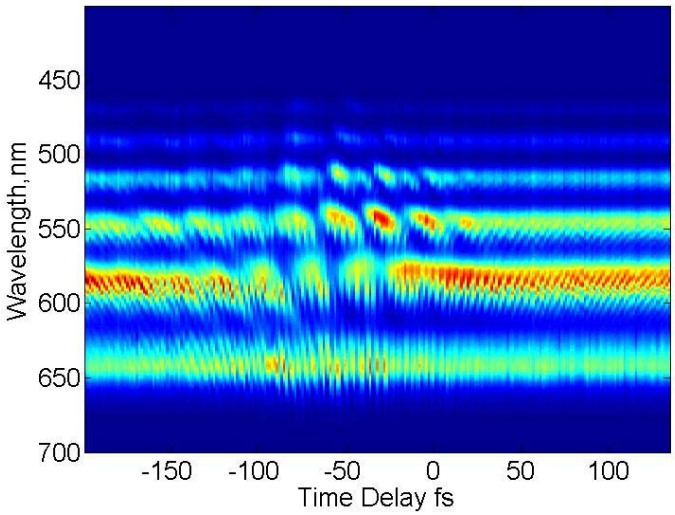

Figure 4.12: The spectrogram generated by two sets of beams in the diamond. The interference pattern on the spectrum implies that there are two groups of beams with the same frequency

Moreover, since the reflected pump and Stokes pulses are still sufficient strong, they are able to generate another set of sidebands, which have almost the same frequencies as the original sidebands. On a white screen, we see the interference pattern between the old beams and the new generated sidebands. In some situations, a fringe on the spectrum can be observed in spectrometer as there are double pulses with the same frequency (Fig. 4.12). Besides that, we also observe another two

intensity oscillations with different frequencies, one has very large frequency which appears before the pump and Stokes beams overlap with the high order anti-Stokes sidebands (Fig. 4.13(b)). The other has a relatively small frequency (Fig. 4.13(a)), which corresponds to hundred fs. This might be induced by the spherical mirror aberration.

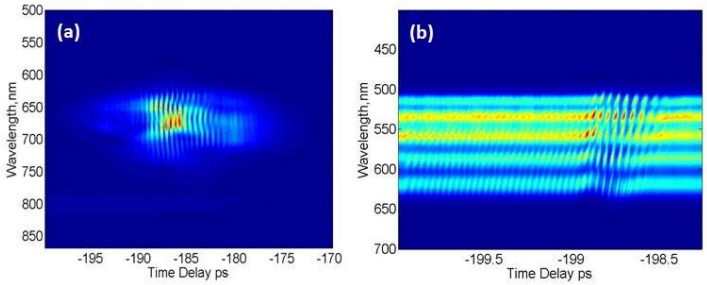

Figure 4.13: The other intensity oscillation observed in experiments. (a) has a period around hundreds femtoseconds. This may be induced by the imperfection of the spherical mirrors. (b) has a bigger frequency and occurs when the beams just begin to interact with each other.

In principle, it is possible to retrieve the spectral phase from the interferogram in a way similar to XFROG trace retrieval. However, it is a bit different from the XFROG [47]. In conventional FROG or XFROG, the gated signal is different from the source either in frequency or polarization. Hence, the signal could be completely separated from the source . The amplitude of the source is proportional to the amplitude of signal. However, in the Raman interferogram, the signal is mixed with the original beam and we are unable to separate them. This requires to include the depletion of the beams in the theoretical model of phase retrieval. Therefore, the typical FROG retrieval algorithm does not work directly for the Raman interferogram we produced. We need a different algorithm to retrieve the spectral phase.

The spectrogram represents the modulation induced by the molecular transition. If the spectrum of one single sideband is infinitely narrow, the analytical solution can be obtained theoretically [83]. Nevertheless, our experiments are done using femtosecond optical pulses, so that it is required to extend the work in Ref. [83] to the broadband situations.

We describe the theory of coherent Raman scattering in Section II[19, 83]. For a single frequency, the effective Hamiltonian has the following form as we showed in Section II [19]:

$$H_{eff} = -\frac{\hbar}{2}\begin{bmatrix} \sum_q a_q|E_q|^2 & \sum_q b_q E_q E_{q-1}^* \\ \sum_q b_{q+1}^* E_q E_{q+1}^* & \sum_q d_q|E_q|^2 - 2\Delta\omega \end{bmatrix} = -\frac{\hbar}{2}\begin{bmatrix} A & B \\ B^* & D - 2\Delta\omega \end{bmatrix}. \tag{4.1}$$

For the broadband spectrum, the equations need to be modified. We adopt the notation from Silbergerg et al [122] and write the nonlinear polarization as

$$P^3 = P^3_{NR}(\omega,\tau) + P^3_R(\omega,\tau) = \int_0^\infty (\chi^3_{NR} + \chi^3_R(\Omega))E_3(\omega-\Omega,\tau)S_{ps}(\Omega)d\Omega, \tag{4.2}$$

where

$$S_{ps}(\Omega) \equiv \int_0^\infty E_p(\omega'+\Omega)E_s^*(\omega')d\omega', \tag{4.3}$$

here S_{ps} represent the coherence build up by the pump and Stokes beams. We replace it with $\rho_{ab}(\Omega)$ for the higher order sideband generation. E_3 is the probe beam. In the cascaded Raman process, it is replaced by E_q.

We still take all sidebands far away from the resonance as described in 2.36 and assume $a_q = b_q = a_0$ and $b_0 = b_q$ and define propagation constant $\beta_q(\omega) = \eta\hbar\omega_q N a_0$ for different wavelength. Describing the interaction using a convolution of

the broadband spectrum, the propagation equations can be written as

$$\frac{\partial E_q(\omega,z)}{\partial z} = -j\frac{b_0}{a_0}\beta_q\left(\int \chi(\Omega)\rho_{ab}(\Omega)E_{q-1}(\Omega-\omega)d\Omega + \int \chi^*(\Omega)\rho^*_{ab}(\Omega)E_{q+1}(\Omega+\omega)d\Omega\right) \tag{4.4}$$

The quantity $\rho_{ab} = \frac{1}{2}sin(\theta)exp(j\varphi)$, where $B = |B|exp(j\varphi)$, $tan\theta = \frac{2|B|}{2\Delta\omega - D + A}$. The line profile is describe by $\chi = \frac{\alpha}{\Omega-(\omega_p-\omega s)-i\gamma}$. α is a constant related to the spontaneous Raman cross-section. ω_s and ω_p are the angular frequencies of the pump and Stokes. γ is the half-width of Raman line. We set the boundary condition according to our experiment. For example, in our experiment of Fig. 4.7 the boundary condition is as follows : besides E_0,E_{-1}, E_3, E_4, E_5 and E_6, all the other sidebands give zero contribution at $z = 0$. $E_q = Eamp_q * exp(j(\varphi_q))$ and $Iamp_q = |Eamp_q|^2$. At $z = 0$, E_0, E_{-1}, E_3, E_4, E_5 and E_6 can be obtained from the measurement of spectrometer. φ_q is the parameters retrieved by our simulation. These partial differential equations can be solved numerically using Runga-Kutta method.

The integral is approximately calculated sampling with small step in the frequency domain. As a prerequisite, we need to test that the step we choose is small enough to give a converge result. Then in order to make the calculation much efficient, we make some further assumptions. From results of simulations, we realized that the pump and Stokes beams would not affect the period of the intensity oscillation. The role of strong pump and Stokes is to build up the coherence between the vibrational states. Therefore, we take the pump and Stokes out of the boundary conditions and assume the phase and the strength of coherent states are constant during the interaction. Second, we assume the interaction length to be around 200 hundreds μm, which is evaluated by the beam waist and Rayleigh length. The beam intensities and coherence are uniform in this length and the divergence will be neglected. Moreover, the solutions of equations have properties of Bessel function, which are similar to the

result of Ref. [19].

In order to compare with the experimental result effectively, we need to further process the experimental data recorded by spectrometer. The experimental results are smoothed to get rid of the noise. Since the pixels of spectrometer are not uniformly distributed in frequency, we use the numerical intrepolation to reconstruct the field in frequency domain. Moreover, for the sidebands in coherent Raman scattering, there are two kinds of phases: one is "local", which appears on each individual sideband, the other is "global", which is related with the phase between different sidebands, as we discussed in the last subsection. In the first order approximation, we want to retrieve the "global" phase between the sidebands. In addition, tn the synthesis of the ultrafast waveform, the relative phases are decisive, so that we have no need to get the absolute phase of the beams. Here, we want to reminder the reader about the relationship between the spectral phases and the waveform. For one beam with single frequency, the phase is arbitrary, which depends on the initial time. If there were two beams with different frequencies, the phase of the second beam would only affect the carrier envelope phase instead the envelope. When there are three beams, the phase of the third beam begin to affect the waveform. Therefore, for the waveform synthesis, the relative phase become important only when there are more than two different beams. Our theoretical simulation starts from the same initial condition of time. The parameters we control are the phases of the spectral component, the time delay between the sidebands, the propagation coefficient and the interaction coefficient. The results for two sidebands of AS3 and AS4 are shown in Fig. 4.14. Fig. 4.14(a) is the theoretical result and Fig. 4.14(b) is the experimental result. (c) and (d) are the cross section at wavelength 597 nm on AS3 and 557 nm on AS4 respectively. It shows that the intensity oscillations from the experiment have the same phase and period as the theoretical results, even though the amplitudes are

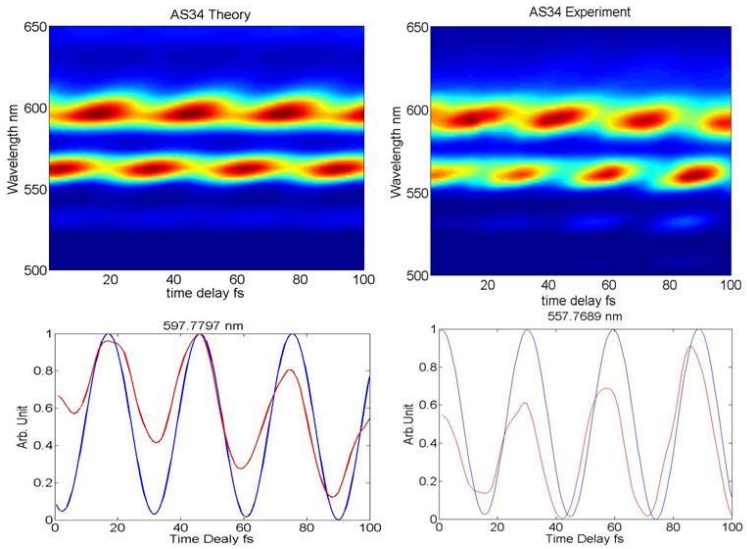

Figure 4.14: The theoretical simulation and the experiment of the interferogram of AS 3 and AS 4. The top left is the result of theory and the top right is the result of experiment. The bottom left is the comparison at the wavelength 597.7 nm and 557.7 nm. The red line is the result of experiment and the blue line is the result of the theoretical simulation

not 100% in agreement with each other due to the other parasitic nonlinear effect.

Fig. 4.15 is the result for AS3-AS7. It also shows an agreement of the phases and periods of the intensity oscillation betwenn the theory and experiment, which implies that our theoretical simulation has the right "global" phases. But the "local" phase is still different due to the dispersion resulted from the aberration of spherical mirror and the parasitic nonlinear effect. The "local" phase is difficult to retrieve in our current setup. In principle, we can use the simulation to predict the structure of the nondistorted interferogram of the sidebands, which can be used as a criterion for our phase correction experiment. With the global phases we retrieved from the numerical calculation, we calculate the ultrafast waveform and the electric field of the ultrafast waveform synthesized using AS3-AS7 (Fig. 4.15 (c) and (d)). Fig. 4.15.

The phase retrieval based on Raman interaction is different from the phase re-

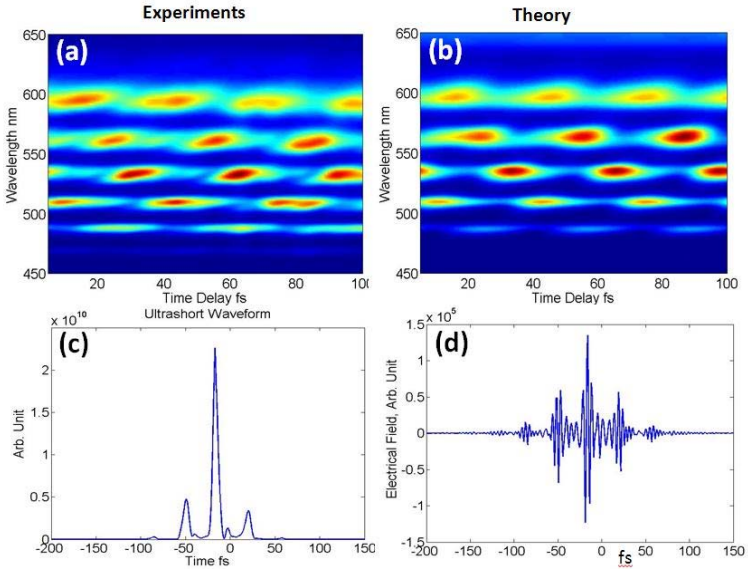

Figure 4.15: The theoretical simulation and the experimental interferogram of AS3-AS7. (a) is the experimental interferogram and (b)is theoretical interferogram. They are in agreement with each other for the intensity oscillation. (c) is the ultrafast waveform retrieved from the experimental interferogram. (d) is the electric field of the ultrafast waveform retrieved from the experimental interferogram.

trieval based on parametric nonlinear process such as SHG or SFG. Using of SHG or SFG allows retrieval of the spectral phase especially for near IR fields successfully [47]. However, if SHG or SFG approaches the UV range, it would give rise to some difficulty situation because of the large loss of UV in optics. The scheme to generate the interferogram using Raman scattering could avoid this problem. However, the Raman process coexists with some other nonlinear process, therefore, the accuracy would be lower.

4.3 Ultrafast Waveform Synthesis Using Deformable Mirror (DM)

The setup described in the first subsection is capable of producing non-sinusoid waveform in visible and UV range with coherent Raman sidebands. But the energy of the waveform are limited by the damage threshold of the crystal TeO_2 inside Dazzler.

Meanwhile, due to the relative small bandwidth over which the integrated Dazzler can act upon, the pulse duration generated with one commercial Dazzler is around few femtoseconds. Therefore, if we want to synthesize a sub-cycle optical pulse, we need to combine several different Dazzler to provide the required bandwidth, which will make our setup more complicated.

In Section II, we describe the experiment to measure the spectral phase in reflection scheme based on Raman interaction. The advantage of this scheme for the pulse synthesis is that the energy of the ultrafast waveform would be sufficiently high due to the low loss of setup. Also it would easily allow ultrafast waveform synthesis with a more broaband spectrum. At the focal point of the spherical mirror, the coherent sidebands are overlapped temporally and spatially so that the ultrafast waveform would be obtained in a short region. Even though these ultrafast waveforms would not be maintained during the propagation, it is still useful in scientific research, where the ultrafast waveform is required only in a short distance such as the study of significant new nonlinear phenomena and the dynamics in sub-femtosecond scale [2].

From the result of simulation for the reflection scheme, we know that the ultrafast waveform formed at the focal point is not Fourier-transform limited. Hence, we need to modify the spectral phases of the sidebands for ultrafast waveform synthesis in the reflection scheme. We propose to use deformable mirrors (DM) to adjust the spectral phases. The deformation of the surface is induced by applying high voltage at the accurator of the DM, which corresponds to a 2 mm $\times$ 2 mm area of the mirror surface. The surface can be modified by tens of nm, which makes it a phase sensitive device. Hence, if the beam diameter is below 2 mm, the DM would be able to adjust the "global" phase of the beam. Using sidebands generated from $PbWO_4$, our experiment demonstrates that the ultrafast waveform could be synthesized using

the coherent Raman sidebands with the assistance of DM.

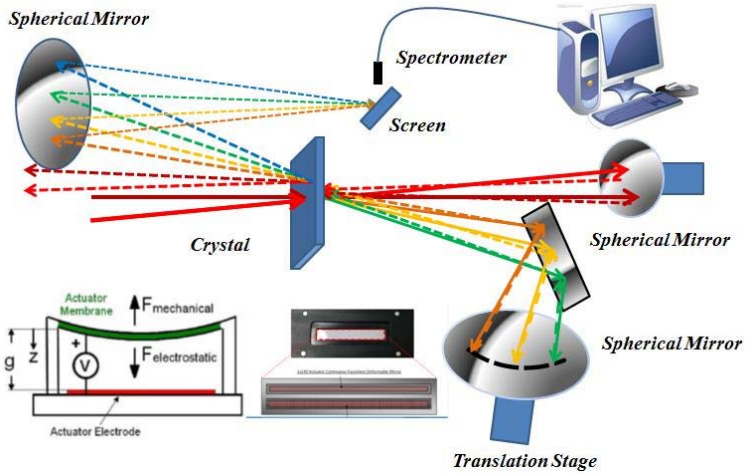

Figure 4.16: This is setup to generate the spectrogram with deformable mirror. DM is the phase sensitive device. The insets are the sketch of the DM. For each of the accurator, there would be a electrode, which could be applied high voltage. The active area of one pixel of DM is around 2 mm $\times$ 2 mm. This could change the surface of the mirror, which is a special membrane material. The surface of mirror could be poked by at most around 1.6 μm. The smallest step is also around tens of nanometer.

In the experimental setup, we insert the deformable mirror where the beams are still separately as shown in Fig. 4.16 so that we could adjust the spectral phase for each sideband independently. Raman sidebands are generated on $PbWO_4$ in the experiment. On the second mirror, three Raman sidebands, AS7, AS8, and AS9 are reflected.

In a spectrogram with two sidebands, the intensity oscillation is directly connected with the phase difference between two sidebands. If the beams are single frequency, the "local extremum" intensity is where the phase difference is close to 0. The nearly unchanged intensity is where the phase difference is close to π. So

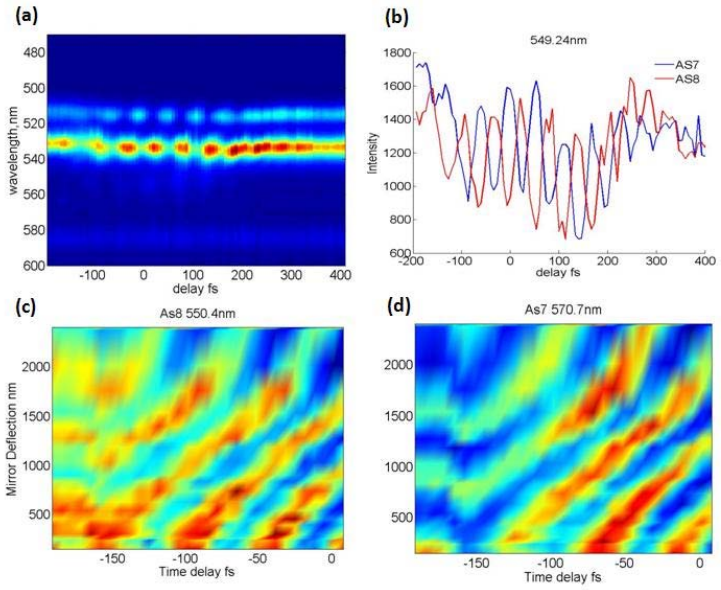

Figure 4.17: The synthesis of spectral phases with DM. (a) is the spectrogram of AS8 and AS9. (b) is the cross section at 550 nm from two spectrograms with different AS8 phase. It shows that by adjusting the spectral phase, we could make the intensity oscillation out of phase. (c) and (d) are how the intensity oscillations change when we adjust the phase of AS8 continuously. The y-axis is the displacement of the surface of DM.

by looking at the intensity oscillation, it is easy to observe the adjustment of the spectral phase.

Fig. 4.17 shows how DM modifies the spectral phases. We show a result where the intensity oscillation at certain wavelength 550 nm of AS8 is shifted by π (Fig. 4.17(b)). This is realized by using DM to adjust the intensity oscillation related to the result with no phase displacement. Fig. 4.17 (c) and (d) are how the intensity oscillation change at 550 nm and 570 nm as we adjust the spectral phases of AS8 continuously. Fig. 4.18 are the spectrogram of the ultrafast waveform synthesized using coherent Raman sidebands AS7, AS8 and AS9 with different spectral phase of AS8. Fig. 4.18(a)((b)) is the spectrogram and Fig. 4.18(c) ((d)) is the corresponding pulse in time domain retrieved from the theoretical simulation. The result demonstrates

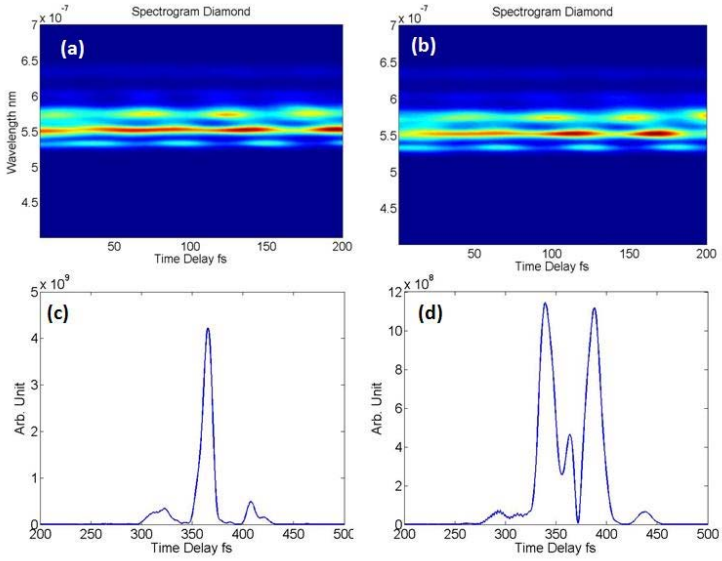

Figure 4.18: The synthesis of ultrafast waveform with DM. (a) and (b) are the spectrogram generated with AS7,AS8, As9, pump and Stokes beams. The difference between (a) and (b) is that in (b), we applied a additional π phase for AS8. (c) is the pulse we retrieved from the experiment result in (a) and (d) is the pulse we retrieved from the experiment result in (b)

the ability of our scheme for ultrafast waveform synthesis. I need to mention that in our demonstrative experiment, we do not manipulate the amplitudes of sidebands. Also limited by our device, we could not correct the phase distortion on each individual sidebands. In principle, the best way to synthesize the ultrafast waveform is to adjust the spectral phase for each sidebands separately. The micro-mirror arrays might be an ideal choice.

5. ULTRAFAST OPTICS APPLICATIONS

The field of ultrfast optics is highly cross-disciplinary, including physics, chemistry, biology, material science, medical science, and so on [1]. The coherency, high time resolution, and ability to reach extremely high powers are all properties which allow for the specialized applications. In this section, I will present two experimental demonstrations of the application of femtosecond laser pulses. The first demonstration is using femtosecond laser filamentation to get sub-diffraction imaging in remote sensing. The second experiment demonstrates an optical-control of TEA nitrogen laser using femtosecond laser pulses. In the third subsection, I will present a theoretical simulation for the generation of UV ultrafast pulses using near IR femtosecond pulses in HC-PCF. This could be a source for the ultrafast pulse in the UV range.

5.1 Sub-diffraction Imaging Using Laser Filamentation in Remote Sensing [1]

Ever since the invention of the telescope, many techniques for seeing at a distance have been developed, even up to the present. Normally these are limited by diffraction, which is a consequence of the wave properties of light that causes it to spread as it propagates. One way to overcome this limit is to illuminate the target with a focused beam from a source, like a laser, that is in the proximity of the target. Essentially this is analogous to moving the object up close so we can examine it in detail. However the deployment of a distant laser source is usually not practical and so an alternative is needed. Here we assert that laser triggered filaments can provide the high-resolution illumination spots needed to achieve practical long-range

[1]*Part of this subsection is reprinted with permission from "Remote sub-diffraction imaging with femtosecond laser filaments." by K. Wang, B.D. Strycker, D.V. Voronine, P.K. Jha, M.O. Scully, R.E. Meyers, P. Hemmer, A.V. Sokolov, OPTICS LETTERS 37(8) 1343-1345(2012), Copyright 2012 by Optical Society of America

sub-diffraction imaging. It has been known for a while that intense laser pulses can be used to create filaments or sparks, like man-made lightning, in the air [9, 50]. These have many important applications, such as remotely guiding real lightning bolts along safe discharge paths [123]. In particular, the use of femtosecond pulses with negative prechirping has demonstrated the ability to create these filaments at a long distance from the source [51–53]. This technique has already been considered for long range sensing, for example ionization of particular chemicals in the air for remote threat detection [9, 50], or possibly the production of backward propagating lasers for long-range high-resolution spectroscopy [57, 124]. Here we examine the use of these long distance filaments for high resolution imaging of remote targets. To see the power of laser filament imaging, consider that the size of the laser filaments is determined by the properties of the material through which the light propagates. Filamentation occurs when an intense femtosecond laser pulse is self-focused to create a high enough intensity to ionize the material. Once this threshold is reached the laser beam is self-guided and its size is determined by the interplay between Kerr self-focusing and defocusing from low density plasma. Hence the size of the filaments is not limited by the aperture of an optical system [125] which would ordinarily determine the diffraction limited laser spot size. The intensity and diameter of a self-guided filament remain constant as it propagates. This means the depth of field may be several orders of magnitude greater than that of a conventional imaging system, as it is determined by the length of the filament. Laser scanning using focused light thresholding, which has also been shown to achieve sub-Rayleigh resolution imaging [126], verifies the importance of the size of the illumination beam. Therefore imaging with laser filaments that are narrower than normal laser illumination beams would give unique advantages toward achieving sub-diffraction illumination of remote objects and scenes. Although laser filament imaging is restricted to appli-

cations involving scanning laser illumination, such systems are ubiquitous; from bar code reading to environmental sensing to military target identification. For example, environmental sensing uses laser radar (LIDAR) to measure atmospheric pollution thousands of meters above ground [127]. For long range imaging and target identification, laser illumination has several advantages over ambient light. For example: 1) Laser illuminated objects do not suffer from confusing shadows or back lighting. 2) Laser illumination is capable of delivering higher power to particular regions of interest in a scene to enhance the local image signal to noise ratio. 3) Short pulsed lasers enable high resolution in the propagation direction, outperforming stereoscopic techniques for long standoff distances. In remote imaging and sensing, beating the diffraction limit by using nonlinearities of the intervening medium between object and image is an approach that has been largely neglected. Yet nonlinearities already play an important role in many existing sub-diffraction and sub-wavelength imaging schemes, for example many sub-diffraction microscopy [128–131] and super-resolution lithography methods [132–136] exploit nonlinearities in the target (i.e., the object being imaged or photoresist). Quantum nonlinearities of light and the photo-detection process have also been exploited for super-resolution [137]. This has become an important approach since it was shown that quantum features of light could be simulated through frequency selective measurement [138]. Super-resolution can also be accomplished using non-classical states of thermal light, as in two-photon interference ghost imaging [139], even through turbulence [140, 141]. In this case, less focused sources of light actually create higher resolution images, especially when lensless ghost imaging is used, provided enough light passes through any turbulence or obscurants to illuminate the target with sufficient energy [139]. The use of filaments is particularly attractive for exploring super-resolution with more directed energy.

5.1.1 Experiments

In a proof-of-principle experiment, we demonstrate remote imaging with resolution at least an order of magnitude greater than that allowed by diffraction, by using femtosecond laser filaments in water. Our experimental setup is shown in Fig. 5.1. We use a Ti:Sapphire regenerative amplifier (Legend Elite Coherent: 1 kHz rep. rate, 4mJ/pulse) seeded by a Coherent Micra-5 Ti:Sapphire Oscillator (80 MHz rep. rate, 470 mW). The amplifier spectrum is centered at 800 nm, and the pulse is 34 fs full width half maximum (FWHM). The power is attenuated by neutral density filters, while the iris diameter is D=2 mm. The FWHM of the beam at the target is 1.647 mm. The beam power after the iris is 203 mW, which is sufficient to generate a single filament in water. In order to establish a stable single filament, we adjust the chirp of the pulse by varying the compressor setting of the amplifier; the beam power remains constant. The target is placed in a water tank L=5 m distant from the iris. Back-scattered light from the sample is collected by a photomultiplier tube (PMT). A high-pass optical filter is used to block the 800 nm back-scattered light from the energy reservoir of the filament while allowing the white light generated in the filament core to be detected. The diameter of the iris D and the distance L determine the diffraction limit to be $\delta = 1.22\lambda L/D = 2.44\ mm$. The diameter of the filament is about 40 μm. The pixel size of the image is determined by the scan step.

Our first target consists of two wires which are 150 μm in diameter and separated by about 400 μm. As shown in Fig. 5.2(a), the two wires are clearly resolved with the formation of a stable single filament; resolution of the wires disappears when the image is constructed without the filament (Fig. 5.2(b)). The resolution is 20 μm x 50 μm, 20 μm in the x direction and 50 μm in the y direction. The images have been digitally processed with interpolation. Figs. 5.2(c) and 5.2(d) show the cross-

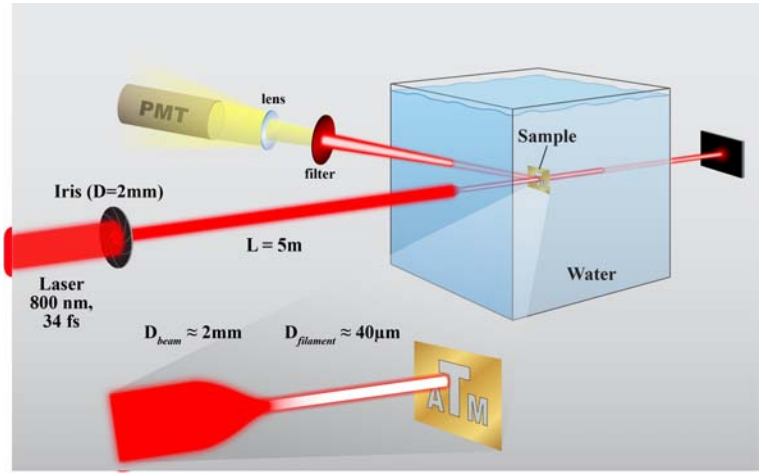

Figure 5.1: The experimental setup. The iris diameter is D=2 mm; it is L=5 m away from the target. The diffraction limit is $\delta = 1.22\lambda L/D = 2.44\ mm$. The diameter of the filament is about 40 μm, which is 60 times smaller than the diffraction limit δ. The target (ATM logo) is inside a water tank. The photomultiplier tube (PMT) collects the back-scattered light in order to reconstruct the image. A high-pass optical filter is used to block the scattered 800 nm light from the energy reservoir of the filament.

sections of the 2D scans in Figs. 5.2(a) and 5.2(b), respectively. The cross-sections coincide well with the theoretical convolutions (red curves).

Our second target is the Texas $A\&M$ University logo (ATM). The stroke width of each letter in the logo is about 300 μm, less than the diffraction limit of the system (2.44 mm). The letters are sculpted onto a transparency film (Fig. 5.3(d)). Fig. 5.3(a) is the retrieved image of the logo using a stable single filament, while Fig. 5.3(b) shows the image obtained without the use of filaments. The resolution of these images is 50 μ m $\times$ 50 μm, and they have been digitally processed with interpolation, as well. Our results clearly show that the sub-diffraction logo pattern can be resolved with a single filament. Fig. 5.3(c) digitally enhances the contrast of Fig. 5.3(a).

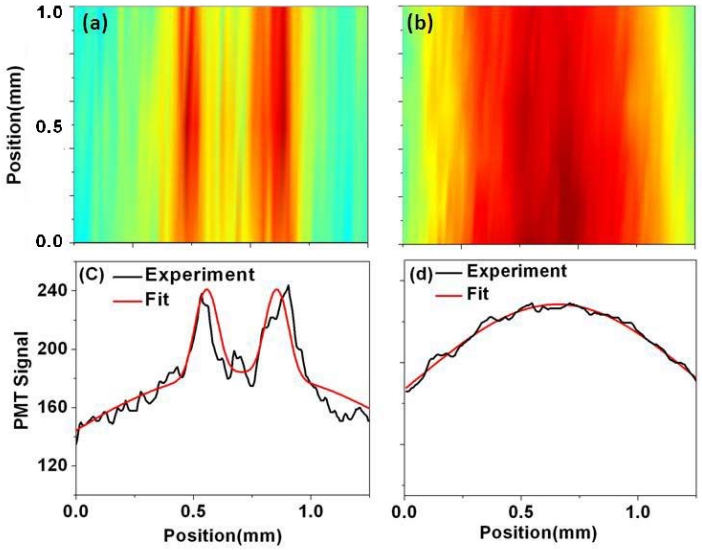

Figure 5.2: The remotely retrieved images of two wires. The wires are 150 μm in diameter and are separated by about 400 μm. (a) and (b) are the reconstructed images with and without a stable single filament, respectively. (c) and (d) are the cross-sections of images (a) and (b), respectively. The black curves are the experimental data and the red curves are the theoretical fits.

5.1.2 Prospect

The relatively small distances (and moderate laser powers) at which filament formation occurs in water render it useful for controlled studies of filament propagation in the laboratory. For long range imaging in the atmosphere the performance may be projected from our data with appropriate scaling [55]. The total number of molecules that a beam encounters and hence the total linear dispersion per unit length is proportional to the molecular density, which is 3 orders of magnitude greater for liquids than for gases under similar conditions. Therefore, each 1 cm of propagation in water, in terms of dispersion, will roughly correspond to 10 m in air. Nonlinear refraction will also scale with the molecular density, and in addi-

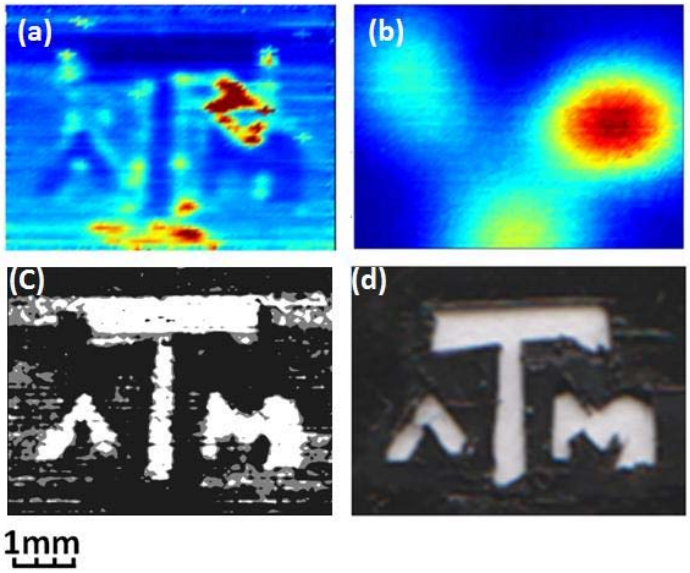

Figure 5.3: The remotely retrieved images of the TAMU logo (ATM) with (a) and without (b) a stable filament. The strokes of the letters are about 300 μm thick, smaller than the diffraction limit of our optical setup. With the filament, the ATM logo can be imaged clearly, while without a filament, the letters cannot be resolved. (c) The digitally processed image in (a). (d) A micro-photograph of the logo sculpted onto the transparency.

tion with laser power, so that more powerful laser sources will have to be used in atmospheric experiments. Based on the power of available lasers we envision sub-diffraction imaging in air performed kilometers away from the target [142]. For such long range applications, control of filament formation and propagation is paramount. In particular, turbulence is a major consideration for long range imaging, and indeed advanced techniques such as variable focusing [143, 144], and adaptive optics methods [145] will likely be needed to stabilize the turbulence-dependent spatial positions of the filaments. Here we note that filaments are robust and can maintain shape while propagating through rough media, turbulence, and aerosol perturbations which tend to spread conventional beams [126, 146]. Significantly, even if it

is not possible to adequately stabilize the filament positions, high resolution images can still be constructed using random filament positions by precisely determining the location of each filament flash in the image plane, for example computing the centroids in a manner analogous to the popular stochastic sub-wavelength imaging technique [128–130]. Filament Bessel beams are also feasible [147] and are especially interesting since non-diffracting Bessel beams already achieve sub-Rayleigh-limited illumination [148–150]. Therefore using Bessel beams to generate filaments could have multiplicative benefits, for example Bessel beams may allow filamentation at much longer distances than Gaussian beams. Bessel beams also have a self-mending property such that, when disturbed by particulates, the beams reform into a similar shape, although with a corresponding loss of scattered energy. Laser filament imaging could be used with compressive sensing [148, 151–153] to image a remote object with substantially less data points measured than would be needed by direct scanning. Compressive sensing recognizes that imaged objects have continuity and can be expressed in fewer degrees of freedom than the number of pixels in the image. Finally, especially desirable applications of filament imaging include sensing in atmosphere through curved spatial channels (i.e., seeing around the corner) which would be possible through use of ultra-intense filamenting Airy beams [154]. Laser filamentation also has prospects for upper atmosphere imaging, as it is independent of atmospheric pressure [155]. Filaments even have potential to advance the field of underwater sensing and imaging; they might be used in underwater scanning of oil and gas plumes [156] as well as in extended range underwater imaging via structured illumination [157]. Filaments may also be utilized to generate remote acoustic sources for acoustic imaging [158]. In particular, our demonstration experiment which images sub-diffraction limited features of an object in a distant water environment is directly applicable to high altitude airborne imaging of small objects beneath the

ocean surface. Hence femtosecond filaments may find many uses for sensing and imaging in any environment.

5.2 Optical Control of a TEA Laser Using Ultrafast Laser Pulse

The realization of all-optical control devices where the "gate" photons could switch a "source" light beam has been a long-standing goal in optics, especially in optical communication and quantum information. All-optical control has been demonstrated from a level of few hundred photons to a few photons by means of electromagnetic induced transparency (EIT) in atomic system [159]. All-optical switches and modulators has also been realized in III-V compound semiconductors [160].

In this subsection, we report a demonstration of all-optical control of a TEA nitrogen laser by triggered a TEA nitrogen laser with a femtosecond laser pulse. This may see applications in a remote sensing scenario. With a second TEA laser, we also setup a model to demonstrate the swept gain scheme for remote sensing [57].

The TEA nitrogen laser is a gas laser operating in the ultraviolet range using molecular nitrogen as its gain medium energized by a high voltage electrical discharge pressure [56]. Our experiment is done with a home-made TEA nitrogen laser. The schematics of home-made TEA nitrogen laser is shown in Fig. 5.4(a). The TEA laser in our lab is shown in Fig. 5.4 (c). Two extreme flat aluminum plates are put parallel to each other, with sharp edges to form a 2 mm $\times$ 300 mm pencil-like gap. These two plates are also connected by a 2 $k\Omega$ resistor. One of the plate is connected with high voltage power supply. The other is connected with a electrode. There is another electrode grounded with a large metal plate. The distance between two electrodes are around 8 mm. Between the grounded plate and the two parallel plates, we put several sheets of dielectric papers to form a capacitor. The high voltage will induce an air breakdown between the two electrodes. This leads to a transverse uniform

discharge in the pencil-like gap. During the fast high voltage discharge in air, the nitrogen molecular is populated to the upper laser level, an excited state with a 40 ns lifetime (The energy diagram for molecular nitrogen is shown in Fig. 5.4(b)). When it drops to the lower level, it emits at 337.1 nm. The discharge occurring inside the pencil-like gap will invert the population of nitrogen molecular and build up the gain for lasing. Therefore, the fluorescence can be amplified to be a laser pulse. The lasing generally comes out both in forward and backward directions along the gap. The lower laser level has a 10 μs decay time, much longer than the upper level, and then drops to a metastable state with a much longer lifetime. This makes it a pulsed laser instead of a continuous wave laser. Fig. 5.4 (d) is the beam profile of the nitrogen laser recorded by a camera. Besides, TEA laser has a very good beam quality [56].

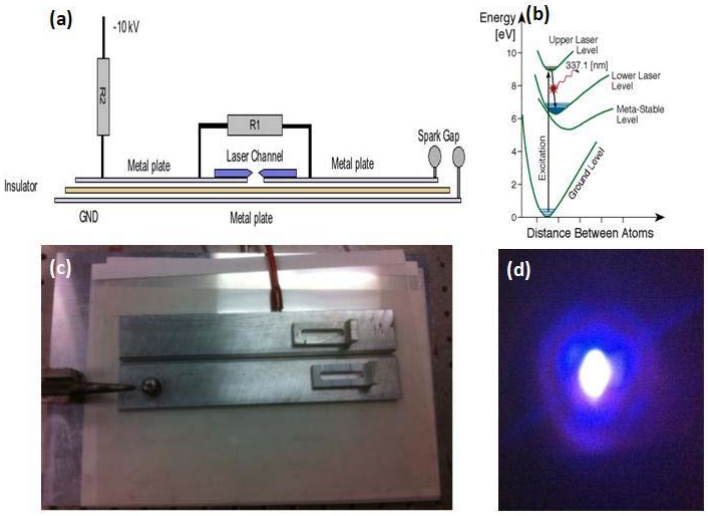

Figure 5.4: (a) The design of home-built TEA nitrogen laser. ($http://new-electronics.gr/n2/tea_air_laser2.html$). (b) The energy diagram for nitrogen laser. (c) The photo of the home-made TEA nitrogen laser in our lab. (d) The photo of the beam profile of nitrogen laser. The lasing is at 337 nm in the UV range. The photo shows the fluorescence of lasing on a white paper.

In order to control the TEA nitrogen lasing, we try to synchronize the air breakdown with a femtosecond laser pulse. In the first step, we stop the spontaneous air breakdown between electrodes by decreasing the voltage (In our experiment (Fig. 5.5(a)), the air breakdown will occur when the applied voltage is above 5 kV). Then we focus the femtosecond laser pulse inside the spark gap, which will produce a conventional plasma. This plasma helps to trigger the air breakdown in the lower electric potential. We observe that the air breakdown has been synchronized very well with the plasma induced by the femtosecond laser pulse. As long as the air breakdown takes place, there would be a uniform discharging inside the pencil-like gap, which builds up the population inversion for the nitrogen molecular and leads to a nitrogen lasing from the gap.

We record the nitrogen lasing together with the air breakdown using an oscilloscope. The histograms we record show that there is a time jitter between the air breakdown and the lasing, which is $\sim \mu s$. Fig. 5.5 (a) is the experimental setup. Fig. 5.5 (b) is the nitrogen lasing and the discharge signal (spark) between two electrodes recorded in time domain. Fig. 5.5 (c) and (d) are the histograms of the lasing corresponding to the spark between the two electrodes in time domain. The oscilloscope is triggered by the nitrogen lasing and histograms are constructed by air breakdown signals (spark). Fig. 5.5 (c) is the histogram when a femtosecond laser pulse is focused between the electrodes. The pulse produces a conventional plasma to induce the air breakdown between electrodes. It shows a μs time jitter between the triggered air breakdown and N_2 lasing. Fig. 5.5 (d) is the histogram of spontaneous air breakdown when there are no femtosecond laser pulses to produce the plasma between electrodes. It shows a similar profile as Fig. 5.5 (c) and there is a μs time jitter between the lasing and the spark as well. In Fig. 5.5 (c), there are also some traces at 200 μs and 250 μs. So far, we do not have a clear understanding

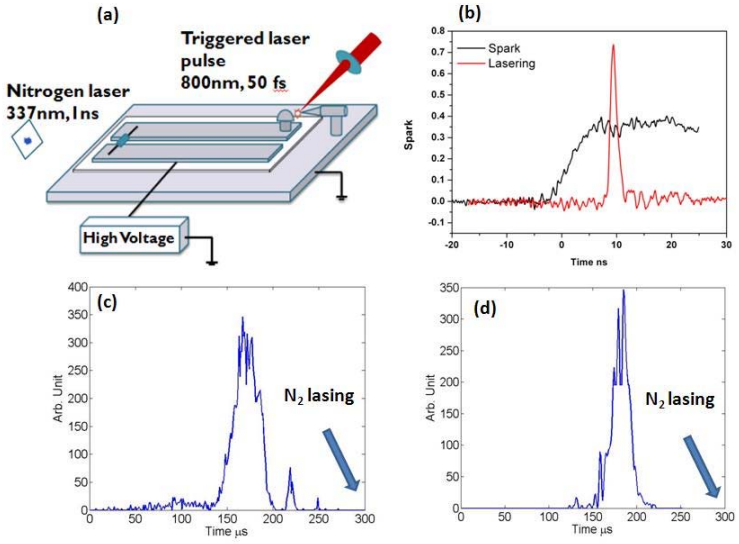

Figure 5.5: (a) The setup of the triggered TEA nitrogen laser. The distance between two electrodes in the spark gap is 6 mm. A femtosecond laser is focused between two electrodes. (b) The signal of the nitrogen lasing and the spark between two electrodes recorded in time domain. (c) and (d) are the histograms of spark corresponding to the N_2 lasing. N_2 lasing is set as the trigger for the histogram. (c) The histogram when a femtosecond laser pulse triggers the spark. (d) The histogram when no femtosecond laser pulses trigger the spark and a higher voltage between two electrodes is applied to induce the spontaneous air breakdown between the electrodes.

for them. These histogram envelopes could be fitting into the gaussian function very well, which implies that the different time jitter corresponding to the different spatial tracks of the air breakdown between two electrodes. This microsecond time jitter has limited the application prospect of the current setup. A proposal to suppress the time jitter is to replace the electrodes with hydrogen thyratron to switch the air discharge inside the pencil-like gap.

By configuring two TEA nitrogen laser setups as shown in Fig. 5.6, we could use this as a model for swept gain scheme in remote sensing. P. Hemmer, *et al.* [57] proposed an conceptual approach on the basis of the backward-directed lasing and stand-off spectroscopy. It relies on the remote generation of a weakly ionized plasma chan-

nel through the way like filamentation of an ultra-intense femtosecond laser pulse. Depending on the spectral and temporal content of the driving pulses, a transient population inversion is established in either nitrogen- or oxygen-ionized molecules, thus enabling a transient gain for an optical field propagating toward the observer. The proposed technique can be enhanced by combining it with the gain-swept excitation approach as well as with beam shaping and adaptive optics techniques. This technique results in the generation of a strong, coherent, counter-propagating optical probe pulse. Such a probe, combined with a wavelength-tunable laser signal(s) propagating in the forward direction, provides a tool for various remote-sensing applications.

We use the home-made TEA nitrogen laser to demonstrate the gain-swept excitation of nitrogen laser in the lab. Two TEA lasers are combined as Fig. 5.6. The nitrogen gain is built by the discharge in air inside the TEA laser instead of laser filamentation . In this model, the lasing from one TEA laser will pass through the gain region of another TEA laser. The pulse would arrive at a proper time when the gain is build up. Hence the pulse in one direction would be amplified by the transient gain. Combining two TEA nitrogen lasers could be looked as the "Oscillator-Amplifier" laser system. The lasing power of the "Oscillator" itself measured to be 90 μW and the "Amplifier" itself measured to be 30 μW. In the case when they are combined as the swept gain model, the lasing is measured to be near 200 μW from the "Amplifier". This clearly shows that with a proper timing, the laser pulse could be amplified by the gain-swept excitation approach based on nitrogen-ionized molecular in the atmosphere, which provides a strong probe field towards observers.

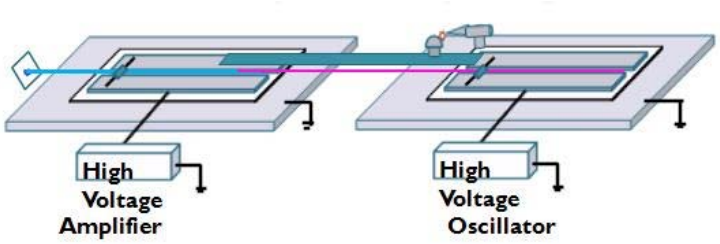

Figure 5.6: The scheme for the swept gain model for remote sensing. The two TEA nitrogen laser would be triggered simultaneously. One of them could be used as the "Oscillator" and the other one could be used as an "Amplifier".

5.3 Dispersive Wave in Photonic Crystal Fiber

The generation of ultrashort pulses in optical fibers has been well-studied. Using the nonlinear polarization rotation (NPR) technique, the 77 fs ultrashort pulse was first achieved in a short unidirectional ring laser in 1993 [161]. Since then, the NPR technique become the main method to generate ultrashort pulses in fiber lasers and attracted much attentions [162]. However, most of these work are done in the near infrared region. In the UV range, there are not many source available to generate the ultrashort pulse. As an example, researchers could get ultrashort UV pulses by using hollow fiber to compress the pulses duration in that spectral region [163].

In the femtosecond regime, when pumping the optical fiber with a femtosecond pulse in the anomalous dispersion spectral range, the supercontinuum generation process is mainly dominated by solitonic dynamics [164]. In addition to the formation of a high-order soliton in the anomalous dispersion spectral range and its subsequent fission into lower-order solitons, each soliton component is sometimes accompanied by the emission of resonant dispersive waves (RDW) in a spectral range where the dispersion can be normal [58, 100]. The latter phenomenon entails the emission of narrow band quasi-linear pulses at specific frequencies and results from a special kind

of phase matching between the optical soliton propagation constant and those of the emitted radiation components [68, 165].

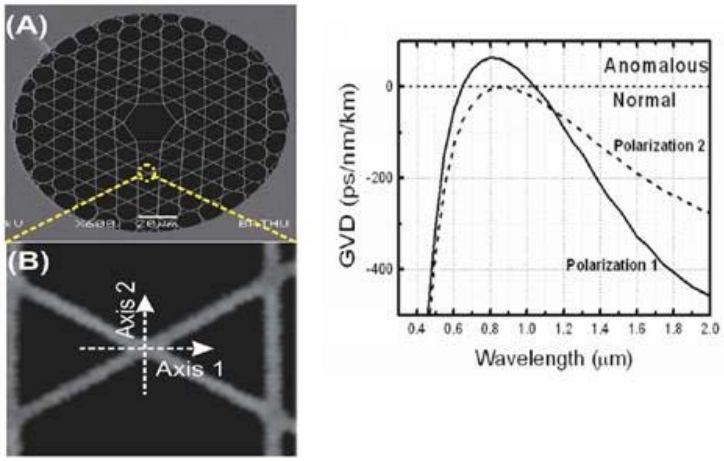

Figure 5.7: The dispersion of Kagome-lattice HC-PCF fiber and the STM photo of the structure. The Kagome-lattice HC-PCF has a pitch of 12.5 μm and a strut-thickness of 550 nm.

RDW has been experimentally identified in the spectra generated within solid-core PCFs [100, 164] and hollow Kagome fiber [59]. In the latter work, the two dispersive waves were proved to be femtosecond pulses, with pulse durations of about 118 fs and 125 fs at the blue and the red sides, respectively, of the main soliton (for Gaussian pulses). Considering the RDW at the blue side, it could be a good resource to produce short pulses in the UV region.

We do a numerical calculation to explore whether we could make RDW pulses shorter by inputting either a chirped pulse or several pulses centered at different wavelength. The NSE equation , which is used to describe the wave propagation, is

$$i\psi_z + D(i\partial t)\psi + \gamma N(|\psi|^2)\psi = 0, \tag{5.1}$$

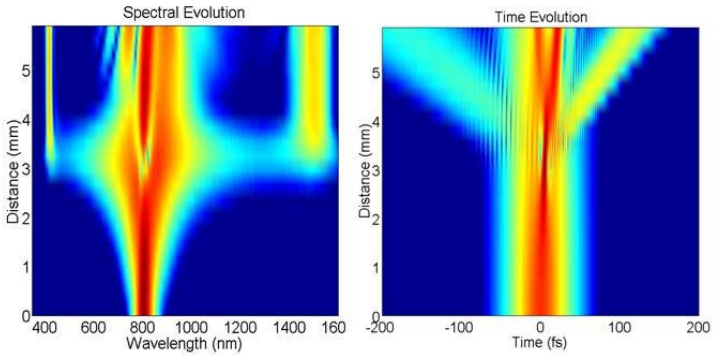

Figure 5.8: Theoretical simulation of propagation of a FTL pulse with central wavelength 806 nm. The propagation distance is 6mm. The left is the change of the spectrum as the pulse propagated inside the fiber. The right is the change of the pulse in time during the propagation.

where $\psi(z,t)$ is the complex amplitude of the pulsed electric field envelope, $\gamma = \frac{n_2\omega_0}{cA_{eff}(\lambda)}$, and n_2 is the nonlinear index (the Kerr coefficient). Here,

$$\widehat{N}(|\psi|^2) \equiv \alpha|\psi|^2 + (1-\alpha\int R(t-t')|\psi(t')|^2dt'). \tag{5.2}$$

D is the nonlinear operator as we mentioned in Section II, i.e. $D = i\sum_{m=3}^{\infty}\frac{\beta_m}{m!}(i\frac{\partial}{\partial t})^m$. Considering the higher order dispersion as the pertubation, the solution could be written as $\psi(z) = \psi(z,\omega_0) + \psi_{blue}(z,\omega_2) + \psi_{red}(z,\omega_2)$.

The fiber which we are studying is a Kagome-lattice HC-PCF with a pitch of 12.5 μm (Fig. 5.7) and a strut-thickness of 550 nm [58]. Fig. 5.7 is the dispersion of this Kagome-lattice fiber. We could see that the dispersion is anomalous at around 800 nm for the light whose polarization is along the Axis 1. The optical soliton would be formed when a pulse centered around 800 nm propagating in the fiber.

We use theoretical simulation to solve the NSE with different inputting pulses. Fig. 5.8 is an example of how our simulation works. The input pulse is 50 fs centered at 800 nm, linearly polarized with nJ energy. The left of Fig. 5.8 shows the changing

of the spectrum during the propagation (y-axis). The right of Fig. 5.8 is how the pulse changes in time domain during the propagation. The propagation distance is 6 mm in our calculation. From the spectrum, we could see the generations of new waves (RDW) at UV and near IR region as the light propagates in the fiber.

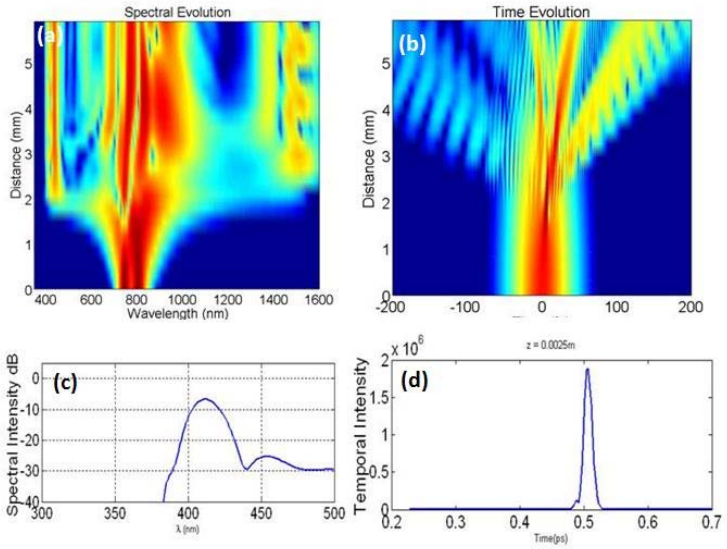

Figure 5.9: Theoretical simulation of propagation of two FTL pulses with different center wavelengths. (a) is how the spectrum evolves as the pulse propagates inside the fiber. (b) is how the pulse evolves in time during the propagation. (c) is the spectrum at 6 mm propagating distance at around 400 nm and (d) is the corresponding pulse in time domain. We theoretically filter out the beam below 500 nm.

We consider the situation of inputting of two fs pulses, which have similar energy, pulse width. The spectra of the two pulse are different by at least 70 nm, which means that they are still overlapped with each other. The simulation results are shown in Fig. 5.9. Fig. 5.9 (a) is how the spectrum evolves during the propagation (y-axis). Fig. 5.9 (b) is how the pulse evolves in time domain during the propagation. (c) is the spectrum when the pulse propagates 6 mm in the fiber and (d) is the corresponding

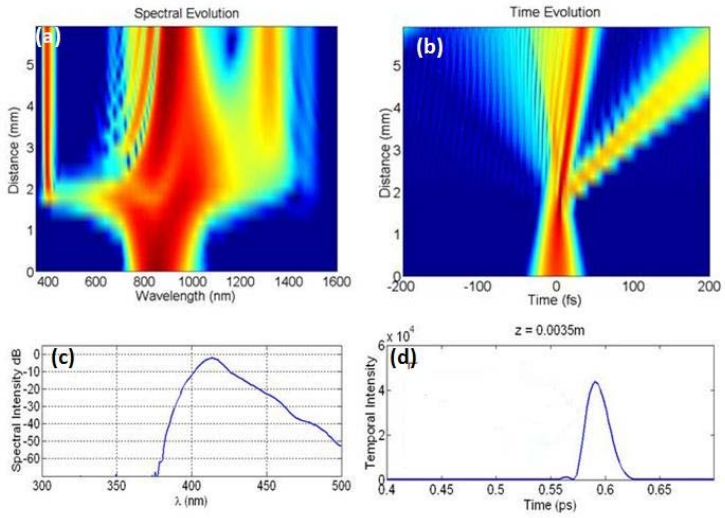

Figure 5.10: Theoretical simulation of the propagation of a chirped near-IR pulse. (a) is how the spectrum evolves as the pulse propagates inside the fiber. (b) is how the pulse evolves in time during the propagation. (c) is the spectrum at 6 mm propagating distance at around 400 nm and (d) is the corresponding pulse in time domain. We theoretically filter out the spectrum below 500nm.

pulse in time domain. We theoretically use a filter to filter the spectrum below 500 nm. It shows that the pulse as short as 30 fs is obtained in the blue/UV spectral region due to the mechanism of RDW generation. This implies that inputting two pulses, the ultrashort pulse at the short wavelength (400 nm) with a time duration under 30 fs is able to be generated in the Kagome photonic crystal fiber. Next we also consider the situation that the incident pulse is chirped with a broadband width centered at 800 nm. The result is shown in Fig. 5.10. The scheme of figure is the same as that of Fig. 5.9. It shows that with a broadband chirped pulse, it is possible to generate the ultrashort pulse around 50 fs at the short wavelength.

In conclusion, our theoretical result demonstrates a new approach to generate ultrashort pulse at Uv range. When RDW at UV is generated with inputting a near-IR pulse into the PCF, its time duration is usually around 100 fs. In order

to generate a UV pulse with shorter time duration, we could input two pulse with similar energy, bandwidth but a little different central wavelengths or a broadband chirped pulse to yield a sufficient short optical pulse in short wavelength. Moreover, in experiment, we need to use a short pass filter to separate this pulse from the fundamental pulse and the other RDW in near infrared.

6. CONCLUSIONS

We generate the broadband coherent Raman sidebands in Raman active crystal (diamond and $PbWO_4$) using femtosecond laser pulses. The spectrum of the Raman sidebands could be more than one octave, which provides the bandwidth potentially for a sub-cycle optical pulse. With the assistance of pulse shapers based on AOPDF or DM, we demonstrate that our setup is capable of characterizing and synthesizing the ultrafast waveform using the coherent Raman sidebands.

With the assistance of pulse shaper Dazzler, we demonstrate the mutual coherence of the spectral sidebands generated through molecular modulation in diamond, and show our capability to control spectral phases in a precise and stable manner, in a setup which combines manual, course adjustment of individual sideband phases with programmable pulse shaping and fine phase (and amplitude) tuning across the full spectrum. The good agreement between theory and experiment allows us to synthesize well-controlled and predictable temporal waveforms. Although in this experiment, we focus on 5 sidebands only, this method in principle can be extended to many more spectral lines. Moreover, it can also be applied to other frequency combs such as harmonics that are generated from OPAs [118]. In principle, with a broadband spectrum which is more than one-octave, we are able to synthesize the sub-cycle optical pulse with non-sinusoidal field. The non-traditional fields will find application in many areas of ultrafast science, such as coherent control [120].

The crystal inside the pulse shaper has a relative low damage threshold. It limits the pulse energy produced through this setup. Moreover, due to the bandwidth of commercial Dazzler, it only allows for the synthesis of an optical pulse whose duration is a few fetmoseconds. In order to synthesize the sub-femtosecond ultrafast wave-

form, different Dazzlers need to be combined to cover the required spectral range, which will be a complicated experimental setup. Therefore, in order to use more energy of the sidebands and simplify the system, we propose another scheme using spherical mirrors to assist ultrafast waveform synthesis. In this reflection scheme, the Raman sidebands are reflected back to the Raman crystal and we characterize the relative spectral phases of sidebands from an interferogram based on the nonlinear Raman interaction. Furthermore, in order to synthesize the ultrafast waveform, we insert a MEMS DM in the beam path to modify spectral phases. Using Raman sidebands generated from $PbWO_4$, we demonstrate that it is capable of synthesizing the ultrafast waveform using the coherent Raman sidebands with the assistance of DM. In this scheme, the ultrafast waveform is only yielded near the focal point of the spherical mirror. Even though the ultrafast waveform only maintains in a short distance, it is already sufficient for the studies of ultrafast nonlinear phenomena and high-field physics.

We explore the method of generating ultrafast pulses in PCF using theoretical simulation. In theory and experiment, people have demonstrated the RDW in photonic crystal fiber [59]. By inputting two near IR pulses or a broadband chirped pulse, our simulations show that a ultrashort UV pulse with sufficient short time duration could be obtained from RDW.

Besides the generation of ultrafast waveform, we also study the application of ultrafast laser pulses. The applications of femtosecond laser are versatile and highly cross-disciplinary. I present two experiments which demonstrate the application potential of femtosecond laser pulse. Using femtosecond laser filament, we demonstrate a remote-imaging method which retrieves images having resolution at least an order of magnitude greater than the diffraction limit. Femtosecond laser filament illuminates a remote target, and the backscattered light is collected to construct an image.

In particular, our demonstration experiment is directly applicable to high altitude airborne imaging of small objects beneath the ocean surface. Such remote imaging schemes are relevant to applications in which high-resolution must be obtained at a great distance and may find use both underwater and in the atmosphere. In the second experiment, we demonstrate an all optical controlling of a home-made TEA nitrogen laser triggered by a femtosecond laser pulse. The microsecond time jitter between the trigger and the lasing limits its application prospect. With two TEA lasers as a model, we also demonstrate the swept gain scheme for remote sensing. If we want to utilize this model in more practical application, we may be able to suppress the time jitter by replacing the electrodes with hydrogen thyratron to switch the air discharge inside the pencil-like gap.

REFERENCES

[1] A. Weiner, *Ultrafast Optics* (John Wiley & Sons Ltd., New York, 2009), 1st ed.

[2] F. Krausz, G. Korn, P. Corkum, and I. A. Walmsley, *Ultrafast Optics IV: Selected Contributions to the 4th International Conference on Ultrafast Optics, Vienna, Austria (Springer Series in Optical Sciences)* (Springer, New York, 2004).

[3] Z. Chang, *Fundamentals of Attosecond Optics* (CRC Press/Taylor Francis, Boca Raton, FL, 2011).

[4] X. Wen, *Ultrafast Spectroscopy: Principle and Applications in Semiconductor Nanostructures* (VDM Verlag, Saarbrcken, Germany, 2008).

[5] P. Hannaford, *Femtosecond Laser Spectroscopy* (Springer-Verlag, New York, 2005).

[6] M. Chergui, *Femtochemistry* (Springer-Verlag, New York, 1996).

[7] J. Ye and S. Cundiff, *Femtosecond Optical Frequency Comb: Principle, Operation, and Applications* (Springer-Verlag, New York, 2008).

[8] A. C. Eckbreth, *Laser Diagnostics for Combustion Temperature and Species (Combustion Science and Technology)* (Gordon and Breach, New York, 1996).

[9] S. Chin, *Femtosecond Laser Filamentation* (Springer, New York, 2010).

[10] F. Dausinger, F. Lichtner, and H. Lubatschowski, *Femtosecond Technology for Technical and Medical Applications* (Springer,Berlin, Germany, 2004).

[11] M. M. Martin and J. T. Hynes, *Femtochemistry and Femtobiology* (Elsevier, Amsterdam, N.L., 2004).

[12] F. P. Shafer, *Dye Lasers* (Springer-Verlag, Berlin, 1990).

[13] U. Keller, *Landolt-Bornstein, Laser Physics and Applications. Subvolume B: Laser Systems* (Springer-Verlag, Berlin, 2007).

[14] S. Popov, *Tunable Laser Applications* (John Wiley & Sons Ltd., New York, 2003), 2nd ed.

[15] I. Sansone, L. Poletto, and M. Nisoli, Nature Photonics **5**(656) (2011).

[16] S. Baker, I. Walmsley, and J. Marangos, Nature Photonics **5**(101038) (2011).

[17] L. I. R. and H. Edwards, eds., *Handbook of Raman Spectroscopy* (CRC Press, New York, 2001).

[18] F. Garmire, E.and Pandarese and C. H. Townes, Phys. Rev. Lett. **11**, 160 (1963).

[19] S. E. Harris and A. Sokolov, Phys. Rev. Lett. **55**, R4019 (1997).

[20] M. Belsley, D. T. Smithey, K. Wedding, and M. G. Raymer, Phys. Rev. A **48**, 1514 (1993).

[21] S. E. Harris and A. V. Sokolov, Phys. Rev. Lett. **81**, 2894 (1998).

[22] A. V. Sokolov, D. R. Walker, D. D. Yavuz, G. Y. Yin, and S. E. Harris, Phys. Rev. Lett. **85**, 562 (2000).

[23] D. D. Yavuz, D. R. Walker, G. Y. Yin, and S. E. Harris, Opt. Lett. **27**(9), 769 (2002).

[24] M. Shverdin, D. Walker, D. Yavuz, G. Yin, and S. Harris, Phys. Rev. Lett **94**, 033904 (2005).

[25] N. Zhavoronkov and G. Korn, Phys. Rev. Lett. **88**, 203901 (2002).

[26] D. Yavuz and J. Weber, Opt. Lett. **37**(20), 4191 (2012).

[27] J. Q. Liang, M. Katsuragawa, F. L. Kien, and K. Hakuta, Phys. Rev. Lett. **85**, 2474 (2006).

[28] M. Katsuragawa, J. Q. Liang, F. L. Kien, and K. Hakuta, Phys. Rev. A **65**, 025801 (2002).

[29] D. Yavuz, Phys. Rev. A **76**, 011805(R) (2007).

[30] K. Inoue, J. Kato, E. Hanamura, H. Matsuki, and E. Matsubara, Phys. Rev. B **76**, 041101 (2007).

[31] M. Zhi and A. Sokolov, Opt. Lett. **32**(10), 2251 (2007).

[32] A. S. Grabtchikov, R. V. Chulkov, V. A. Orlovich, M. Schmitt, R. Maksimenko, and W. Kiefer, Opt. Lett. **28**(11), 926 (2003).

[33] M. Zhi and A. Sokolov, New J. Phys. **10**, 025032 (2008).

[34] J. Strohaber, M. Zhi, A. Sokolov, A. Kolomenskii, G. Paulus, and H. Schuessler, Opt. Lett. **37**(16), 3411 (2012).

[35] M. Zhi, K. Wang, H. Hua, X.and Schuessler, J. Strohaber, and A. Sokolov, Opt. Express **21**(23), 27750 (2013).

[36] T. Kobayashi, J. Liu, and Y. Kida, IEEE J. of Selected Topics in Qunatum Electronics **18**, 1077 (2012).

[37] R. Weigand, J. Mendonca, and H. Crespo, Phys. Rev. A **79**, 063838 (2009).

[38] J. Kida, Y.and Liu and T. Kobayashi, Appl. Opt. **51**, 6403 (2012).

[39] A. Sokolov, D. Yavuz, D. Walker, G. Yin, and S. Harris, Phys. Rev. A **63**, 051801 (2001).

[40] K. R. Pandiri, T. Suzuki, S. A., K. Midorikawa, and M. Katsuragawa, Opt. Express **18**(2), 3110 (2012).

[41] H. Chan, Z. Hsieh, W. Liang, A. H. Kung, C. Lee, C. Lai, R. Pan, and L. Peng, Science **331**, 1165 (2011).

[42] D. Yavuz, Science **331**(6021), 1142 (2011).

[43] S. Cundiff and A. Weiner, Nature Photonics **4**(11), 760 (2010).

[44] A. Sokolov, M. Shverdin, D. Walker, D. Yavuz, A. Burzo, G. Yin, and S. Harris, Journal of Modern Optics **52**, 285 (2005).

[45] E. Matsubara, T. Sekikawa, and M. Yamashita, Appl. Phys. Lett. **92**, 071104

(2008).

[46] E. Matsubara, Y. Kawamoto, T. Sekikawa, and M. Yamashita, Opt. Lett. **34**(12), 1837 (2009).

[47] R. Trebino, *Frequency-Resolved Optical Gating: The Measurement of Ultrashort Laser Pulses* (Kluwer Academic Publisher, Norwell, MA, 2002), 1st ed.

[48] T. Hansch, Opt. Commun. **80**, 71 (1990).

[49] Z. M. Hsieh, C. J. Lai, H. S. Chan, S. Wu, C. Lee, W. Chen, C. Pan, F. Yee, and A. Kung, Phys. Rev. Lett. **102**(21), 213092 (2009).

[50] A. Couairon and A. Mysyrowicz, Phys. Rep. **441**, 47 (2007).

[51] L. Wooste and et al, Laser Optoelektron. **29**, 51 (1997).

[52] B. P. Sprangle, J. R. Penano, and B. Hafizi, Phys. Rev. E **66**, 046418 (2002).

[53] C. D'Amico, Y. Andre, S. Tzortzakis, M. Franco, B. Prade, A. Mysyrowicz, A. Couairon, E. Salmon, and R. Sauerbrey, Opt. Commun. **247**, 171 (2005).

[54] W. K., S. B. D., D. V. Voronine, M. O. Jha, P. K. Scully, R. E. Meyers, P. Hemmer, and A. V. Sokolov, Opt. Lett. **37**(8), 051801 (2012).

[55] G. Heck, J. Sloss, and R. J. Levis, Opt. Commun. **259**, 216 (2006).

[56] C. Willett, *Introduction to Gas Lasers: Population Inversion Mechanisms* (Pergamon, New York, 1974).

[57] P. R. Hemmer, R. Miles, P. Polynkin, T. Siebert, A. Sokolov, P. Sprangle, and M. Scully, Proc. Natl. Acad. Sci. **108**, 8 (2011).

[58] F. Benabid, f. Biancalana, and et al, Opt. Lett. **33**(22), 2680 (2008).

[59] J. Peng, F. Zhu, and A. Sokolov, Opt. Lett. **33**(14), 1620 (2008).

[60] R. Boyd, *Nonlinear Optics* (Academic Press, Burlington, MA, 2008), 3rd ed.

[61] P. Gibbon, *Short Pulse Laser Interactions with Matters: An Introduction* (Imperial College Press, London, U.K., 2005).

[62] M. Hercher, J. Opt. Soc. Am. **54**, 563 (1964).

[63] A. Braun, G. Korn, X. Liu, D. Du, J. Squier, and G. Mourou, Opt. Lett. **20**(1), 73 (1995).

[64] Q. Feng, J. V. Moloney, A. C. Newell, and E. M. Wright, Opt. Lett. **20**(19), 1958 (1995).

[65] A. Chiron, B. Lamouroux, R. Lange, J. F. Ripoche, M. Franco, B. Prade, G. Bonnaud, G. Riazuelo, and A. Mysyrowicz, Eur. Phys. J. D **6**, 383 (1999).

[66] B. La Fontaine, D. Comtois, C. Chien, A. Desparois, F. Gnin, G. Jarry, T. Johnston, J.-C. Kieffer, F. Martin, R. Mawassi, H. Ppin, F. Risk, F. Vidal, C. Potvin, P. Couture, and H. Mercure, J. Appl. Phys. **88**(2), 610 (2000).

[67] A. Hasegawa and M. Matsumoto, *Optical Solitons in Fibers* (Springer, New York, 2002), 3rd ed.

[68] A. N. and K. M., Phys. Rev. A **51**(3), 2602 (1995).

[69] C. Raman, Indian J. Phys. **2**, 387 (1928).

[70] G. Landsberg and L. Mandelstam, Naturwissenschaften **16**(28), 557 (1928).

[71] A. Smekal, Naturwissenschaften **11**(43), 873 (1932).

[72] R. Singh, Physics in Perspective **4**(4), 399 (2002).

[73] J. Cheng and S. Xie, *Coherent Raman Scattering Microscopy* (CRC Press/Taylor Francis Group, Boca Raton, FL, 2013).

[74] K. Hill, B. Kawasaki, and D. Johnson, Appl. Phys. Lett. **29**(3), 181 (1976).

[75] O. Boyraz and B. Jalali, Opt. Express **12**(21), 5269 (2004).

[76] N. W.K. and W. E.J., Appl. Phys. Lett. **18**(12), 550 (1971).

[77] G. Eckhardt, R. W. Hellwarth, F. McClung, S. E. Schwarz, D. Weiner, and W. E.J., Phys. Rev. Lett. **9**(11), 455 (1962).

[78] W. Demtröder, *Laser Spectroscopy: Basic Concepts and Instrumentation* (Springer Verlag, Berlin, Germany, 2003).

[79] A. A. Kaminskii, C. L. McCray, H. R. Lee, S. W. Lee, D. A. Temple, T. H.

Chyba, W. D. Marsh, J. C. Barnes, A. N. Annanenkov, V. D. Legun, H. J. Eichler, G. M. A. Gad, and K. Ueda, Opt. Commun. **183**, 277 (2000).

[80] R. P. Mildren and A. Sabella, Opt. Lett. **34**(18), 2811 (2009).

[81] H. Kawano, Y. Hirakawa, and T. Imasaka, IEEE Journal of Quantum Electronics **34**(2), 260 (1998).

[82] A. A. Kaminskii, H. J. Eichler, K. Ueda, N. V. Klassen, B. S. Redkin, L. E. Li, J. Findeisen, D. Jaque, J. Garcia-Sole, J. Fernandez, and R. Balda, Appl. Opt. **38**, 4533 (1999).

[83] F. Kien, J. Liang, M. Katsuragawa, K. Ohtsuki, K. Hakuta, and A. Sokolov, Phys. Rev. A **60**, 1562 (1999).

[84] S. E. Harris, Opt. Lett. **19**(23), 2018 (1994).

[85] F. Kien and K. Shon, N.H. Hakuta, Phys. Rev. A **64**, 051803 (2001).

[86] A. Sokolov and S. Harris, J. Optics B **5**, R1 (2003).

[87] M. Zhi and A. Sokolov, IEEE J. Sel. Top. Quantum Electron **18**, 460 (2012).

[88] T. T. Basiev and R. C. Powell, Optical Materials **11**(4), 301 (1999).

[89] P. Lecoq, I. Dafinei, E. Auffray, M. Schneegans, M. V. Korzhik, O. V. Missevitch, V. B. Pavlenko, A. A. Fedorov, A. N. Annenkov, V. L. Kostylev, and V. D. Ligun, Nuclear Instruments and Methods in Physics Research Section A: Accelerators, Spectrometers, Detectors and Associated Equipment **365**, 291 (1995).

[90] F. Manjon, D. Errandonea, N. G. Munoz, J. Pellicer-Porres, J. Lopez-Solano, P. Rodriguez-Hernandez, S. Radescu, and A. Mujica, Phys. Rev. B. **74**(14), 144112 (2006).

[91] J. Takahashi, Y. Kawabe, and E. Hanamura, Opt. Express **12**(7), 1185 (2004).

[92] A. Wirth, M. Hassan, I. Grguras, J. Gagnon, A. Moulet, T. Luu, S. Pabst, R. Santra, Z. Alahmed, A. Azzeer, V. Yakovlev, V. Pervak, F. Krausz, and

E. Goulielmakis, Science **334**(6053), 195 (2011).

[93] I. Hartl, X. Li, C. Chudoba, C. Ghanta, T. Ko, J. Fujimoto, J. Ranka, and R. Windeler, Opt. Lett. **26**(9), 608 (2001).

[94] J. Ranka, R. Windeler, and A. Stentz, Opt. Lett. **25**(1), 25 (2000).

[95] D. J. Jones and et al, Science **288**, 635 (2000).

[96] C. Dunsby and et al, J. Phys. D: Applied Physics **37**, 3296 (2004).

[97] H. Delbarre and M. Tassou, Conference on Lasers and Electro-Optics Europe p. CWF104 (2000).

[98] H. Takara, T. Ohara, T. Yamamoto, H. Masuda, M. Abe, H. Takahashi, and T. Morioka, Elect. Lett. **41**, 270 (2005).

[99] S. Sanders, Appl. Phys. B: Lasers and Optics **75**, 799 (2002).

[100] J. Dudley, G. Genty, and S. Coen, Rev. Mod. Phys. **78**, 1135 (2006).

[101] T. Kippenberg, R. Holzwarth, and S. Diddams, Science **324**(6029), 555 (2011).

[102] J. Green, T. Sikes, and D. Yavuz, Opt. Lett. **34**(17), 2563 (2009).

[103] S. Oemrawsingh, J. van Houwelingen, E. Eliel, J. Woerdman, E. Verstegen, J. Kloosterboer, and G. 't Hooft, Appl. Opt. **43**, 688 (2004).

[104] A. Gorbach, D. Skryabin, and C. Harvey, Phys. Rev. A **77**, 063810 (2008).

[105] A. Weiner, Rev. Sci. Instr **71**, 1929 (2000).

[106] A. M. Weiner, D. E. Leaird, G. P. Wiederrecht, and K. A. Nelson, Science **2471**, 1317 (1990).

[107] N. Dudovich, D. Oron, and Y. Silberberg, Nature **418**, 512 (2002).

[108] T. Brixner, N. H. Damrauer, P. Niklaus, and G. Gerber, Nature **414**, 57 (2001).

[109] R. J. Levis, G. M. Menkir, and H. Rabitz, Science **292**, 709 (2001).

[110] R. Bartels, S. Backus, E. Zeek, L. Misoguti, G. Vdovin, I. Christov, M. Murnane, and H. Kapteyn, Nature **406**, 164 (2000).

[111] C. Joe-Wong, T. Ho, R. Long, H. Rabitz, and R. Wu, J. Chem. Phys. **138**,

124114 (2013).

[112] D. Pestov and et al, Science **316**(5822), 265 (2007).

[113] X. Wang, K. Wang, G. Welch, and A. Sokolov, Phys. Rev. A **84**, 021801 (2011).

[114] Z. Jiang, C. Huang, D. Leaird, and A. Weiner, Nature Photonics **1**, 463 (2007).

[115] K. Yoshii, J. Anthony, and M. Katsuragawa, XVIIITH INTERNATIONAL CONFERENCE ON ULTRAFAST PHENOMENA Book Series: EPJ Web of Conferences **41**(01010) (2013).

[116] N. Forget, V. Crozatier, and T. Oksenhendler, J. Opt. Soc. Am. **27**, 742 (2010).

[117] B. Xu, J. Gunn, D. C. J.M., L. V. V., , and M. Dantus, J. Opt. Soc. Am. B **23**, 750 (2006).

[118] W. Chen, Z. Hsieh, S. Huang, H. Su, C. Lai, T. Tang, C. Lin, R. Pan, C. Pan, and A. H. Kung, Phys. Rev. Lett. **100**, 163906 (2008).

[119] J. Sun, B. Gale, and D. Reid, Opt. Lett. **32**(11), 1414 (2007).

[120] E. Goulielmakis, V. Yakovlev, A. Cavalieri, M. Uiberacker, V. Pervak, A. Apolonski, R. Kienberger, U. Kleineberg, and F. Krausz, Science **317**, 769 (2007).

[121] M. Zhi, X. Wang, and A. Sokolov, Opt. Express **16**(16), 12139 (2008).

[122] N. Dudovich, D. Oron, and Y. Silberberg, J. Chem. Phys. **118**, 9208 (2003).

[123] J. Kasparian, L. Woste, and J. Wolf, Optics and Photonics News Optics and Photonics News **21**(7), 22 (2010).

[124] A. Dogariu, J. B. Michael, M. O. Scully, and R. B. Miles, Science **331**, 442 (2011).

[125] M. Born and E. Wolf, *Principles of Optics* (CUP Archive, Cambridge, U.K., 1999), 7th ed.

[126] S. Mouradian, F. N. C. Wong, and J. H. Shapiro, Opt. Express **19**(6), 5480 (2011).

[127] J. Eckbreth, *Remote Sensing Of The Environment: An Earth Resource Perspective* (Prentice Hall, New York, 2007), 2nd ed.

[128] E. Betzig and et al., Science **313**, 1642 (2006).

[129] M. Rust, M. Bates, and X. Zhuang, Nature Methods **3**(10), 793 (2006).

[130] S. T. Hess, T. P. K. Girirajan, and M. D. Mason, Biophys. J. **91**(11), 4258 (2006).

[131] S. W. Hell, Nature Biotechnol. **21**, 1347 (2003).

[132] A. N. Boto and et al., Phys. Rev. Lett. **85**, 2733 (2000).

[133] G. S. Agarwal, R. Boyd, E. M. Nagasako, and S. J. Bentley, Phys. Rev. Lett. **86**, 1389 (2001).

[134] S. J. Bentley and R. Boyd, Opt. Express **12**(23), 5735 (2004).

[135] M. P. Stocker, L. Li, R. R. Gattass, and J. T. Fourkas, Nature Chemistry **3**, 223 (2011).

[136] Z. Liao, M. Al-Amri, and M. S. Zubairy, Phys. Rev. Lett. **105**, 183601 (2010).

[137] P. R. Hemmer, A. Muthukrishnan, M. O. Scully, and M. S. Zubairy, Phys. Rev. Lett. **96**, 163603 (2006).

[138] P. R. Hemmer, Proc. SPIE **8163**, 24 (2011).

[139] R. E. Meyers, K. S. Deacon, and Y. Shih, Phys. Rev. A. **77**, 041801(R) (2008).

[140] R. E. Meyers, K. S. Deacon, and Y. Shih, J. Mod. Opt. **54**, 2381 (2007).

[141] R. E. Meyers, K. S. Deacon, and Y. Shih, Appl. Phys. Lett **98**, 111115 (2011).

[142] M. Rodriguez and et al., Phys. Rev. E **69**, 036607 (2004).

[143] G. Fibich and et al., Opt. Express **14**(12), 4946 (2006).

[144] W. Liu and et al., Appl. Phys. B **85**, 55 (2006).

[145] J. F. Daigle and et al., Appl. Phys. B **97**, 701 (2009).

[146] A. Zemlyanov and Y. Geints, Opt. Commun. **259**, 799 (2006).

[147] P. Polynkin, M. Kolesik, A. Roberts, D. Faccio, P. Di Trapani, and J. Moloney,

Opt. Express **16**(20), 15733 (2008).

[148] R. E. Meyers and K. S. Deacon, Proc. SPIE **7815**, 78150I (2010).

[149] R. E. Meyers, K. S. Deacon, and A. Tunick, Physics of Quantum Electronics,Snowbird, UT p. 2 (2011).

[150] R. E. Meyers and K. S. Deacon, Physics of Quantum Electronics,Snowbird, UT p. 2 (2011).

[151] O. Katz, Y. Bromberg, and Y. Silberberg, Appl. Phys. Lett. **95**, 131110 (2009).

[152] M. A. T. Figueiredo, R. D. Nowak, and S. J. Wright, IEEE J. Sel. Top. Signa. **1**, 586 (2007).

[153] E. J. Cande's, J. K. Romberg, and T. T., Commun. Pur. Appl. Math. **59**(8), 1207 (2005).

[154] P. Polynkin, M. Kolesik, J. V. Moloney, G. A. Siviloglou, and D. N. Christodoulides, Science **324**, 229 (2009).

[155] J. Bernhardt, W. Liu, S. L. Chin, and S. R., Appl. Phys. B **91**(1), 45 (2008).

[156] J. Liu, A. J. Jakas, A. Al-Obaidi, and Y. Liu, ETFA, 2010 IEEE Conference on p. 1 (2010).

[157] J. S. Jaffe, Opt. Express **18**(12), 12328 (2010).

[158] T. G. Jones, A. Ting, J. Penano, P. Sprangle, and G. DiComo, CLEO/QELS 2006 Conference on p. 1 (2006).

[159] W. Chen, K. Beck, R. Bucker, M. Gullans, M. Lukin, H. Tanji-Suzuki, and V. Vuletic, Science **341**, 768 (2013).

[160] V. Almeida, C. Barrios, R. Panepucci, and M. Lipson, Nature **431**, 1081 (2004).

[161] K. Tamura and et al, Opt. Lett. **18**(13), 1080 (1993).

[162] K. Tamura and M. Nakazawa, Appl. Phys. Lett. **67**, 3691 (1995).

[163] J. Liu, K. Okamura, Y. Kida, T. Teramoto, and T. Kobayashi, Opt. Express **18**(20), 20645 (2010).

[164] A. Husakou and J. Herrmann, Phys. Rev. Lett. **87**, 203901 (2001).

[165] P. Wai, C. Menyuk, Y. Lee, and H. Chen, Opt. Lett. **11**(7), 464 (1986).